Department of Physics and Astronomy

University College London

Computational study of defects and heat transfer in gold nanostructures

Thesis submitted for the degree of Doctor of Philosophy

by

Ana Sofia Araújo Vila Verde

2012

I, Ana Sofia Araújo Vila Verde, confirm that the work presented in this thesis is my own. Where information has been derived from other sources, I confirm that this has been indicated in the thesis.

Abstract

Gold nanoparticles are promising tools for cancer therapy and cell imaging due to their non-toxicity, high heat conduction and tunable optical properties for the infrared-visible region. Nanoparticles production often involves thermal annealing, a process that changes the structure of the nanoparticle by mechanisms that are not yet well understood. For any of the biomedical applications, the nanoparticles are organically-coated to allow targeting and efficient uptake by cancer cells. Once the nanoparticles are inside the cell, their optical tunability allows the use of specific wavelengths strongly absorbed or scattered by the particles but poorly interacting with the medium to induce hyperthermia or obtain an image of the cell. In any case, the nanoparticle is expected to heat up. Although the propagation of heat is well understood at the macroscale, the details of the heat transfer at the nanoscale are still poorly understood. In this work, we use classical, equilibrium molecular dynamics simulations to create nanoparticles and investigate how their crystalline structure and the number and type of defects evolves as a function of annealing conditions. We use both analytical methods and classical non-equilibrium molecular dynamics simulations to investigate the effects of the particle size and the type of interface on the heat transfer properties of bare and organic-coated gold nanoparticles embedded in water. Water was chosen to mimic the cellular medium because it is the most abundant cellular component. Our simulations with a slab system of water and gold suggest that the material present at the interface between the gold and the water affects the heat transfer in the system. Moreover, our analytical calculations and computational results indicate that the heat transfer is dominated by the heat conduction in the medium for large nanoparticles, while for smaller nanoparticles the interface controls the overall heat propagation.

Acknowledgements

I am deeply thankful to my advisors Dorothy, Marshall and Tony for the many discussions held over the duration of this project and for keeping me from getting carried away and from spreading my work in too many directions. I would also like to express my gratitude to Kai Nordlund and his group, from the Department of Physics, Univerisity of Helsinki, for receiving me twice as a visitor. The three months spent in his group were definitely among the best I had during my PhD.

I would like to acknowledge the "Fundação para a Ciência e a Tecnologia" (the Portuguese National Science Foundation) and the European Social Fund for grant SFRH/BD/38150/2007, the HPC-Europa2 Transnational Access Programme for supporting my two visits to Kai Nordlund's group, University of Helsinki, and access to the clusters in CSC, and the UCL Graduate School, the Department of Physics and Astronomy and the Institute of Physics for their grants that allowed me to attend international conferences.

Finally, I know it was not easy to put up with a bad-mood-Ana and work-only-Ana sometimes... For this reason, I would like to express a sincere "muito obrigada" to my family and friends for all the support and patience during this entire PhD-saga, with a special emphasis to my sister Célia.

Contents

1 Introduction and motivation **16**

2 Background **18**
2.1 Heat transfer 18
2.1.1 Modes of heat transfer 18
2.1.2 Heat conduction 20

3 Overview of the production, preparation and use of gold nanostructures for biomedical applications **22**
3.1 Production of gold nanoparticles 22
3.2 Preparation of gold nanoparticles functionalised with proteins 24
3.3 Gold nanoparticles for diagnosis and therapy 26
3.3.1 Studies on cell uptake and cytotoxicity 28
3.3.2 Studies on living body circulation and clearance 30
3.3.3 Other aspects relevant for the use of nanoparticles on bioapplications 31
3.4 Heat transfer studies 32

4 Methodology **39**
4.1 Molecular dynamics 39
4.1.1 Force fields 40
4.1.2 Initialisation 48
4.1.3 Force calculation and integration algorithms 49
4.1.4 Ensembles 50
4.2 Non-equilibrium molecular dynamics 51
4.2.1 Two thermostats method 52
4.2.2 Heat source and sink method 54

4.2.3 Comparison between the two methods . . . 57
4.3 Determination of the steady state regime . . . 59
4.4 Determination of the heat transfer coefficient - planar system . . . 62
4.5 Determination of the heat transfer coefficient - spherical system . . . 64
4.6 Verification of nanoparticle melting . . . 67
4.7 Analysis of crystal lattice defects . . . 67
4.7.1 Order parameter performance . . . 70

5 Production of nanoparticles and analysis of defects 72
5.1 Annealing of nanoparticles . . . 73
5.1.1 Systems simulated and conditions used . . . 73
5.2 Computational results for the annealing process . . . 75
5.2.1 Verification of the melting of the particle core . . . 75
5.2.2 Estimate of the minimum cooling rate for crystallisation . . . 76
5.2.3 Effect of cooling rate on the crystal structure . . . 80
5.3 Analysis of nanoparticle structure . . . 84
5.4 Summary . . . 92

6 Analytical and computational studies of heat transfer for bare gold-water systems 93
6.1 Introduction and motivation . . . 93
6.2 Heat flow at extreme conditions, an analytical approach . . . 94
6.2.1 Heat flow dominated by the conduction in the medium . . . 94
6.2.2 Heat flow dominated by the gold-water interface . . . 95
6.2.3 Intermediate conclusion . . . 100
6.3 Bare gold-water heat transfer coefficient . . . 101
6.3.1 Systems and conditions simulated . . . 101
6.3.2 Results and discussion . . . 105
6.3.3 Summary . . . 108

7 Determination of heat transfer coefficient at the organic-coated gold-water interfaces 110
7.1 Systems and conditions simulated . . . 111
7.2 Results and discussion . . . 115
7.3 Summary . . . 118

8 Studies on heat release in a spherical geometry **119**
8.1 Dependence of heat flow with nanoparticle size 120
8.1.1 Systems and conditions simulated 120
8.1.2 Results and discussion 124
8.2 Dependence of heat flow with the temperature of the nanoparticle . . . 130
8.2.1 Results and discussion 132
8.3 Summary 134

9 Conclusions **137**
9.1 Future work 140

A Implementation of the NEMD methods in the MD code **153**
A.1 Implementation of the two thermostats method 154
A.2 Implementation of the heat source and sink method 154
A.3 Monitoring the evolution of the system 155
A.3.1 Division of system into slabs or coronae 155
A.3.2 Determination of the temperature per slab or corona 156

B Values for the material variables **157**

C Order parameter results for defects created in a perfect lattice **162**

D Results related to the annealing of the nanoparticles **164**

E Results related to the abnormality of thirteen atomic neighbours **186**

List of Tables

5.1 Conditions and results obtained from the annealing of nanoparticles with different number of atoms. 74

6.1 Heat flux at steady state, for the extreme case of heat propagation dominated by the heat conduction in the medium. 95
6.2 Analytical results for the extreme case of heat propagation dominated by the interface, from the point of view of the particle. 98
6.3 Initial heat flux, for the extreme case of heat propagation dominated by the interface, from the point of view of the medium. 100
6.4 Description and simulation conditions of the several gold-water-gold slab systems. 104
6.5 Results obtained from the linear regression on the simulation results for the gold-water-gold slab systems. 105
6.6 Analytical results for the extreme case of heat flow dominated by the interface, with the new value of H, from the point of view of the particle. 108

7.1 Description of the systems simulated and of the specific conditions used to determined the value of the heat transfer coefficient for the organic-coated gold-water interfaces. 114
7.2 Results obtained from the linear regression on the simulation results for systems of two organic-coated gold slabs separated by a water layer. . . 115

8.1 Description of the spherical systems simulated and of the specific conditions used to determined the transition of the dominant heat transfer mechanism with the nanoparticle size. 123
8.2 Temperature profile at the interface and in the non-thermostated water, and the ratio of these two quantities, for each of the nanoparticle sizes simulated. 124

8.3 Description of the non-equilibrium conditions applied to the spherical system of a gold nanoparticle of radius approximately 2 nm embedded in a water box. 131

List of Figures

3.1 Absorption spectrum of various living tissue components. 26

4.1 Water-gold interatomic potential plots. 42
4.2 Schematic view and initial temperature profile of the system once the two thermostats method is imposed. 53
4.3 Schematic view and temperature profile of the system at steady state. . 54
4.4 Schematic view and initial temperature profile of the system immediately after the source and sink method is imposed. 55
4.5 Configuration energy when different non-equilibrium methods are applied to a slab system. 58
4.6 Steady state average density and temperature distribution for a slab system under non-equilibrium conditions. 59
4.7 Example of the weighted mean temperatures, rolling averages and temperature differences used to determine when the steady state regime is reached. 61
4.8 Schematic view of the slab system gold-water-gold and its analogous electrical circuit. 62
4.9 Scheme of a perfectly spherical and of a realist hot nanoparticle embedded in water, at steady state, under the two thermostats method. . . . 65
4.10 Colour scheme attributed to the range of ψ values. 69
4.11 Order parameter colour scheme for a twin boundary and a stacking fault. 70

5.1 Results regarding the verification of the melting of the nanoparticle core before the start of the cooling process. 77
5.2 Atomic configurations and radial distribution functions of the particle of approximately 5.5 nm diameter (5324 atoms), obtained with different cooling rates. 78

5.3 Atomic configurations of the particle with approximately 4 nm diameter (2048 atoms) obtained with different cooling rates. 79
5.4 Configuration energies and radial distribution functions for the particle of approximately 4 nm diameter (2048 atoms) for the several cooling processes simulated. 81
5.5 Diffusion coefficients for the particle of approximately 4 nm diameter (2048 atoms) for the several annealing processes simulated. 82
5.6 Structure of the particle with diameter of approximately 2 nm (256 atoms), at 300 K, coloured according to the local order parameter values and number of neighbours. 84
5.7 Structure of the particle with diameter of approximately 2.5 nm (500 atoms), at 300 K, coloured according to the local order parameter values and number of neighbours. 85
5.8 Structure of the particle with diameter of approximately 3 nm (864 atoms), at 300 K, coloured according to the local order parameter values and number of neighbours. 86
5.9 Structure of the particle with diameter of approximately 3.5 nm (1372 atoms), at 300 K, coloured according to the local order parameter values and number of neighbours. 86
5.10 Structure of the particle with diameter of approximately 4 nm (2048 atoms), at 300 K, coloured according to the local order parameter values and number of neighbours. 87
5.11 Structure of the particle with diameter of approximately 7 nm (10976 atoms), at 300 K, coloured according to the local order parameter values and number of neighbours. 87
5.12 Structure of the particle with diameter of approximately 10 nm (32000 atoms), at 300 K, coloured according to the local order parameter values and number of neighbours. 88
5.13 Evidence of the regions with HCP and FCC structure in the particle with approximately 10 nm diameter. 88
5.14 Structure of the particle with diameter of approximately 14 nm (84985 atoms), at 300 K, coloured according to the local order parameter values and number of neighbours. 89
5.15 Images of gold nanoparticles, obtained experimentally and computationally, presenting five-fold symmetries. 90

5.16 Two views of the structure of the twelve neighbours surrounding an atom localised in the intersection of the five twin boundaries. 91

6.1 Scheme of the system of bare gold slabs separated by a water box. . . . 102
6.2 Volume, water density, weighted mean temperature and water slab thickness evolution over time, when the system of two gold slabs separated by a water layer is equilibrated. 103
6.3 Dependence of the thermal resistance on the water thickness, obtained with several gold-water-gold slab systems. 106

7.1 Scheme of the system of organic-coated gold slabs separated by a water box. 111
7.2 Volume, water density, weighted mean temperature and water slab thickness evolution over time, when the system of two organic-coated gold slabs separated by a water layer is equilibrated. 113
7.3 Dependence of the thermal resistance on the water thickness, obtained with several systems of two organic-coated gold slabs separated by a water slab. 116

8.1 Volume, water density and weighted mean temperature evolution over time, for a system of a gold nanoparticle embedded in a water box. . . 122
8.2 Temperature profile at the gold-water interface and through the non-thermostated water, for several hot nanoparticles embedded in cold water. 125
8.3 Heat transfer coefficient versus the radius of the gold nanoparticles and versus the inverse nanoparticle radius. 126
8.4 Averaged mass density profile, at steady state, for the non-thermostated water embedding the hot nanoparticles of different radii. 129
8.5 Temperature profile at the gold-water interface and through the non-thermostated water, for the nanoparticle (diameter $\approx$ 4 nm) set to different temperatures embedded in cold water. 132
8.6 Heat transfer coefficient for different temperatures of the gold nanoparticles of diameter $\approx$ 4 nm. 133
8.7 Averaged mass density profile, at steady state, for the non-thermostated water embedding the hot nanoparticle (diameter $\approx$ 4 nm) set to different temperatures. 135

C.1 Order parameter colour schemes on a perfect cubic system, where 5 vacancies were created. 162
C.2 Order parameter colour schemes on a perfect cubic system, where 10 vacancies were created. 163
C.3 Order parameter colour schemes on a perfect cubic system, where 100 vacancies were created. 163

D.1 Part 1/2 - Results for the heating process of the particle with approximately 2 nm diameter. 165
D.2 Part 2/2 - Results for the cooling process of the particle with approximately 2 nm diameter. 166
D.3 Part 1/2 - Results for the heating process of the particle with approximately 2.5 nm diameter. 167
D.4 Part 2/2 - Results for the cooling process of the particle with approximately 2.5 nm diameter. 168
D.5 Part 1/2 - Results for the heating process of the particle with approximately 3 nm diameter. 169
D.6 Part 2/2 - Results for the cooling process of the particle with approximately 3 nm diameter. 170
D.7 Part 1/2 - Results for the heating process of the particle with approximately 3.5 nm diameter. 171
D.8 Part 2/2 - Results for the cooling process of the particle with approximately 3.5 nm diameter. 172
D.9 Part 1/5 - Results for the heating processes of the particle with approximately 4 nm diameter. 173
D.10 Part 2/5 - Results for the faster cooling rates of the particle with approximately 4 nm diameter, when the cooling process started at 900 K. 174
D.11 Part 3/5 - Results for the slower cooling rates used for the particle with approximately 4 nm diameter, when the cooling process started at 900 K. 175
D.12 Part 4/5 - Results for the slowest cooling rate (when the cooling process started at 900 K) and for the fastest cooling rate (when the cooling process started at 800 K) for the particle with approximately 4 nm diameter. 176
D.13 Part 5/5 - Results for the slower cooling rates used for the particle with approximately 4 nm diameter, when the cooling process started at 800 K. 177

D.14 Part 1/2 - Results for the heating process of the particle with approximately 5.5 nm diameter. 178
D.15 Part 2/2 - Results for different cooling rates for the particle with approximately 5.5 nm diameter. 179
D.16 Part 1/2 - Results for the heating process of the particle with approximately 7 nm diameter. 180
D.17 Part 2/2 - Results for the cooling process of the particle with approximately 7 nm diameter. 181
D.18 Part 1/3 - Results for the heating process of the particle with approximately 10 nm diameter. 182
D.19 Part 2/3 - Results for the fastest cooling process of the particle with approximately 10 nm diameter. 183
D.20 Part 3/3 - Results for the slowest cooling process of the particle with approximately 10 nm diameter. 184
D.21 Results for the production of the particle with approximately 14 nm diameter 185

E.1 Examples of clusters with thirteen neighbours, present in the created nanoparticles. 187
E.2 Examples of clusters with thirteen neighbours, present in the particle with 7 nm in diameter. 187
E.3 Structure of the particle with diameter of approximately 2 nm (256 atoms), at 10 K, coloured according to the local order parameter values and number of neighbours. 188
E.4 Structure of the particle with diameter of approximately 2.5 nm (500 atoms), at 10 K, coloured according to the local order parameter values and number of neighbours. 188
E.5 Structure of the particle with diameter of approximately 3.5 nm (1372 atoms), at 10 K, coloured according to the local order parameter values and number of neighbours. 189
E.6 Structure of the particle with diameter of approximately 7 nm (10976 atoms), at 10 K, coloured according to the local order parameter values and number of neighbours. 189

E.7 Structure of the particle with diameter of approximately 10 nm (32000 atoms), at 10 K, coloured according to the local order parameter values and number of neighbours. 190
E.8 Structure of the particle with diameter of approximately 14 nm (84895 atoms), at 10 K, coloured according to the local order parameter values and number of neighbours. 190

Chapter 1

Introduction and motivation

Gold is a material well known for being nontoxic, unreactive with air, water and many reagents[1], while simultaneously being easily conjugated to antibodies or proteins using thiol bonds[2]. When gold is restrained to sizes of the order of nanometres, its optical[3] properties change as a function of the structure's size and shape. For instance, the size and shape of gold nanoparticles or gold coated nanoparticles can be tuned to make them strong absorbers and scatterers[4]. The ease of use of thiol chemistry with gold nanoparticles makes it possible to coat them with organic molecules and thus control their surface chemistry, e.g., to passivate them and to control their electrical charge (i.e., the assembly surface can be negatively, positively or neutrally charged).

These characteristics make gold and gold-coated nanoparticles (NP) promising materials for a number of applications: building blocks of nanostructured materials[5], solar cells[6], nanoelectronic digital circuits[5, 7], detection and copy of DNA, RNA and proteins[8], drug delivery[9], and imaging or killing of specific tissues in the body[2, 4, 10].

Among these applications, some require that an energy source be shone on the medium containing the gold nanoparticles. This may lead to a change in temperature of the particle, which can significantly influence its performance or its surrounding environment. In the case of therapeutic tissue killing, one of the main applications considered in this study, a typical energy source may be a laser, whose photon frequency can be chosen to optically stimulate the free electrons present in the gold. If the wavelength of the laser beam matches the collective plasmon frequency of the free electrons, a majority of the radiation that hits the nanoparticles is absorbed and not re-emitted or scattered[11]. Consequently, this absorption heats up the nanoparticles and their surrounding medium by several relaxation mechanisms. For imaging applications,

the properties of the source must be carefully chosen to minimise the light absorption by the gold nanoparticles and their environment, and maximise the scattering effect. However, wavelengths that meet these requirements may be strongly absorbed by other components of the surrounding medium, so one must considerer the composition of the surrounding medium, together with the size, shape, organic-coating and concentration of nanoparticles.

For these biomedical applications, it is also fundamental that the nanoparticles are taken up by particular tissues. High concentrations of particles in these tissues can be achieved by using thiol chemistry to coat the particles with specific organic molecules, which allow for specific cell targeting as well as an increased circulation time in the blood stream before being filtered by the liver, spleen or kidneys[12, 13].

The nanoparticles lose any absorbed energy by radiative and non-radiative processes, i.e., by radiation, conduction and convection. In a therapeutical context, it is desired that the surrounding medium of the gold nanoparticles heats up to a temperature that can induce cell death[14] by apoptosis ($42 - 43\,^{\circ}\mathrm{C}$) or necrosis ($\geq 44\,^{\circ}\mathrm{C}$) without requiring a vast amount of laser time and with minimum damage to the healthy system. Therefore, the goal is the optimisation of a fast release of heat from the nanoparticle to the surrounding medium. The imaging techniques, on the contrary, require the smallest temperature variation of the medium surrounding the nanoparticles while the laser is in use. In this case, the goal is to minimise the heat transfer from the nanoparticle to the surrounding medium. Optimisation of the heat transfer in each case requires the knowledge of the thermal properties of the nanoparticles, in some cases the coating, their surrounding medium and the interface between these two or more components.

This thesis focuses on the therapeutic and imaging applications of gold nanoparticles. The aim is to understand how nanoparticle size, shape and coating influence the heat propagation from the hot nanoparticle to the colder medium. In the following pages more detailed background on these topics is provided, as well as the methodology used. Following this, the work done so far will be reported.

Chapter 2

Background

2.1 Heat transfer

The majority of the work presented in this thesis aims to understand the heat propagation that occurs when hot gold nanoparticles are embedded in cold water. Before tackling such systems through computational methods, it is important to understand the impact of the heat transfer mechanisms involved through an analytical approach. Therefore, in the next few pages, a short discussion is provided on the heat transfer mechanisms and equations needed to perform such analytical study.

When there is a difference in temperature between two bodies in contact or within the same body, energy is transferred from the part at higher temperature to the part at lower temperature. This process is defined as *heat transfer*[15]. Mathematically, heat flow can be described by a vector pointing in the direction of a negative temperature gradient, i.e., from higher toward lower temperatures. Since a difference in temperatures can exist in a variety of conditions and systems, and may impact the system behaviour, the process of heat transfer is widely studied in almost every branch of engineering and science[15, 16].

2.1.1 Modes of heat transfer

Heat transfer through a body or through two or more bodies may occur by three basic and distinct mechanisms[15, 16]:

- **Conduction**: occurs when the heat is transferred through a body (solid, liquid

or gaseous) or across the interface between two bodies in contact by transfer of internal energy, due to a temperature difference. Changes in the internal energy happen mainly through molecular motion and, in some cases, also by the flow of free electrons and lattice vibrations. Therefore, both transfer of kinetic energy and flux of potential energy contribute to changes in internal energy.

- **Convection**: is associated with heat transfer that occurs via the movement of a fluid, i.e., by mass transfer. When the movement is due to a temperature difference that causes a difference in densities within a fluid acted on by gravity, then the heat transfer is called *free* or *natural convection*. If the movement of the fluid is artificially induced, then the heat transfer is termed *forced convection*. Also, for some authors[15], convection is the result of heat conduction in moving fluids.

- **Radiation**: is the heat transfer in the form of electromagnetic waves, as described by Maxwell's classic electromagnetism, or in the form of photons, according to Planck's theory.

In reality, the heat transfer in a system usually results from a combination of these three mechanisms, making the complete study of heat transfer a very difficult task. Fortunately, in many systems heat transfer is dominated by one of these mechanisms, and when this happens the behaviour of the real system can still be reproduced when the less important mechanisms are not considered. To identify which heat transfer mechanism contributes most to the heat transfer in any given system, each mechanism must first be studied individually. The mathematical equations that govern heat transfer for the three mechanisms mentioned above are distinct, since each mechanism has to take into account different variables/properties of the system.

The heat diffusion in systems of hot gold particles embedded in a cold medium is mainly due to the heat conduction in the metal, the heat transfer through the gold-water interface and, as a first approximation, the heat conduction through the water. In the metal, heat conduction is considered to be the only mechanism of heat transfer, since it has a considerably higher impact on the heat diffusion than the two other mechanisms[17]. As for the interface, the molecular process involved in the heat transfer is still not clear. Several times convection is associated to the energy transfer process at

the interface between a solid and a liquid[1] or can actually be due to conduction between the two media or materials[2]. Owing to this ambiguity and lack of concrete information, the "convection" term may be used further on in this thesis and related to the heat transfer through the interface. In water, heat transfer is mainly treated by conduction and convection, although for the initial nanoseconds of the heat transfer process, the conduction term has a higher impact than the convection term (in reference [19], it is stated that the current velocities due to natural convection are of the order of 0.5 pm/ns, while the temperature change due to conduction can reach several nanometers within a few nanoseconds). Therefore, as a first approximation, only heat conduction in water will be considered.

2.1.2 Heat conduction

In the case of heat conduction, the rate of heat flow $\vec{Q}$ in a certain direction has been proved experimentally to be proportional to the area A normal to the direction of the flow and to the temperature gradient ∇T in that direction. Although the experimental demonstration of this fact was done initially by J. B. Biot, the mathematical description was published in 1822 by the French mathematical physicist Joseph Fourier[15, 16]. This description, known as Fourier's Law, can be written as

$$\vec{Q} = -kA\nabla T \quad , \tag{2.1}$$

where the variable k is the thermal conductivity[3] of the medium, a positive quantity.

The rate of heat flow per unit area is the heat flux $\vec{q}$. Equation 2.1 can then be written in terms of the heat flux as

$$\vec{q} = \frac{\vec{Q}}{A} = -k\nabla T \quad . \tag{2.2}$$

This equation implies that a negative temperature gradient results in a positive heat flow and vice-versa.

This equation is valid for the particular case of a system with constant k and no source of energy within the system. To derive a more general equation for the heat conduction, it is necessary to take into account the energy balance in the system due

[1] As can be verified in several books: pages 20-22 of reference [15] and pages 5-7 of reference [18].

[2] As can be verified in reference [16], pages 65-68.

[3] The thermal conductivity of a material is a function of its physical structure, thermodynamic state and chemical components, depends strongly on temperature and less strongly on pressure[15].

to heat exchange by conduction, heat generation within the system and the increase of internal energy, i.e.,

$$\begin{pmatrix} \text{Heat gain} \\ \text{by conduction} \end{pmatrix} + \begin{pmatrix} \text{Energy} \\ \text{generation} \end{pmatrix} = \begin{pmatrix} \text{Increase of} \\ \text{internal energy} \end{pmatrix}. \tag{2.3}$$

Developing this equation, as in chapter 2 of reference [16], it is possible to obtain the following general heat conduction equation

$$-\nabla\vec{q} + g = c\rho\frac{\partial T}{\partial t} \quad , \tag{2.4}$$

where c is the specific heat of the material, ρ is the density of the material, $\frac{\partial T}{\partial t}$ is the variation of the temperature T with time t and g is an external energy source per unit of volume within the system.

Taking into consideration equation 2.2 and for a medium in which the thermal conductivity k is constant in temperature and space, the previous equation can be simplified to what is denominated as the Fourier-Biot equation[15]

$$k\nabla^2 T + g = c\rho\frac{\partial T}{\partial t} \tag{2.5}$$

It is important to highlight that, the heat conduction equation can only be solved analytically for some simple systems, such as the ones presented in section 6.2. For complex systems, equation 2.5 must be solved numerically.

Chapter 3

Overview of the production, preparation and use of gold nanostructures for biomedical applications

In the last few decades, gold-based nanostructures have been investigated for different applications. Gold nanoparticles have been considered for medical applications, such as imaging and therapy, because they are good scatterers or absorbers in the visible-near-infrared spectral range and their surface can be easily functionalised.

The work presented in this thesis addresses outstanding issues related to the use of gold nanoparticles as heat sources. Therefore, this literature review will start with a summary of the main methods used to produce unfunctionalised gold and gold-coated nanoparticles. Following this, some methods to coat gold nanoparticles with different proteins are also discussed. After, a short review of some of the studies done on uses of gold nanostructures for biomedical applications and some results concerning the studies of heat transfer relevant for these applications are presented.

3.1 Production of gold nanoparticles

Experimentally, there are several chemical or physical methods to create gold nanoparticles. Some are "green approaches"[20], as they do not rely on hazardous chemicals, while others are less environmentally friendly. Depending on the approach, particles of

different sizes (in the range of a few up to some hundreds of nanometres in diameter), shapes (e.g., pyramidal, spherical, rod-shaped), compositions (pure gold, core-shell or gold-coated), surface charges and chemistries can be made. In this section, a short description of some methods used to make nanoparticles is presented.

For one reported environmentally friendly approach, a solution containing sodium tetrachloroaurate, $NaAuCl_4$, is added to an infusion of Darjeeling tea and in a matter of minutes, gold nanoparticles of 15-45 nm in diameter are created. Due to the phytochemicals present in the infusion, this production method enables the simultaneous phytochemical-coating of the gold nanoparticles. This coating contributes to the non-agglomeration and stabilisation of the particles, and when used *in vitro* shows very good affinity towards cell receptors.

One of the main chemical approaches used to produce gold nanoparticles is by chemical reduction in aqueous solution[3]. At the boiling point of a heated diluted solution containing chloroauric acid ($HAuCl_4$), a small quantity of citric acid ($C_6H_8O_7$) is added while the mixture is vigorously stirred. After a short period of time, gold nanoparticles are produced. This is usually identified by the change in colour in the solution, from transparent or blue to red or pink, depending on the distribution of nanoparticle sizes. In the case of reference [3], the particles obtained are rod-shaped, with an average length of 38 nm and a mean aspect ratio of close to 1.3.

A physical method employed quite commonly uses a muffle furnace to heat up a surface coated with a thin film of gold. The cooling process can then be controlled and performed at a slow rate, resulting in the formation of gold nanoparticles. At low annealing temperatures, this is likely due to atomic diffusion on the surface and partially due to evaporation-condensation mechanisms and bulk diffusion. At higher annealing temperatures, the nanoparticle formation seems to be due to the combination of grain boundary and bulk diffusion, a process known as grain-coarsening. An alternative explanation has also been proposed: nanoparticles may form due to the temperature dependence of the interfacial energies of the three media present in the system, which leads to local surface deformations[21]. With this method there is the risk of diffusion of some atoms from the substrate to the nanoparticle, which may change the nanoparticle's properties and crystal structure[22]. Spherical nanoparticles of sizes between 30 and 400 nm are commonly obtained with this method.

Nanoparticles with only an outer layer of gold (either a core-shell or a gold-coated particle), may be produced by first functionalising the core nanoparticles with an amine-terminated compound (e.g., for the case of silica core nanoparticles in [23]). Gold

colloids (2-3 nm) are then attached to the amine and finally, a continuous shell is obtained by reduction of a solution containing chloroauric acid onto the attached small colloids in the presence of formaldehyde. For other methods regarding the production of core-shell nanoparticles, refer to [13], [24] and references therein.

Nanoparticles of distinct shape, as in the case of gold pyramids[25] in which the pyramid base has dimensions of 100-300 nm but the pyramid tip is around 1-10 nm in size, can be produced using a combination of techniques. Electron-beam deposition, a layer-by-layer approach, is used to deposit chromium and gold, while phase-shifting photolithography and wet-chemical etching are used first to create the chromium masks, and subsequently to remove these masks, once the electron-beam gold deposition is complete. This top-down nanofabrication is a good example of how combinations of methods allow the production of anisotropic structures that are highly uniform in shape and size, and multifunctional.

For solution-based nanoparticle production methods, the main factors to take into account are the temperature and the concentration of any external agents (e.g., citrate, organic coating). As for production methods based on thin films, the main production factor is the annealing temperature used, the amount of time the material is kept at that temperature and film-substrate properties (for instance, gold film shape, size and thickness, presence or not of an adhesion layer on the substrate). Chapter 5 will explore the effect of annealing temperatures and cooling rates on the nanoparticle production, as these factors should have a strong influence on the nanoparticle crystal structure, and are still not fully understood.

3.2 Preparation of gold nanoparticles functionalised with proteins

The organic coating of the nanoparticles can happen at a second stage, after the nanoparticle production, or may happen simultaneously. In the next few paragraphs both approaches will be exposed.

A method that allows the production of thiol-derivatised gold nanoparticles employs a two-phase liquid-liquid environment[26]. In brief, a solution containing chloroauric acid is transferred to an organic solution of toluene, while using a phase-transfer catalyst (tetraoctylammonium bromide). Once this transfer is completed, dodecanethiols are added to this mixture. At this stage, a reducing agent (sodium borohydride) is

introduced in the system, under vigorous stirring. In a matter of seconds, the organic phase changes colour from orange to deep brown. Finally, the organic phase is separated from the dark brown precipitate.

Proteins and antibodies can also be attached to gold surfaces after the gold structure production. This attachment can happen either by electrostatic interaction (as is the case for the albumin protein which has several positive amine groups and is thus attracted to the negative charge of components adsorbed to the gold surface) or by covalent thiol bonds between the amino acid cysteine and gold[23].

For *in vivo* applications, noncovalent approaches should be avoided[27]. Blood contains a high variety of proteins that can compete with the already coated antibodies to bind to the gold nanoparticles. This can then accelerate the dissociation of the attached antibodies, leading to nonspecific binding. Therefore, the covalent bonding[2] method is described here. A redox solution with a phosphate buffer at a weak basic pH is created in order to suspend the proteins and deprotect the terminal thiol. After some time in this reducing solution, the proteins are desalted to obtain deprotected proteins in a pure water solution. This desalted solution is then added to a solution containing gold colloids and shaken for several hours at a low frequency. After this period, the solution of protein-gold nanoparticles is buffered to an almost neutral pH and it is left to equilibrate for some time. For a period of some hours following this, the concentration of salt (NaCl) is gradually increased, while the solution is sonicated, in order to keep the particles dispersed. The addition of salt allows the attachment of the proteins to the nanoparticle surface and by varying the salt concentration, the coated protein density can be controlled[2]. Subsequently, the solution is shaken at low frequency for several more hours, to allow the production of fully functionalised protein-gold nanoparticles. Finally, to separate the coated nanoparticles from all the unbounded proteins, several centrifugations, supernatant removals and resuspensions in solution with anionic surfactant are executed. This entire procedure may need to be performed in the dark, in case a light sensitive dye is used (to prevent photobleaching). The protein coating layer can be 5 to 11 nm thick, as measured experimentally for several types of proteins[2, 23].

The density of proteins coated on the gold nanoparticle surface, which can be measured experimentally by fluorescence and absorbance methods[2, 28], depends on the nanoparticle as well as the salt concentration. Particles with smaller sizes can accommodate a higher number of proteins per unit area, although this density varies with the salt concentration. High concentration of salt can screen the charges of the organic components during the adsorption process, leading to an increase of the number of pro-

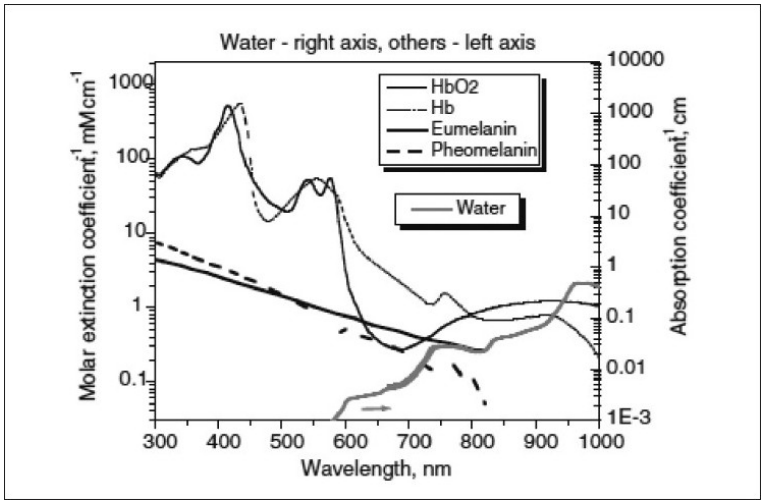

Figure 3.1: Absorption spectrum of various components of living tissue. Image used from Kumaresan *et al.*, reference [29], with permission.

teins per unit area [28]. As the particle size increases, the density of proteins decreases, reaching a limit value when the particle radius is bigger than 30-50 nm[2]. Although not explored in this thesis, the effect of the protein distribution on the nanoparticle surface when these are used as heat sources is mentioned in chapter 9, as an interesting issue to address in the future.

3.3 Gold nanoparticles for diagnosis and therapy

For any of the biomedical procedures mentioned in the introduction, the nanoparticles used should be inert, biocompatible and should respond to radiation in the near infrared (near-IR) spectrum region. This frequency range is preferable because it is poorly absorbed or scattered by living tissue, as figure 3.1 shows for the case of melanin and red oxyhemoglobin (HbO_2). Therefore, near-IR radiation maximises contrast per dose, i.e. decreases tissue attenuation and autofluorescence from nontarget tissues. Furthermore, the nanoparticle must be developed to efficiently exit the body, by biodegradation or intact excretion (renal clearance or liver sequestration)[13].

When light shines on gold nanoparticles it can either be mainly absorbed (by photon-electron interaction) or scattered. If the frequency of the light source matches the collective plasmon resonance of the nanoparticle, the majority of the incident radiation is absorbed by the particle[11], while if this resonance is not reached, then light will be mainly scattered. As this surface plasmon frequency strongly depends on the size of

the nanoparticle, nanoparticles of identical composition but different radii will lead to markedly different effects[30].

Radiation scattered by the particle, either forward (in the direction of the beam) or backwards, can be used for diagnostic purposes. In particular, backscattered radiation can be used for imaging by confocal reflectance microscopy, laser scanning microscopy, spectrophotometry and optical coherent tomography. These techniques can provide useful insight on inflammatory, degenerative or neovascular disorders and could be used for early cancer detection[4]. The use of optical fluorescence imaging techniques in surface-based ($<$ 1 cm) clinical applications such as open-surgical interventions, among others, also seems to be a promising application for gold nanoparticles[13]. Experimental results[11] with radiation of 532 nm seem to suggest that for particles bigger than 20 nm the scattering effects becomes considerable, while for smaller sizes the majority of radiation is converted to heat. Computational studies[4] show that, although the angular intensity map is symmetric, shorter wavelengths (532 nm) reveal a greater scattering for particles with radius of 20 to 75 nm, while for bigger particles with a radius of 75 to 100 nm, the scattering effect is greater for longer wavelengths (800 nm). Similar studies on core-shell silica-gold nanoparticles[4] reveal that, for the smaller wavelengths (532 nm), scattering increases with the increase of the shell thickness, with forward scattering being greater than backscattering. For the longer wavelengths (800 nm), a decrease in scattering is obtained, with the intensity of the backscattered radiation always higher than the forward scattered radiation.

When the objective is to use nanoparticles as heat sources inside tissues, it is desirable that the nanoparticle has a strong, narrow and tunable absorption close to the near-IR region. Computational results[4] show that for gold particles with sizes of 5-100 nm, absorption is greater for shorter wavelengths (532 nm) than for longer wavelengths (800 nm). When the nanoparticles are core-shell silica-gold, an increase in the radiation absorption is verified for the shorter wavelength (532 nm), while for a longer wavelength (800 nm) a decrease in the absorption is obtained. Experimental studies[11], using photocalorimetric methods with continuous wave lasers of wavelength of 532 nm and gold nanoparticles of 20 nm diameter, show a very high efficiency in the light to heat conversion for several laser modulations. Studies also show that nanoparticle aggregates present, besides the transverse band due to the plasmon mode of the individual nanoparticles ($\approx$ 520 nm), a near-IR absorption band (typically from 650 until 850 nm). This band tends to be inhomogeneously broadened due to different sizes and structures of the aggregation of nanoparticles[31]. Therefore, careful considera-

tions need to be taken in the production and use of nanoparticles, to be sure whether absorption occurs due to the individual particles or their aggregates. More promising nanoparticles are hollow gold nanospheres, where the combination of shell thickness and diameter allow the tuning of the absorption peak between 550 and 820 nm[31]. Hollow nanoparticles with shell thickness of a few nanometers and sizes from 30 to 50 nm provide a tunable absorption peak in the visible near-IR region ($\approx$ 800 nm)[32]. When coated with antibodies, the hollow nanoparticles showed no aggregation and a small blue shift ($\approx$ 18 nm) on the absorption spectra[33]. Hence, their strong absorption in the near-IR region, associated with their small size, spherical shape and easy conjugation with organic components make these nanoparticles very good candidates for biomedical applications. The *in vitro* and *in vivo* experiments of these nanospheres targeted with antibodies or specific peptides and proteins demonstrated a very effective use for photothermal ablation treatments[33], with results up to eight times better than with solid gold nanoparticles[32]. The magnitude of this improvement was attributed to much stronger near-IR absorption and more effective photothermal conversion.

The matching between the wavelength of the external light source and the surface plasmon resonance of the nanoparticle or nanoparticle aggregate determines the temperature profile of nanoparticle during and after the laser irradiation. For that reason, in section 8.2 of chapter 8, the effect of the nanoparticle temperature on the overall heat transfer is investigated.

3.3.1 Studies on cell uptake and cytotoxicity

A compound can enter a cell by several mechanisms, depending, among other aspects, on its size, shape, surface charge and arrangement of chemical groups[34]. Smaller and nonpolar molecules, a few atoms in size, can passively diffuse through the membrane layer, while for nanometre-sized proteins and ions, specialised membrane-transport protein channels are used. For bigger molecules and most nanomaterials (where nanoparticles are included), the uptake into the cell seems to be due to endocytosis[34].

For certain diseased tissues (e.g., a tumour), enhanced nanoparticle uptake can occur due to an abnormal lymphatic system and a leaky vasculature. These inherent properties allow for enhanced permeability and retention effect of smaller nanoparticles in the tumour relative to the healthy tissue. Also, some cancer cell membranes contain different and/or more receptors than healthy cells. Consequently, nanoparticles coated with specific organic materials can directly attach to these receptors and increase the

rate of endocytosis[35]. During endocytosis, part of the cellular membrane rearranges to envelop the nanomaterial, isolating it from the cell cytosol. This restricts the location of the nanoparticle within the cytosol, which may be undesirable. This effect can sometimes be reversed by co-internalising a membrane-disrupting agent together with the nanoparticle. The downside is that the endocytosis of these artificial/synthetic systems can create pores in the cell membrane that can lead to cellular toxicity, by destroying the ionic and protein balance between the interior and the extracellular medium.[34]. A way to prevent this cell toxicity is by either changing the nanoparticle size and/or shape in order to change the uptake mechanism or by modifying the surface-structure of the nanoparticle to reduce the impact on the formation of pores, the latter being a better way to guarantee the usage of the nanoparticle in a wider range of conditions.

As for uptake efficiency[34, 36], nanoparticles with smaller surface area seem to more easily use endocytic pathways. For example, spherical nanoparticles are internalised via endocytosis up to 500% more than rod-shaped particles. In terms of sizes, spherical nanoparticles with diameters of the order of 50 nm seem to present the best uptake. Smaller nanoparticles may extravasate or pass through the tumour vasculature, to the extreme of nanoparticles of around 10 nm in diameter being detected in several organs[35]. Experimental results[37] with pegylated gold nanoparticles with 20, 40 and 80 nm diameter indicated that the smaller nanoparticles had a higher tumour uptake, related to their prolonged resident time in the blood and their ability to extravasate from the tumour blood vessels . Regarding the spatial arrangement of the coating, characterised using scanning tunnelling microscopy, ordered protein coatings show a better efficiency of particle-cell-membrane interactions than randomly arranged ones, with a higher density of protein coating being related to an increased cell uptake[34]. Studies referred in [35] also point to the importance of the length of the ligand attached to the nanoparticle, with shorter targeting ligands enhancing the efficiency of the nanoparticle delivery due to the smaller overall size of the nanoparticle. As for surface charge, neutral nanoparticles minimise unforeseen nanomaterial-biological interactions[34] and increase blood circulation time[35]. Charged surfaces enhance cell uptake, although different conclusions are found in the literature. Some[34] argue that the higher uptake rate is obtained with cationic-coated nanoparticles, although other sources[35] suggest that positively charged organics coatings do not specifically stick to cells and strong negatively charged coatings enhance liver retention. To increase the cell uptake, coating the nanoparticle with serum proteins or other natural cell-penetrating motifs (as neutral

and hydrophilic ligands, e.g., poly(ethylene glycol) PEG) is often done, together with ordered spatial arrangement, in order to enhance nanoparticle dispersion and receptor-mediated endocytosis, minimise nanoparticle aggregation and avoid unwanted protein adsorption[34, 35]. Furthermore, results[27] also suggest that nanoparticles coated with a mixture of specific proteins and natural cell-penetrating motives allow simultaneously specific cell targeting and avoid nanoparticle filtration by the reticuloendothelial system of the body.

All of these points argue to the advantage on the use of spherical particles for biomedical applications. For this reason, the nanoparticle shapes created in chapter 5 and used in chapter 8 approximate spheres.

3.3.2 Studies on living body circulation and clearance

The particle size is a key factor determining the lifetime of the nanoparticles in the circulatory system and the mechanism by which they are cleared by the body. Results presented in reference [35] argue that nanoparticles between 5 and 100 nm in diameter are not significantly captured by the liver, spleen or kidneys. On the other hand, groups cited in reference [13] and results presented in reference [38] show that reasonably long circulation lifetimes are obtained for nanoparticles with sizes between 3 and 7 nm in hydrodynamic diameter[1]. Smaller particles lead to nonspecific tissue dispersal and extravasation (i.e., increase on background fluorescence and potential prolonged retention), while larger probes tend to accumulate in the liver, leading to an eventual hepatobiliary excretion. Since the liver is the more time consuming clearance route, the increased retention of the nanoparticles in this organ may allow possible interference with other imaging assessments and cause prolonged exposure[13]. The same group verified that smaller particles (3.3 nm diameter) are more quickly and completely excreted (after 48 hours, 73% of particles were out of the system) than the larger particles (6 nm diameter) (only 64% of particles were excreted in the same period). Experimental results[37] with pegylated gold nanoparticles with 20, 40 and 80 nm diameter considered the effect of the size of the nanoparticle and of its organic coating in terms of blood clearance. Their results indicated that smaller nanoparticles had significantly higher activity in the kidneys and intestines than the bigger ones, which were rapidly

[1] According to [39], the hydrodynamic radius is the hypothetical radius of a hard sphere that presents the same diffusion characteristics as the particle under analysis. As most of the particles used in the several biomedical studies are not spheres, the hydrodynamic radius gives an apparent size of the dynamic hydrated/solvated particle.

captured by the liver and spleen. Nevertheless, the authors also pointed out that the slower blood clearance of the smaller nanoparticles could also be due to the higher surface PEG density achieved in the smaller particles, arguing that the compact PEG layer could effectively insulate the nanoparticles from nonspecific binding of plasma proteins, resulting in reduced liver uptake.

In terms of the surface charge, work from several groups, cited in reference [13] and reference [35], argues that zwitterionic or, preferably, neutral surfaces are more bioinert, allow an extended blood circulation time and a more effective clearance via the kidneys, while charged probes tend to increase the opsonising response (i.e., the susceptibility to be ingested by phagocytes) from the environment (e.g., serum proteins), causing a growth in probe size and preventing renal excretion.

Hence, there is quite some variability in the size of the nanoparticle that can be used in biomedical applications, as long as the total surface charge is zero. For this reason, the studies presented in chapter 8 use several sizes of neutral nanoparticles, in systems of hot particles embedded in water.

3.3.3 Other aspects relevant for the use of nanoparticles on bioapplications

For biomedical applications, coating the nanoparticle with specific proteins is often necessary. As part of the coating process (and as mentioned in section 3.2), it is necessary to centrifuge the solutions containing both nanoparticles and proteins in order to separate the excess proteins from the nanoparticles. Multiple centrifugations can lead to loss of protein coating[40], implying a change in the nanoparticle surface properties that can affect the outcome of the nanoparticles application.

Nanoparticle dispersion is another important factor to be considered, as previously motivated in page 26. According to some studies[40], the protein coating, besides increasing the compatibility of the gold nanoparticles in biological media and allowing the adaptation of the particles to different bioapplications, also minimises the nanoparticle aggregation. This a very convenient advantage since, as mentioned above, the optical properties change with the size of the gold aggregate. The protein coating also minimises the cytotoxic effect of the nanoparticle assemblies.

Furthermore, some experimental work[41] with ferromagnetic nanoparticles *in vitro* and *in vivo* indicates that inducing an hyperthermia state might not be enough to treat some tumours. For instance, the repeated heating of the tissues to hyperthermia

temperatures triggers the release of heat shock proteins[35], which are proteins involved in the folding and unfolding of other proteins. Therefore, in some cases, chemotherapy treatments may be also necessary in combination with the hyperthermia treatment using a heat shock protein inhibitor. This inhibitor has a antitumour effect by reducing the cells thermotolerance, hence increasing the cells susceptibility to hyperthermia.

As mentioned above in section 3.2, one of the issues that is addressed in this thesis is the influence of the identity of the organic layer coating the nanoparticles on the heat transfer between the nanoparticles and their surrounding medium.

Changes in coating density are also important issues to explore with computational models, as the transfer of heat through the interface may suffer changes as well as the temperature profile. Due to the project's limited duration, this study was not done.

3.4 Heat transfer studies

If the frequency of the light source shining on the system of gold nanoparticles in a medium matches the collective conduction band electron oscillation, a good part of the radiation will be absorbed by photon-electron interaction. This energy will be distributed by electron-electron scattering within 10-50 fs. Within a few picoseconds, the lattice temperature starts to increase due to electron-phonon interactions, reaching thermal equilibrium within 10-50 ps[42]. As the temperature of the particle increases, this accumulated heat can be propagated to the surrounding medium by phonon-phonon coupling and a thermal equilibrium between the particle and the surrounding fluid can be achieved within nanosecond time scales, depending on the particle size and laser pulse intensity[43]. Studies of heat transfer in a system containing nanoparticles in liquid media have been performed by several groups and different characteristics and parts of the system deserved special attention, as will be discussed in this section.

Experimental results[3] show that gold nanoparticles can undergo a shape change from rods to spheres at temperatures of 1213 K, below the melting point of gold (1337 K), with increased magnitude of the effects for bigger laser fluences. In some cases, the creation of smaller nanoparticles by what the authors call "laser-induced size reduction" was also verified. Under these conditions, the water surrounding the gold nanoparticle may reach temperatures close to the critical temperature (T_{cr} = 647 K), and a vapour phase is formed around the gold nanoparticle in an explosive manner[44, 45]. This vapour layer seems to form for all the sizes of nanoparticles tested (9-110 nm

in diameter), although for bigger nanoparticles the change in phase occurred at lower water temperatures. Studies of gold nanospheres in water using experimental[46] and finite element[47] methods showed that a quasi-steady temperature profile, without a vapour layer formation, can be established with low intensity and long laser pulses. If the laser intensity increases, a phase-change from liquid water to vapour occurs around the nanoparticle. Once this new phase is present, any additional increase in laser intensity does not significantly change the temperature of the nanoparticle or its surrounding medium, since the vapour layer shields the hot nanoparticle from the cold liquid water.

The presence of an explosive vapour layer led some authors to consider the use of pressure waves as a mean of causing mechanical damage at long range distances from the nanoparticle[48]. Their computational results with nanoparticles of 50 nm diameter heated with lasers of several fluences showed that the lengths at which the pressure wave and the thermal spikes should be intense enough to cause any mechanical or thermal damage are within distances comparable to the particle diameter. Thus it is unlikely to be a possible mechanism for mechanical damage.

Computational studies using finite elements to simulate gold nanorods in water and analytical models have clarified the timescales and temperature ranges of heat transfer in nanoparticle-water systems. When long laser pulses are used in a system with gold nanorods[42], the water surrounding the nanorod reaches a temperature close to the critical temperature of water in around 50 ps. The thermal equilibrium between both parts of the system is reached approximately 500 ps after the laser pulse. Much smaller temperature rises have been reported using shorter pulses. In the same study[42], when multiple laser pulses are emulated, a steady temperature rise of 3 K of the water layer surrounding the nanoparticle is achieved within 50 ns and is sustained throughout the duration of the simulation. Between pulses ($\Delta t = 12.5$ ns), the temperature of the gold and of the surrounding water equilibrates before the next pulse. Analytical approaches based on experimental results[11], which compare the relevance of the nanoparticle concentration and of the laser fluence on the heating of a system of gold nanoparticles in water, reveal that a considerable overall temperature increase of the medium is due to the combined heating effects of many nanoparticles. For high laser fluences in media with low concentrations of gold nanoparticles, a small temperature increase of the overall system is obtained, although a large temperature increase close to the nanoparticle is reported. Similar systems were also analysed experimentally[49] by pump-probe spectroscopy, focusing mainly on the effect of the nanoparticle size on the characteristic time scale associated with the energy dissipation from the nanoparticle

to the surroundings. Their results reveal an independence of the relaxation time on the initial temperature of the particle, but a variation with the square of the nanoparticle radius. In particular, the relaxation time varied from almost 400 ps, for the 50 nm diameter particle, to 10 ps, for the particles with 4 nm in diameter. In addition, for these smaller particles, the relaxation time of the energy dissipation was comparable to the electron-phonon coupling time scale of a few picoseconds, implying that a considerable energy loss happens before the electrons and phonons within the particle are in thermal equilibrium.

The effect of the introduction of an additional organic layer to gold structures has also been studied in terms of heat flow. Experimental measurements[50] on gold surfaces heated to temperatures up to 1075 K and coated with alkanethiolate chains show that the chains remain bonded to the gold surface even at such high temperatures, most probably due to the short duration of the temperature jump. A region at the base of the alkanethiolate chain of ≈ 0.8 nm in length, which corresponds to four carbon segments, is estimated to be involved in the heat conduction from the gold. This is in agreement with findings, reported in the same reference, stating the delocalisation of the heat-carrying vibrations over four or five carbon segments in short-chain alkanes. From this initial step, the velocity of heat propagation through the alkanethiolate chains was estimated to be of 0.95 km s^{-1}, revealing a small resistance on the heat flow through the organic layer.

More experimental studies[51], performed in systems of self-assembled monolayers (SAMs) sandwiched between gold and quartz (Qz) slabs, demonstrated that the bonding chemistry can modify the heat flow through the system, as well as the system stiffness. A stronger covalent bonding between the SAMs and the gold substrate increased the stiffness in the system. Also, the heat transfer through the interface could be directly tuned by changing the density of covalent bonds between the SAM and gold substrate. Moreover, the rate of heat transfer at the interface, hereafter referred to as the heat transfer coefficient, was also measured. They estimated values of 36-39 MW m^{-2} K^{-1} for weaker interactions, as in the Au/CH_3-C_{11}-Si/Qz and Au/NH_2-C_{11}-Si/Qz systems, increasing to 47 MW m^{-2} K^{-1} for bromine-terminated surfaces. The stronger value of 68 MW m^{-2} K^{-1} was measured for the system with covalent bonds (Au/SH-C_{11}-Si/Qz).

The experimental study[52] of the thermal properties of metal nanoparticles (diameters ranging from 4 to 26 nm) embedded in glass show that the cooling processes were controlled by the heat transfer at the interface between the particle and the glass and by the heat difusion in the glass matrix. For the particular case of a gold nanoparticle

of 9 nm in diameter, the heat transfer coefficient for the case of a gold-glass interface is estimated to be approximately 100 MW m^{-2} K^{-1}.

Some experimental studies have also been performed regarding the effect of the coating of metal nanoparticles in the heat transfer. For the case of citrate stabilised Pt particles (diameter $\approx$ 10 nm) solvated in water[53], the heat transfer coefficient was measured to be around 130 MW m^{-2} K^{-1}. Further studies by the same group[54], with two organic-coated AuPd nanoparticle (diameter $\approx$ 4 nm) embedded in water, determined the heat transfer to be around 250$\pm$90 MW m^{-2} K^{-1} and 145$\pm$55 MW m^{-2} K^{-1}. In the same reference, larger nanoparticles (diameter $\approx$ 20 nm) of organic-coated Au-core/AuPd-shell nanoparticles have a heat transfer coefficient of 230$\pm$50 MW m^{-2} K^{-1}. Due to the very large uncertainties associated with the heat transfer coefficients measured in experiment, the authors concluded that the heat transfer between the metal and liquid is insensitive to the structure and chemistry of the organic-coating, although they admit surprise towards such result. Furthermore, their results suggest that the heat transfer between the metallic nanoparticle and water is at least one order of magnitude larger than in systems where the particle is embedded in an organic medium. Similar conclusions were obtained with heated gold surfaces coated with alkanethiolates of different lengths[50], in which a heat transfer between the gold and the alkanethiols of 220 MW m^{-2} K^{-1} was measured. On the other hand, other experiments[55] with gold nanorods with different kinds of coatings (PEGs of different lengths, alkanethiolates acids of different lengths, etc.) embedded in solutions with the organic compounds of the coating affirm that the heat transfer at the interface does not significantly depend on the length of the coating, but it does depend on the surface chemistry. Their evaluation of the heat transferred at the interface, which includes the transfer at gold-organic interface and the transfer through the organic and at the organic-solvent interface, gives values of 175 ± 75 MW m^{-2} K^{-1} for the case of $CH_3(CH_2)_9COOH$ (mercaptoundecanoic acid), 163 ± 35 MW m^{-2} K^{-1} for the case of $CH_3(CH_2)_{14}COOH$ (mercaptohexadecanoic acid) and infinity for the remaining types of coatings.

Slab systems can be used to focus on the effect of the interface in the heat transfer. Experimental results in [56] have shown that planar gold functionalized with 1-octadecanethiol (C_{18}), in order to make the surface hydrophobic, has a heat transfer coefficient of 50 ± 5 MW m^{-2} K^{-1}, while planar gold functionalized with 11-mercapto-1-undecanol ($C_{11}OH$) becomes hydrophilic and measures 100 ± 20 MW m^{-2} K^{-1}.

Finite element methods or analytical approaches cannot readily capture the phase transitions experienced by the gold or its surrounding medium, when non-equilibrium

conditions, such as difference in temperatures, are imposed. A more natural way of studying these phenomena is by using molecular dynamics. This computational method also has the advantage of allowing the study of the fundamental heat transfer mechanisms, as it does not require any prior knowledge of the heat transport[57].

Results obtained with a general nanoparticle of a few nanometres in diameter embedded in a general fluid[58] show that the fluid next to the nanoparticle can be heated well above its boiling point without experiencing a phase change, due to the increase of the curvature-induced pressure of the fluid close to the nanoparticle. The continued increase of the nanoparticle temperature also led to a saturation point in the heat flux of the system. Studies on flat surfaces, where effects of curvature are suppressed, also demonstrate that, at a critical heat flux, a vapour layer develops, followed by a heat flux drop[58]. Also, results obtained with a slab system of two general solid slabs separated by a general fluid demonstrated that the heat transfer at the interface increases with the wetting of the liquid to the solid[59].

In more particular studies, such as in reference [60], several liquid-liquid interfaces are simulated and each of the heat transfer coefficient is determined. Their values are between 65 ± 10 MW m^{-2} K^{-1} for water-octane interface and 370 ± 40 MW m^{-2} K^{-1} for hexane-surfactant tail ($CH_3(CH_2)_{29}OH$). For the case of water-surfactant head (OH groups), their heat transfer coefficient is determined to be 300 ± 40 MW m^{-2} K^{-1}, which they justify on the strong coupling between the water and the hydroxyl group. The acceptance and donation of hydrogen bonds between the hydroxyl "head group" and the water, which is visible in their simulations, leads to a visible peak in the mass density distribution at the interface. They also verify a very small temperature drop through the surfactant chain. As for their vibrational modes analysis, the systems with good heat transfer show overlapping low vibrational frequencies. Planar systems of self-assembled monolayers with a broad range of surface chemistries (from hydrophobic to hydrophilic) embedded in water[61] show values of the heat transfer coefficient at the water-SAM interface ranging from 40 MW m^{-2} K^{-1}, for hydrophobic surfaces, to 140 MW m^{-2} K^{-1}, for the hydrophilic surfactants. Solid-organics interfaces have also been investigated under equilibrium and non-equilibrium molecular dynamics. In references [62] and [63], the authors performed several studies with Au-SAM-Au junctions. In particular, they focused on the variation of the heat transfer coefficient at the Au-SAM interface with the temperature, external pressures, SAM molecule coverage and Au-SAM bond strength. Their results show that in such a system, the interface presents a bigger resistance than the heat conduction through the substrate or the organic com-

ponents. They found that the heat transfer coefficient increased with temperature, for temperatures lower than 150-250 K, reaching a plateau beyond this point. The authors also verified an increase on the low frequency vibration modes in the gold and organic components as the temperature increases, while only the organic components presented an increase on the intermediate frequency modes. This latter anharmonicity was attributed to suppress any further increase on the thermal conductance, therefore justifying the plateau reached. The effect of the variation of the external pressure or of the alkanedithiol chain length on the heat transfer coefficient was considered minimal. On the other hand, an increase on the SAM molecule coverage or on the Au-SAM bond strength was found to increase the value of the heat transfer coefficient. The heat transfer coefficients measured ranged from 200 to 420 MW m^{-2} K^{-1}.

In terms of curved systems, several studies have been undertaken with molecular dynamics tools. For instance, for ZnO nanoparticles solvated in tetradecane[64], a vapour layer around the nanoparticle was obtained for the case of extremely high heat flux. According to reference [65], gold nanoparticles (radius of 1.2 nm) embedded in octane and heated up to temperatures of 500 K presented a value of the heat transfer coefficient of around 100 MW m^{-2} K^{-1}, while as the nanoparticle temperature increased, this value reduced to 50 MW m^{-2} K^{-1} at 1200 K. Heat flows above 700 nW made the nanoparticle lose crystalline order and start to disintegrate, without the formation of a liquid vapour layer. When similar simulations were performed in water, the heat transfer coefficient varied from 170 to 150 MW m^{-2} K^{-1}. As the nanoparticle temperature increased, a diluted liquid layer, hotter than the critical temperature of water (650 K), surrounded the nanoparticle, although this layer never reached vapour density values.

In more recent years, the variation of the heat transfer coefficient at the interface with the particle size has been studied. Lervik *et al.*[66] used systems of alkane nanodroplets embedded in water and detected a strong reduction of the heat transfer coefficient from 250 to 90 MW m^{-2} K^{-1}, as the size of the nanodroplet increased from 2 to 12 nm in diameter. As for Hu *et al.*[64], ZnO particles, with radii between 10 and 30 Å were embedded in tetradecane and heated up with a extremely high heat flux. Their calculated heat transfer coefficients decreased from 35-40 MW m^{-2} K^{-1} for the smaller particles to 6-12 MW m^{-2} K^{-1}. As already explained in these two references, this dependence of the heat transfer coefficient with the size of the nanoparticle can be due to a surface tension effect. The surface tension and solid free energy increases with the radius of the nanoparticle, which leads to a stiffer interface and, therefore, a a lower heat transfer.

These results have addressed important issues such as the heat transfer in media with gold and water, the advantages of using protein coated gold nanoparticles, the size dependence of their use as heat sources and the importance of the different interfaces present in the system, among others. However some issues are still unexplored and simulations using molecular dynamics and analytical approaches can provide useful explanations and information. For instance, the main mechanisms responsible for the heat transfer in systems of embedded nanoparticles has not been greatly explored, and are addressed in chapter 6, by employing analytical and computational methods. In the same chapter, the heat propagated through the gold-water interface is quantified, by employing non-equilibrium molecular dynamics. Also, as this section shows, some studies have been done in terms of evaluating the heat transfer between different interfaces. As mentioned above, the few existing experimental studies investigating this issue report heat transfer coefficient values with very large associated uncertainty, which do not allow definitive conclusions to be made. Nevertheless, very few studies have been focused on the case of organic-coated gold structures in water and the influence of this organic coating in the heat transfer through the gold-water interface. Therefore, this issue is investigated in chapter 7. Furthermore, although the temperature distribution in systems of embedded hot particles has been reported by some groups, not many of those systems used atomistic detail to study the temperature variation in the water as a function of distance from the nanoparticle and with time, which we refer to in chapter 8. In the same chapter we also explore the effect of different variables, such as the nanoparticle size and temperature, on the heat propagation for the case of bare gold nanoparticles solvated in water, as this particular system has not been widely studied through molecular dynamics.

Chapter 4

Methodology

4.1 Molecular dynamics

The properties of a molecular system may be investigated using different, complementary methods. Experiments are the optimum standard but cannot single handedly yield all the desired information about any given system. On the one hand, most experimental techniques require analytical or computational models for the interpretation of measured quantities. On the other hand, most experimental techniques give spatially and/or temporally averaged information and do not give direct evidence on molecular scale mechanisms. A third limitation of experimental techniques is that few of them are surface sensitive, which limits our ability to investigate processes taking place at interfaces. Both analytical and computational models are used to address these limitations. Analytical models are most often utilised to gain insight into the spatially or temporally averaged behaviour of many systems, but frequently cannot be used to understand the molecular scale details of system behaviour. Particle-based computational models are the preferred option for this.

Particle-based computational models have become widely used in the last 20-30 years. In this approach, a system is simulated with atomic or molecular scale detail, and average values of its properties (temperature, pressure, configurational energy, etc.) are systematically taken, allowing the study of the evolution of the system and statistical prediction of its properties.

One of the computational methods available is molecular dynamics (MD). The idea behind MD simulations is precisely that it is possible to study the average behaviour of a many-particle system simply by computing the natural time evolution of that system

numerically and averaging the quantity of interest over a sufficiently long time[67].

In many aspects, an MD simulation is similar to a real experiment. In a real system, a sample has one or more of its properties (temperature, pressure, etc.) being monitored/controlled with a certain instrument (thermometer/thermostat, barometer/barostat, etc.) over time. To minimise the statistical noise of the instrument measurement, it is advisable to perform the data collection over a long period of time. In molecular dynamics the same concept is used. As the name suggests, the dynamics of the system (a solid, a liquid, a gas, a protein, etc.) is simulated over time. To perform the simulation, the initial configuration of the system and the interatomic potentials that govern the interactions between particles must be assigned. The force acting on each particle at each instant is solely determined by these potentials and the positions of the surrounding particles. Once the force acting on each particle is known, the coordinates and velocities of each of the particles can be propagated in time, according to Newton's equations of motion. To mimic experimental conditions, some of the system properties (e.g., number of atoms, volume, total energy, pressure, etc.) are kept constant. As the system reaches a steady state, that is, the overall properties no longer change, the ensemble averages (i.e., the averages over all possible states of the system), which are equivalent to the time average values when the ergodic hypothesis is assumed, are taken. In MD, the ensemble averages are assumed to be independent of the initial conditions of the system[67].

The MD code used and modified in the simulations is DL_POLY_3.09[68]. Now, some parts of this brief description are explored in more detail, namely the force fields used, the initialisation, force calculation and integration algorithm used and the ensembles used.

4.1.1 Force fields

As noted above, the interactions between the atoms in an MD system are determined by the interatomic potentials. In the following pages a short description of the interatomic potentials used to emulate the forces between the atoms in the system studied will be presented.

All parameters mentioned in this section are tabulated in appendix B.

Metallic potential

To simulate the metallic bonds between the gold atoms, the Sutton-Chen (SC) potential[69] was used. The SC potential is a derivation from the empirical N-body potential initially developed by Finnis and Sinclair[70](FS). This potential takes into account, beyond the short range interaction of the FS approach, a long range interaction given by a van der Waals tail. The N-body interaction is given in terms of the force between any pair of atoms, which is dependent on the interatomic distance between them and on all neighbours of both atoms. This potential has the form

$$V_{Au-Au}(r_{ij}) = \epsilon \left[\frac{1}{2} \sum_i \sum_{j \neq i} \left(\frac{a}{r_{ij}} \right)^n - c \sum_i \sqrt{\sum_{j \neq i} \left(\frac{a}{r_{ij}} \right)^m} \right] \quad , \tag{4.1}$$

where ϵ depends on the metal being simulated and has dimensions of energy, a is the lattice constant, r_{ij} is the interatomic distance between the atoms i and j, c is a dimensionless parameter, m and n are positive integers with $n > m$.

As already noticed by Sutton and Chen[71], this potential is not accurate enough to distinguish certain differences (e.g., the total energy difference between face-centered cubic (FCC) and hexagonal closed-packed (HCP) crystal structure), but it provides reasonable description of surface effects, in agreement with experimental observations[72].

Water-gold potential

To simulate the interaction between the gold and the water molecules, the potentials presented by Dou *et al.* in reference [45] were used. These potentials, which consist of gold-oxygen and gold-hydrogen interactions, are an adaptation of the potentials initially developed by Spohr[73]. The potentials developed by Spohr are based on a rigid metal surface, while this modified form allows the metal atoms to move and interact with the water molecules[74]. Dou modified the Spohr function so that the interactions are pairwise additive between the O and the H atoms in the water molecule and the metal atoms. So, the modified potentials have the form

$$V_{Au-H}(r) = \gamma D_0 e^{-2\beta_H (r - r_{e2})} \tag{4.2}$$

and

$$V'_{Au-O}(r) = D_0 \left(e^{-2\beta_O (r - r_{e1})} - 2e^{-\beta_O (r - r_{e1})} \right) \quad , \tag{4.3}$$

where D_0, r_{e1} and r_{e2} are adjustable parameters that translate the adsorption energy and the distance of the water molecules to the metal surface, respectively, obtained from experimental results[75], and β_O and β_H are chosen to give the same range and curvature as the original Spohr functions.

To gain computational efficiency, it is necessary to force the previous equation smoothly to zero. For the case of the gold-hydrogen potential, since it approximates to zero quite fast, no adaptation is necessary. As for the gold-oxygen potential, this is done by applying a switching term $S(r)$ to $V'_{Au-O}(r)$ so that this potential smoothly approaches zero at an appropriate cutoff distance. Therefore, the gold-oxygen potential becomes:

$$V_{Au-O}(r) = S(r)V'_{Au-O}(r) \quad , \tag{4.4}$$

where

$$S(r) = \begin{cases} 1 & r \leq r_{on} \\ \frac{\left(r_{off}^2 - r^2\right)^2 \left(r_{off}^2 + 2r^2 - 3r_{on}^2\right)}{\left(r_{off}^2 - r_{on}^2\right)^3} & r_{on} < r \leq r_{off} \end{cases} \tag{4.5}$$

and where r_{on} and r_{off} are the start and the end distances of the truncation function.

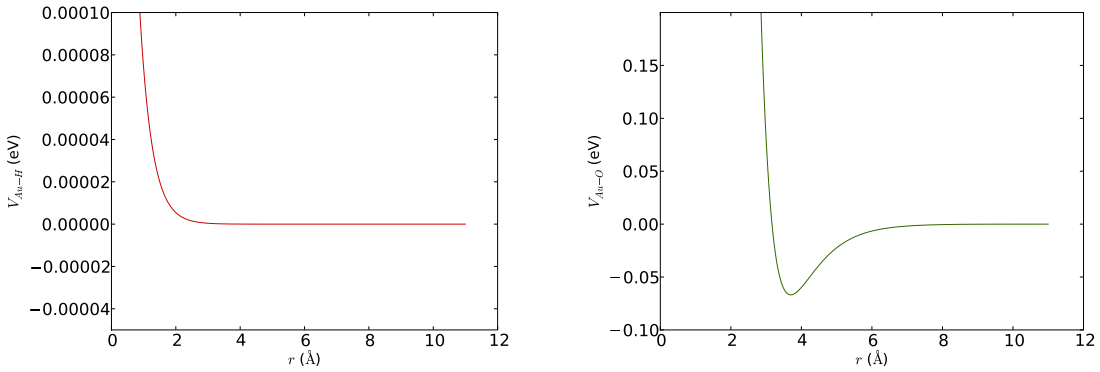

(a) Gold-hydrogen interatomic potential curve. (b) Gold-oxygen interatomic potential curve.

Figure 4.1: Water-gold interatomic potential plots, zoomed on the y axis.

These potentials have the standard repulsive short range term and attractive long range term, as illustrated in figure 4.1. Also, they have been used by different authors with good results. For instance, in reference [76], these water-gold potentials were used in Monte Carlo simulations of gold nanoparticles embedded in water. In this study, the

3D crystal structure of the simulated nanoparticles was used to directly demonstrate the ability of the atomic pair distribution technique to yield three dimensional structural information for materials of limited structural coherence, including nanoparticles in solution. Another study, in reference [75], the water-gold potentials were used to simulate the adsorption of water molecules around gold nanoparticles of several sizes. Their results indicated that the interaction energy between the gold nanoparticles and the water molecules is sensitive to the size of the nanoparticles, which has direct influence on the adsorption constant, defined as the ratio between the number of water molecules within the first hydration layer and the surface area of the gold nanoparticle. The increase of the adsorption constant with the decrease of the nanoparticle size was considered to be in good agreement with results provided by a Langmuir adsorption model and experimental ones. Therefore, as these two studies present good agreement with experimental results, these potentials were considered a good choice to describe the interaction between water and gold.

Potentials of this form are not included in the DL_POLY package used, therefore the values of these potentials were added to the simulation, in tabular form, as one of the input files. To verify that these potentials were correctly implemented in DL_POLY, the adsorption energy of water per gold atom was calculated. In order to do so, three systems were simulated: a full system consisting of a water slab between two gold slabs, a system with the water slab only and a system with the two gold slabs. Each gold slab was created as a perfect FCC lattice, so that its 2160 atoms were distributed over six (1 1 1) planes perpendicular to the z axis. The dimension of each gold slab was $50 \times 52 \times 14$ Å^3. The water box was also built as a lattice of water molecules, where the intermolecular distances were set to mimic the water density of 1000 kg/m^3. Its initial dimensions were of $47 \times 47 \times 50$ Å^3. Each system was then assembled by including the necessary parts in the same simulation box.The slab conditions were simulated by increasing the z component of the simulation box by approximately 30 Å and by using periodic boundary conditions in three dimensions. Each system was simulated for 100 ps, under NVT conditions. The temperature in each system was kept at 300 K by a Nosé-Hoover thermostat, with a relaxation time of 0.1 ps. Statistics were collected every 1 ps. A detailed description of the gold-gold, water-gold and water-water interatomic potentials and the cut off distances used is presented in section 4.1.1. At the end of the simulation, the total energies of the three systems were obtained and the water-

gold interaction energy per gold surface atom, eV/Au, was calculated by dividing the configuration energy due to the water and gold interaction, CE_{AuWa}, by the number of gold atoms that are on the surface in contact with the water slab , i.e.,

$$\frac{CE_{AuWa}}{\text{no. Au atms}} = \frac{E_{tot} - (KE_{Au} + CE_{Au}) - (KE_{Wa} + CE_{Wa})}{\frac{A_{total}}{A_{AuAtm}}} \quad , \tag{4.6}$$

where E_{tot} is the total internal energy of the system of gold and water slabs, KE_{Au} and CE_{Au} are the kinetic and configuration energies of the gold system only, KE_{Wa} and CE_{Wa} are the kinetic and configuration energies of the water system only. A_{total} is the total area of gold in contact with water and A_{AuAtm} is the area of a single gold atom, approximated to a square with side equal to the diameter of the gold atom.

The value obtained was $\approx -0.1\ eV/Au$. Several *ab initio* studies[77], density function theory[78, 79] and molecular dynamics[80] determined the adsorption energy of water monomers in gold surfaces to be between 0.1 and 0.13 eV/monomer. As can be verified, these values are very similar to the one determined. Hence, it can be assumed that the potential presented by Dou and added to the simulation represents reasonably well the water-gold bonding.

Water potential

In the system simulated, the potentials used to describe the interactions between the water molecules were standard versions. The water molecules were simulated as a rigid body, i.e., the vibration modes of the water molecules were non-existent. For this reason, the oxygen-hydrogen bond distances and the angles between the bonds were fixed. The latter were obtained by constraining the fixed distance between the hydrogen atoms.

The interactions between the water molecules were simulated by using the SPC/E (extended simple point charge, original) water model, which is composed by a short range Lennard-Jones potential and a long range electrostatic term (a Coulomb interaction potential). The electrostatic term describes the charge-charge interaction between pairs of atoms in any two molecules considered. The Lennard-Jones potential describes the dispersion and repulsive interactions between the two oxygen sites[45]. The total potential between molecules i and j is given as

$$V_{Wa-Wa}(r_{ij}) = V_{LJ} + V_{Coulb} = 4\epsilon_{LJ}\left[\left(\frac{\sigma_{LJ}}{r_{ij}}\right)^{12} - \left(\frac{\sigma_{LJ}}{r_{ij}}\right)^{6}\right] + \sum_{k\in i=1}^{3}\sum_{l\in j=1}^{3}\frac{q_{ik}q_{jl}}{4\pi\epsilon_0 r_{kl}} \quad ,(4.7)$$

where the summation is over partial charges k and l of the atoms, r_{ij} is the distance between oxygen atoms, ϵ_{LJ} and σ_{LJ} are positive constants, where the first measures the strength of the attraction and the second the radius of the repulsive core, and ϵ_0 is the permittivity of free space or vacuum permittivity.

In an MD simulation with periodic boundary conditions, it is not possible/advisable to simply truncate the electrostatic term due to its long-range nature. Therefore, the electrostatic term is determined by the particle mesh Ewald algorithm. The employed smoothed particle mesh Ewald (SPME) includes a real space component, described by a sum of gaussians up to a cutoff distance (r_{cut}), a reciprocal space term which uses a Fourier series and a self-interaction term. More information on this method, including details on each of these terms, can be found in the DL_POLY manual[68].

The SPC/E water model was chosen based on a study performed by Nilsson and Mark, reference [81], where the bulk water structure and dynamics of several commonly used water models were compared. In this study, Nilsson and Mark pointed out that the SPC/E model gives the best bulk water structure and dynamics results, i.e., the most satisfactory description on the bulk water diffusion from the simple models analysed. According to their results, the SPC/E model had a self-diffusion coefficient closest to experiment. In addition, the radial distribution function for the oxygen-oxygen distance for the SPC/E model had the closest agreement with the experimental data (e.g., it describes the curve of the second peak), although its first peak position occurred at a smaller distance than the experimental result. Furthermore, recent systematic studies with the SPC/E water model[82] revealed that its thermal conductivity approaches values close to experimental ones for temperatures between 500 K and 650 K. For temperatures lower than 500 K, the thermal conductivity is overestimated by up to 30 %, while for temperatures above 600 K, depending on the average water density, the thermal conductivity can be underestimated by up to 30%.

Gold-sulphur potential

The potential used to describe the covalent interaction between the sulphur head group of the alkanethiols and the gold surface was the one presented by Zhang *et al.* in

reference [83]. The interaction between the sulphur and the gold used a Morse potential, as it can mimic the bonding from a partially covalent bond. This potential is described as

$$V_{Au-S}(r) = D_e \left(e^{-\frac{S}{r_{eq}}(r-r_{eq})} - 2e^{-\frac{S}{2r_{eq}}(r-r_{eq})} \right) \tag{4.8}$$

where r_{eq} is the equilibrium position, D_e is the dissociation energy and S is a scaling factor. These parameters were obtained by fitting this potential to *ab initio* results for periodic systems, as the sulphur-gold distances and energy differences among adsorption sites, and experimental data, as binding energies.

Alkanethiols and functional groups potentials

The alkanethiols used in the simulations included atoms in two descriptions. The head group (S-) and terminal functional groups (-CH_3 and -COOH) used an all-atom description, while the alkane chain was built with united-atom beads, here named carbons, which describe CH_2 groups in an averaged manner. In terms of the several intra-molecular interactions, the chemical bond between neighbouring atoms, the angle between three consecutive atoms and the torsion related with four consecutive atoms were described by standard potentials. For the head group and the carbons from the alkane chain, the potentials from reference [84] were used, while for the atoms of the different functional groups, the CHARMM potentials, reference [85], were used.

In addition, the functional groups were built by atoms with partial charges. Therefore, besides the intra-molecular interactions, the charged atoms interacted with its surrounding environment by the electrostatic potential, determined by the particle mesh Ewald algorithm described previously.

The chemical bonds between two consecutive atoms in the head group (sulphur), alkane chain (united-atom carbons) and in the functional groups (an all-atom description) were described by the harmonic potential V_{bond}

$$V_{bond}(r) = \frac{k_{bond}}{2}(r - r_{eq})^2 \quad , \tag{4.9}$$

which depends only on the distance r between the two atoms.

The potential energy of the angle bend between a triplet of atoms V_{angle} was obtained by an harmonic potential

$$V_{angle}(\theta) = \frac{k_{angle}}{2}(\theta - \theta_{eq})^2 \quad , \tag{4.10}$$

where the magnitude of the potential depends only on the angle θ between two consecutive bonds. The force field used to describe the functional groups, CHARMM[85], sometimes requires the introduction of virtual bonds, so to restrain the motions of the bonds involved in the angles. These restrictions are obtained by defining a potential, often named as Urey-Bradley potential, which uses an equation equivalent to the bond potential function, equation 4.9.

Finally, the torsional potential between four consecutive atoms were modelled by two different potentials. For the atoms in the head group and alkane chain, the potential used was the OPLS (optimized potentials for liquid simulations) potential[86] V_{OPLS}

$$\begin{aligned} V_{OPLS}(\phi) &= A_0 + \frac{A_1}{2}\left(1 + \cos(\phi - \phi_0)\right) - \frac{A_2}{2}\left(1 + \cos(2(\phi - \phi_0))\right) \\ &\quad + \frac{A_3}{2}\left(1 + \cos(3(\phi - \phi_0))\right) \quad , \end{aligned} \tag{4.11}$$

while for the atoms in the functional groups, a cosine potential was used V_{cos}

$$V_{cos}(\phi) = A\left[1 + \cos(m\phi - \delta)\right] \quad . \tag{4.12}$$

In these equations, variables $k_{bond}, r_{eq}, k_{angle}, \theta_{eq}$, A_0, A_1, A_2, A_3, ϕ_0, A, m and δ are parameters.

Short range potentials/Remaining potentials

In the simulated systems, intra-molecular and intermolecular interactions need to be taken into account. Until now, the intra-molecular interactions in the alkanethiols were described, as well as the interatomic interations within the gold, within the water, between the gold and the water and between the gold and the sulphur head group.

The remaining interactions that still need to be described are the van der Waals interactions between the several components of the different alkanethiols and the short-range interaction between the components of the alkanethiols and the gold/water. Each of the short-range interactions was described with a Lennard-Jones potential

$$V(r_{ij}) = 4\epsilon_{ij}\left[\left(\frac{\sigma_{ij}}{r_{ij}}\right)^{12} - \left(\frac{\sigma_{ij}}{r_{ij}}\right)^{6}\right] \quad , \tag{4.13}$$

which describes the effect between atom i and j, separated by a distance r_{ij}. ϵ_{ij} is the depth of the potential well and σ_{ij} is the finite distance at which the inter-atomic potential is zero, that is, the hard core radius.

The parameters ϵ_{ij} and σ_{ij} for the same atomic entities were obtained from reference [84], for the case of the head group and the carbons from the alkane chain, and from reference [85], for the atoms of the different functional groups. To describe the short range interactions between different atoms, the parameters ϵ_{ij} and σ_{ij} were obtained from the Lorentz-Berthelot mixing rules

$$\epsilon_{ij} = \sqrt{\epsilon_i \epsilon_j} \quad \text{and} \quad \sigma_{ij} = \frac{\sigma_i + \sigma_j}{2} \quad . \tag{4.14}$$

In order to apply the mixing rules for the particular case of gold interacting with the remaining atoms of the system, it was necessary to determine a Lennard-Jones potential that was equivalent to the interatomic description of the Sutton-Chen potential. The method used to obtain the Lennard-Jones parameters is described in reference [87].

The real space cut off used, for the calculation of the long range force fields was of 12 Å, while the short range potentials were determined up to a distance of 11 Å. The only exceptions were on the heating period of the nanoparticles with diameter of 2, 2.5, 3, 3.5, 4, 5.5 and 7 nm, and the cooling process of the nanoparticles with diameter of 2, 2.5, 3, 3.5, 4 and 5.5 nm, where both cutoffs were set to 7.5 Å.

4.1.2 Initialisation

Once the interactions between each component of the system are established, we can initialise the system. The initialisation process comprises two main steps: obtain the initial configuration of the system, that is, attribute the initial position for each atom in the system, followed by assigning an initial velocity to each particle.

The initial atomic distribution depends on the type of materials or conditions that want to be simulated. In this work, as various systems are simulated, each initial configuration is described in detail further ahead.

As for the initial velocities for each particle, the velocities distribution should reflect the temperature at which we want to simulate the system. In DL_POLY, the attribution of the velocities obeys a Maxwell-Boltzmann distribution for a required temperature.

It is also important to establish the boundary conditions used, that is, if the simulation box is replicated in each direction or not. In the systems simulated, periodic boundary conditions in the three dimensions were used.

4.1.3 Force calculation and integration algorithms

The interactions between the atoms, i.e., the forces acting on each particle are given by the negative derivative with respect to x, y, and z of the interatomic potentials established by the user. For a system with N particles, the force on each particle i will have $N-1$ pairwise additive interactions. If the number of particles in the system is high, which is the case of the simulations performed in this work, then the evaluation of the forces scales rapidly as N^2[67]. Therefore, in most simulations, the force calculation is the most time consuming part of any molecular dynamics program.

To reduce this computational time, a few tricks are put into place. For instance, the forces are only explicitly evaluated within a cutoff distance r_{cut} from the particle, which for the case of systems with periodic boundary conditions, should be smaller than half of the simulation box size. For the case of short range forces, this approximation does not introduce a lot of errors, as the force rapidly reaches zero as the distance increases. When the forces are long range, the real space terms are only calculated up to a distance r_{cut}, as explained in section 4.1.1. Furthermore, the MD program has several lists, which speeds up the access to the atomic information needed to determine the forces. For instance, a link cell list is created, in which the simulation box is divided in smaller cells of size equal or slighly larger than r_{cut} and then each atom i only interacts with atoms from its link cell or the surrounding link cells. Also, from this link cell list, a neighbours lists or Verlet list is used, which keeps track of the particles surrounding each particle up to a cutoff distance r_{cut}.

Once the forces have been calculated, the integration of Newton's equations of motion is done using the velocity Verlet algorithm, which is one of the simplest and usually one of the best in existence[67]. In the velocity Verlet algorithm, the calculation of the new position of atom i after a time Δt is done in two steps. In the first step, the current

position, velocity and force are used to determine the velocity at time $t + \Delta t/2$

$$\vec{v}\left(t + \frac{\Delta t}{2}\right) = \vec{v}\,(t) + \frac{\Delta t}{2m}\vec{f}\,(t) \quad . \tag{4.15}$$

With this new half-step velocity, the particle is moved by a full step $t + \Delta t$,

$$\vec{r}\,(t + \Delta t) = \vec{r}\,(t) + \Delta t \vec{v}\left(t + \frac{\Delta t}{2}\right) \tag{4.16}$$

and as the positions have changed, the recalculation of the forces at time $t + \Delta t$ is also required.

The second step can then happen, as the half-step velocities are advanced to a full step, while using the new force.

$$\vec{v}\,(t + \Delta t) = \vec{v}\left(t + \frac{\Delta t}{2}\right) + \frac{\Delta t}{2m}\vec{f}\,(t + \Delta t) \tag{4.17}$$

In terms of energy conservation, it is basically impossible to have an algorithm that conserves the energy simultaneously at short (that is, a few timesteps) and long times. For instance, the force integration error and the sensitivity to the initial conditions introduce divergencies between the true trajectory of the particles and the computational trajectory. A Verlet-style algorithm has moderate short-term energy conservation but little long-term energy drift. Furthermore, the Verlet algorithm produces almost time-reversible trajectories, which is convenient as Newton's equations of motion are in reality also time reversible.

4.1.4 Ensembles

The system conditions and simulation procedures described so far simulate an ensemble where the number of atoms N, the volume V and the energy E of the system are kept constant. This type of ensemble is known as NVE or microcanonical ensemble.

However, the system may also be coupled to a heat bath to ensure that the system average temperature is kept close to the bath temperature. This ensemble, where the number of atoms N, the volume V and the temperature T of the system are kept constant, is named canonical or NVT ensemble. From the different types of thermostats available, the Nosé-Hoover and the Berendsen were employed in this work. The Nosé-Hoover thermostat, widely employed in MD simulations, is the result of Nosé's use of an extended Lagrangian (i.e., a Lagrangian that contains additional, artificial coordi-

nates and velocities) in Hoover's formulation (where a thermodynamic friction term is included). The equations ruling the system dynamics and further information can be obtained in references [67] and [68]. As for the Berendsen thermostat, the main thermostat used in this work, its description is provided in section 4.2.1.

Furthermore, in systems where it is important to control both the pressure P and temperature of the system, the isobaric and isothermal ensemble or NPT ensembles is used. Hence, besides applying a thermostat to the system, the system is also coupled to a barostat, which can dynamically adjust the size of the simulation box, cell vectors and atomic coordinates. For the case of the Berendsen barostat, the system volume is rescaled, at every time step, by a value η, while the coordinates and cell vectors by a value $\eta^{1/3}$. The variable η is obtained by

$$\eta(t) = 1 - \frac{\beta \Delta t}{\tau_P} \left(P_{ext} - P(t) \right) \quad , \tag{4.18}$$

where β is the isothermal compressibility of liquid water for the water potential used, τ_P is a specific time constant for pressure fluctuations, P_{ext} is the targeted pressure and $P(t)$ is the instantaneous pressure. Further information about this kind of ensemble and barostats can be found in references [67] and [68].

At this stage, all the fundamental knowledge to simulate systems in equilibrium conditions, as constant pressure, temperature, energy, number of particles and/or volume has been summarised. In the next section, two possibilities to set non-equilibrium conditions are described.

4.2 Non-equilibrium molecular dynamics

Up to this point, the MD conditions explained mimic systems in equilibrium, that is, only one thermostat or barostat is applied in the entire system, or there is an even energy distribution throughout the system. Nevertheless, the use of out of equilibrium conditions provides different and challenging ways to investigate diverse systems.

When external conditions are forced in a system initally in equilibrium, its configuration will evolve in order to accommodate these changes. During this period, the system is said to be in a transient state. After some time, if the external conditions are kept constant, the system will reach a new stable configuration. From this stage

onwards, the system is said to be in a steady state.

In this thesis, we wish to investigate heat transfer within our system with non-equilibrium conditions. For this reason, a nonuniform temperature is set throughout the system. After some time under these conditions, the system reaches a steady state regime, with a constant heat flow from the hot to the cold part of the system. At this stage, certain parameters, such as temperature averages and temperature profiles, can be measured.

Two distinct approaches, both commonly used in the literature[58, 88, 89], are considered to set a temperature difference in a system:

1. **Two thermostats method:** control of two temperatures in different parts of the system.

2. **Heat source and sink method:** control of the energy (heat) added and removed from the system.

In the next pages, the basic principles underlying each method are explained. These approaches, although quite similar, have some mathematical variations and produce slightly different outcomes in the simulation of the same system, as explained ahead. For this reason, possible limitations and a comparison between the two methods are also provided. Furthermore, the molecular dynamics code used in this project, DL_POLY_3[68] is not prepared to set and monitor the effects of the non-equilibrium conditions. Therefore, new subroutines are added to the program and their description is presented in appendix A.

4.2.1 Two thermostats method

For this method, let us consider an initial system with a parallelepiped shape, divided into several slabs. The system is initially in equilibrium at temperature T_i. Now, suppose that one of the slabs is heated up to a certain temperature T_{hot}, while a different slab is kept at the initial temperature $T_{cold} = T_i$ (figure 4.2). After some time, the system will reach a steady state regime, where a constant temperature gradient is established between the hot and cold slabs (figure 4.3).

These different temperatures can be achieved by means of independent thermostats in the two slabs. The Berendsen thermostat[90], one of the thermostats currently widely used in computational modelling, is applied to periodically rescale the velocities of the atoms that belong to the target region by a quantity χ, a "rescaling factor".

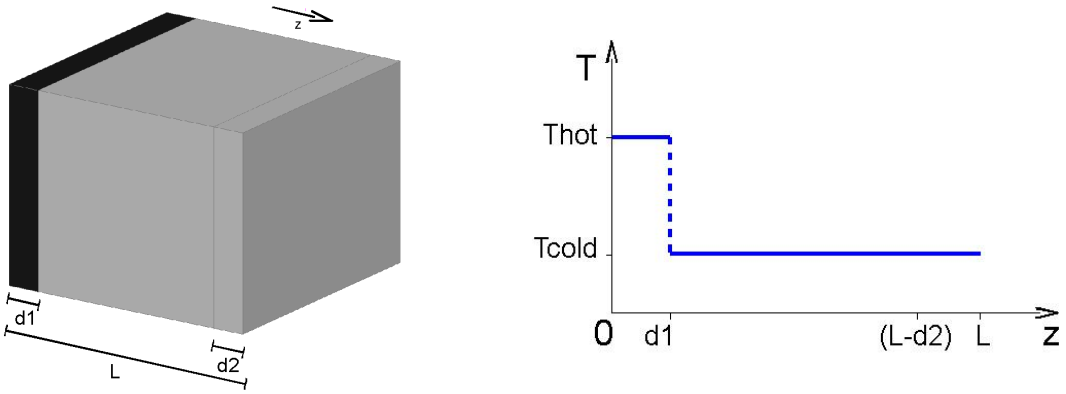

(a) (b)

Figure 4.2: (a) Schematic view and (b) graph of the initial temperature profile of the system once the two thermostats are switched on. In (a), darker grey means a higher temperature than lighter grey.

Mathematically, and with a simple approach, the rescaling factor χ is obtained as follows

$$E_{bath} = E'_K \quad ,$$

$$\tfrac{fN}{2} k_B T_{bath} = \sum_i \tfrac{1}{2} m_i v_i'^2 \quad , \tag{4.19}$$

where E_{bath} is the thermal energy at the target temperature T_{bath}, E'_K is the kinetic energy of the target region (in the example, the target region is the slab), f is the number of degrees of freedom per atom (or molecule), N is the number of particles (or molecules) present in the region, k_B is the Boltzmann's constant, m_i and v'_i are the mass and the new velocity of atom i in the region.

In terms of the simulation, the adjustments of the system properties and variables occur in steps. The new velocity v'_i can be interpreted as a rescaling from the previous velocity of the atom v_i by the factor χ as

$$v'_i = \chi v_i \quad . \tag{4.20}$$

From this equation and from equation 4.19, the value of the rescaling factor can be derived as

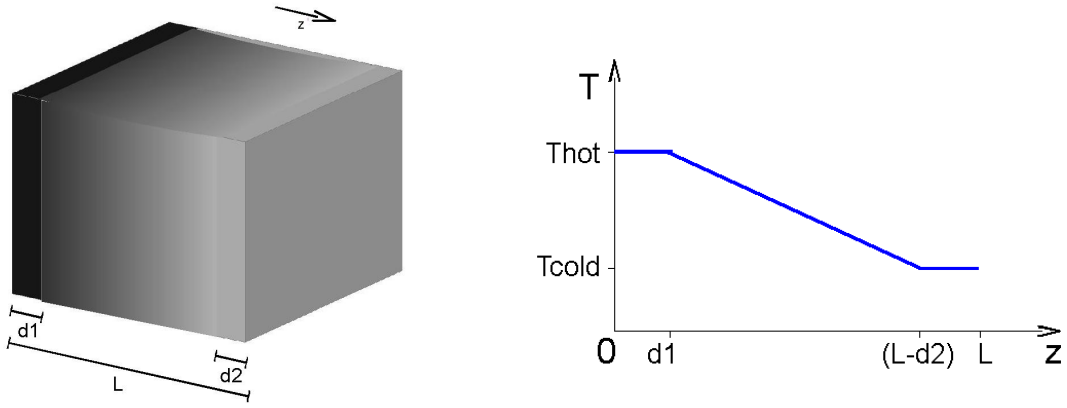

(a) (b)

Figure 4.3: (a) Schematic view and (b) graph of the temperature of the system at steady state. In (a), darker grey means a higher temperature than lighter grey.

$$\chi = \sqrt{\frac{fNk_BT_{bath}}{\sum_i m_i v_i^2}} \quad . \tag{4.21}$$

This computational approach of setting up a thermostat (or a thermal bath) in a region can be optimised to simulate a real situation. In a real system, there is typically a delay between a temperature change and the response of a thermostat to that change. The Berendsen thermostat mimics this behaviour by taking into account a temperature fluctuation time τ. Therefore, the rescaling factor is given by

$$\chi = \sqrt{1 + \frac{\Delta t}{\tau}\left(\frac{fNk_BT_{bath}}{\sum_i m_i v_i^2} - 1\right)} \quad , \tag{4.22}$$

where Δt is the timestep of the simulation.

In summary, for the rescaling of the temperatures in the target region, independent of its shape, the velocities of the atoms are rescaled using equations 4.20 and 4.22.

4.2.2 Heat source and sink method

For the case of the heat source and sink method, let us consider a parallelepiped system divided in several slabs along the z direction, all at an initial temperature T_i. Now, at regular intervals Δt of the simulation, a certain amount of heat $C_+ = +\Delta E$ is added

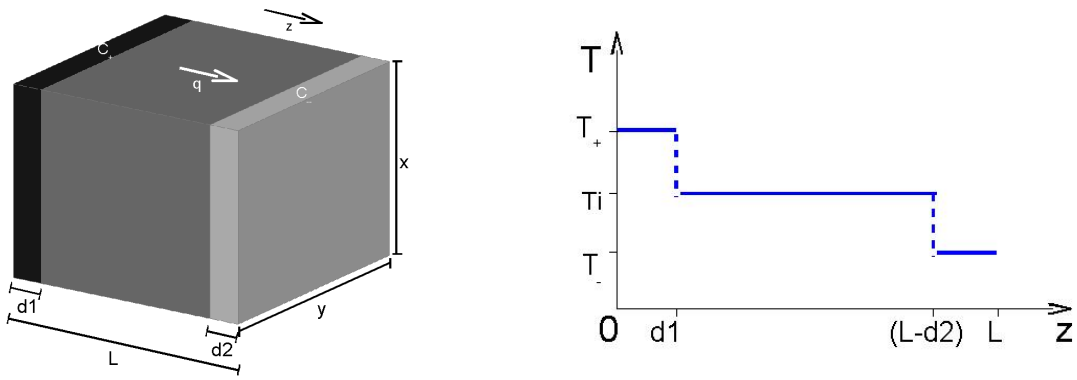

(a) (b)

Figure 4.4: (a) Schematic view and (b) graph of the temperature of the system once the energy source and sink are switched on. In (a), darker grey means a higher temperature than lighter grey.

to one of the slabs and, at a different slab, the same amount of heat $C_- = -\Delta E$ is removed, in order to keep a constant heat flux q_z along the z direction in the system, given by

$$q_z = \frac{\Delta E}{x \cdot y \ \Delta t} \quad , \quad \Delta E = q_z x \cdot y \ \Delta t \quad , \tag{4.23}$$

where $x \cdot y$ is the slab area in the direction perpendicular to the heat flux.

This addition and reduction of heat will impose an increase and decrease of the temperature of the slab to T_+ and T_-, respectively. Figure 4.4 shows a possible initial state of a system with a heat source and sink.

After some time, the system will reach a steady state regime and a stable temperature profile is obtained (figure 4.3). That is, at the heat source slab, a temperature T_{hot} is observed. At the slab functioning as the heat sink of the system, a temperature T_{cold} is registered. And in between these slabs, a temperature gradient is set.

Computationally, rescaling the velocities of the atoms in the heat source (or heat sink slabs) by a quantity α_+ (or α_-) provides a way to add and remove energy from the system. These rescaling variables, mathematically derived below, are then applied to the old velocity of the atoms, v_i (where i is the index of the atom), in order to adjust to a new velocity v_i', as follows

$$v_i' = \alpha v_i \quad , \tag{4.24}$$

where α can be either α_+ or α_-, depending on the slab where the atom is located.

It is worth emphasising that the velocities must be rescaled without introducing a change of the velocity of the centre of mass of the system, i.e., the total momentum of the system must be conserved[89]. So, the velocity v_i of the atom must be separated into the velocity of the centre of mass v_G of the system plus the relative velocity of the atom with respect to the centre of mass v_{rel_i}, meaning

$$v_i = v_G + v_{rel_i} = v_G + (v_i - v_G) \quad . \tag{4.25}$$

By rescaling only the relative velocity of each atom and keeping the velocity of the centre of mass unchanged, the total momentum of the system is conserved. So,

$$v_i' = v_G + \alpha v_{rel_i} = v_G + \alpha\,(v_i - v_G) \quad . \tag{4.26}$$

To deduce the value of the rescaling variable α, the increase (or decrease) in energy of the system is associated to the change in the kinetic energies of the atoms involved, i.e.,

$$\Delta E = E_{Knew} - E_{Kold} = \frac{1}{2}\sum_i m_i \left(v_i'^2 - v_i^2\right) \quad . \tag{4.27}$$

Substituting v_i' from equation 4.26 and v_i from equation 4.25, and using the definition of the centre of mass velocity as $v_G = \frac{\sum_i m_i v_i}{\sum_i m_i}$, the following result is obtained

$$\Delta E = \frac{1}{2}\left(\alpha^2 - 1\right)\left(\sum_i m_i v_i^2 - \sum_i m_i v_G^2\right) = \frac{1}{2}\left(\alpha^2 - 1\right) E_{Krel} \quad . \tag{4.28}$$

To obtain a value for α_+ or α_- (hereafter referred to as $\alpha_\pm$), the previous equation is rewritten in order of α, explicitly stating the adding or removing of energy ΔE, i.e.

$$\alpha_\pm = \sqrt{1 \pm \frac{\Delta E}{\frac{1}{2}\sum_i m_i v_i^2 - \frac{1}{2}\sum_i m_i v_G^2}} \quad . \tag{4.29}$$

In summary, the addition/reduction of energy to/from the system (given by equation 4.28, in order to guarantee a constant flux), is performed by rescaling the velocities of the atoms, according to equation 4.26, with a value $\alpha_\pm$, given by equation 4.29, where '+' and '−' represent adding or removing energy to/from the system, respectively.

As the energy added and removed from the system depends on the geometry of the system, since it depends on the area of contact between the region of the system where the velocities are rescaled and the remainder of the system, this method is only used in the slab systems similar to the example used.

4.2.3 Comparison between the two methods

To evaluate the relative performance of the two thermostats and the source and sink methods, each method is used separately to perform otherwise identical simulations in the slab system of two gold slabs separated by a water layer approximately 35 Å thick. The details of the system setup and relaxation, for both simulations, are provided in section 6.3.1. Regarding the source and sink method, further simulation details are described also in section 6.3.1. As for the two thermostats simulation, the gold slabs were set to 500 K and 300 K, respectively. This system reached steady state in around 70 ps. The steady state was identified according to the conditions described in section 4.3. Once stable, the water temperature slope in graph 4.6(a) and the experimental value of the water thermal conductivity provided in appendix B were used in Fourier's law (equation 2.2) to determine the heat flux of 9.16×10^9 W m^{-2}, from the hot to the cold slab.

It is found that the two thermostats approach is more computationally efficient than the source and sink method: the simulation time needed to reach a steady state regime is around 50 ps faster for the former than for the latter. Another advantage of this method is that it can be used independently of the system configuration, only requiring the identification of the targeted regions.

Another difference between the two methods lies in the configuration energy of the system. As can be verified in figure 4.5, when the two thermostats approach is used, the configuration energy of the system does not reach a constant value, whereas a steady regime is obtained when the source and sink method is used. This difference between the two methods results from the fact that, with the source and sink method, it is assumed that the total energy of the system is constant throughout the simulation, while with the two thermostats method, it is the temperature of the slabs that remains constant.

As for the temperature profiles, shown in figure 4.6, both methods lead to qualitatively similar profiles, but the two thermostats approach presents a slightly smoother profile than the source and sink method. For both methods, the water density varies as

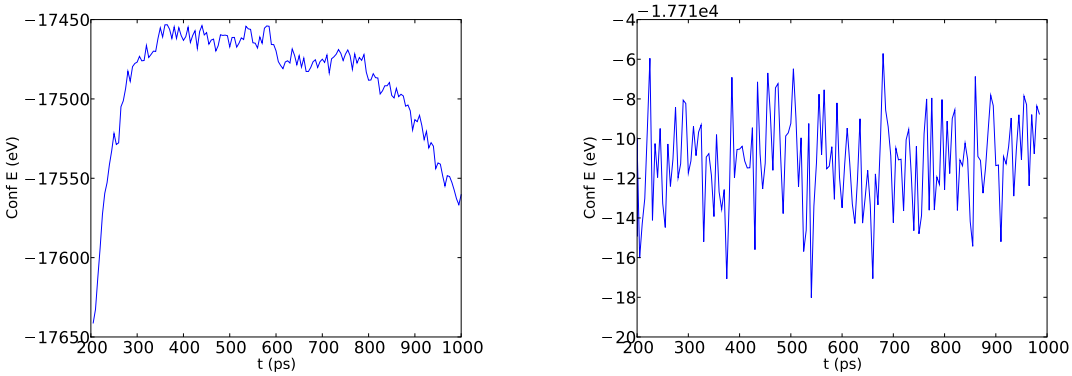

(a) (b)

Figure 4.5: Configuration energy for the system of two gold slabs separated by a water slab of 35 Å thick when (a) the two thermostats and (b) the source and sink method are used.

it approaches the interface. A first layer of water adsorbs to the surface, followed by a lower density region. This creates a region with high water density, followed by a slab with lower density.

In conclusion, both methods have their advantages and flaws. While the two thermostats method does not maintain a constant energy flow in the system, the source and sink method takes longer to reach steady state. It is worth emphasising that these conclusions are only valid for the system simulated (a water slab between two gold slabs) and for the simulation time tested (maximum of 1 ns). Hence, for the reasons presented above, it was decided to use the heat source and sink method for all the slab systems tested, as it was not fundamental to reach pre-defined temperatures and the conservation of the energy in the system is an important aspect to take into account. On the other hand, for the spherical systems, the two thermostats method was applied, since the gold nanoparticles and the water should be set to specific temperatures, allowing an easier comparison with the realistic cases of the use of gold nanoparticles as heat sources for cancer therapy, and the configuration energy losses are still small ($< 1\%$) for the simulation times used.

As mentioned in the beginning of this section, the systems under non-equilibrium conditions are evaluated when steady state regime is reached. The method used to evaluate such regime is explained in the next section.

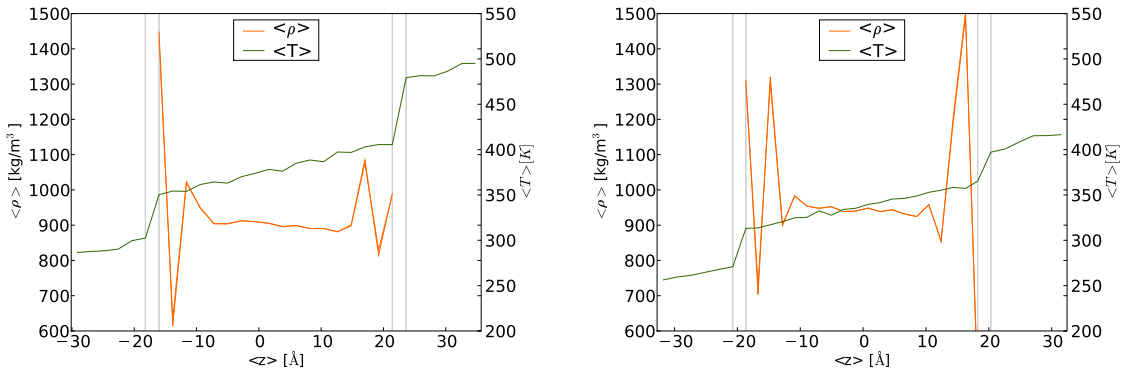

Figure 4.6: Average density and temperature distribution for a system with 35 Å thick water slab, after steady state conditions are reached, when (a) the two thermostats and (b) the source and sink methods are used. Each of the averages contains around 300 to 400 ps of data collection. The vertical grey lines mark, from left to right, the end of the gold slab, the beginning and the end of the water slab, and the beginning of the gold slab.

4.3 Determination of the steady state regime

The computational work related with the biomedical applications, namely in chapters 6, 7 and 8, was done considering the behaviour of the systems under non-equilibrium conditions. The data analysis was performed once the systems reached a steady state regime. The determination of the system's steady state was based on the temperature variation in specific regions of the system. If the heat source and sink method was used, then the temperature profile of the gold slabs was monitored with time. On the other hand, if the two thermostats method was used, then the temperature of the non-thermostated water was checked.

Irrespective of the non-equilibrium MD method employed, the evaluation of the transition from a transient to a steady state regime started by determining the rolling average temperature $T_{rol}(t)$ of the monitored region, with a Δt_{rol} time interval (example in figure 4.7(a)). Depending on the sampling frequency used to collect statistics, the value of Δt_{rol} was adjusted to include at least ten temperature values. With these values of $T_{rol}(t)$, the temperature difference between the rolling average temperature at time t and at time $t + 20$ ps was determined, that is, $\Delta T(t) = T_{rol}(t + 20) - T_{rol}(t)$ (example in figure 4.7(b)). The average temperature $\overline{T}$ and standard deviation σ were also

calculated from the last $100 - 300$ ps of simulation[1] , where the system was considered to be at steady state. Once these values were determined, the following conditions were used to evaluate the stability of the temperature values at a certain time t:

- If $\Delta T(t) < \delta T$, where δT was either 5 K or 1 K, depending if the method employed was the heat source and sink or the two thermostats, respectively;
- And $\Delta T(t + 5 \text{ ps}) < \delta T$;
- And $\Delta T(t + 10 \text{ ps}) < \delta T$;
- And $\Delta T(t + 15 \text{ ps}) < \delta T$;
- And $(\overline{T} - 2\sigma < T_{rol}(t) < \overline{T} + 2\sigma \quad \text{or} \quad \overline{T} - \delta T < T_{rol}(t) < \overline{T} + \delta T)$.

When the majority of the temperatures $\Delta T(t)$ obeyed these conditions, the system was considered to have reached a steady state regime.

[1]This variation of the simulation time comes from the fact that some simulations collected statistics with a lower frequency than others, therefore requiring longer periods of time to determine the value of $\overline{T}$ and σ.

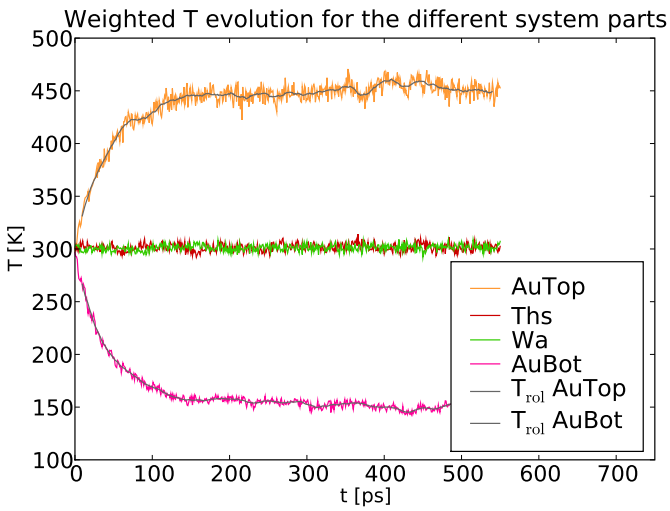

(a)

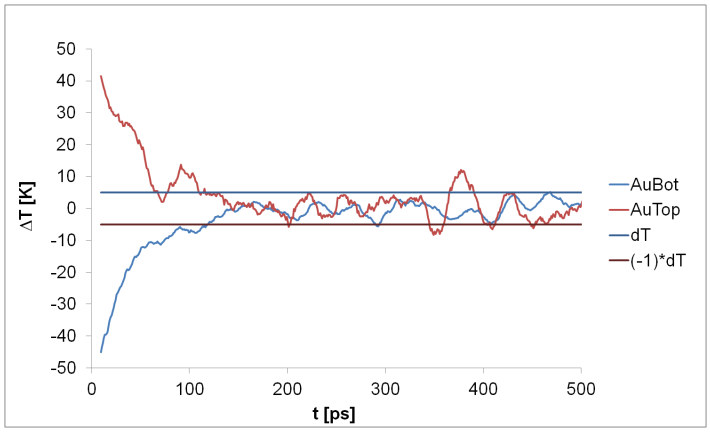

(b)

Figure 4.7: (a) Weighted mean temperatures of the different parts of the system and the rolling average temperatures for the top and bottom gold slabs. These rolling average temperatures $T_{rol}(t)$ were obtained with a time interval of $\Delta t_{rol} = 20$ ps. Using the values of $T_{rol}(t)$ within the interval 439.5-539.5 ps, the average temperature $\overline{T}$ and standard deviation σ were calculated for the top ($\overline{T} = 452.6$ K and $\sigma = 3.3$ K) and bottom gold slab ($\overline{T} = 152.1$ K and $\sigma = 2.8$ K). (b) Temperature difference between the rolling average temperature at time t and time $t + 20$ ps, that is, $\Delta T(t) = T_{rol}(t + 20) - T_{rol}(t)$, for the top and bottom gold slab. These results refer to the slab system of two gold slabs, coated with mercaptohexadecathiol acids, separated by a water layer of 3840 water molecules, when the heat source and sink method is applied. More details on the system and simulation conditions can be found in section 7.1.

4.4 Determination of the heat transfer coefficient - planar system

As discussed in chapters 6 and 7, it will be necessary to evaluate the amount of heat propagated through an interface between two materials. The parameter used to quantify such transfer rate is the heat transfer coefficient, H. One of the possible approaches to determine the value of the heat transfer coefficient for a gold-water interface (either of bare or organic-coated gold) is to study the system of a slab of water between two independent gold slabs.

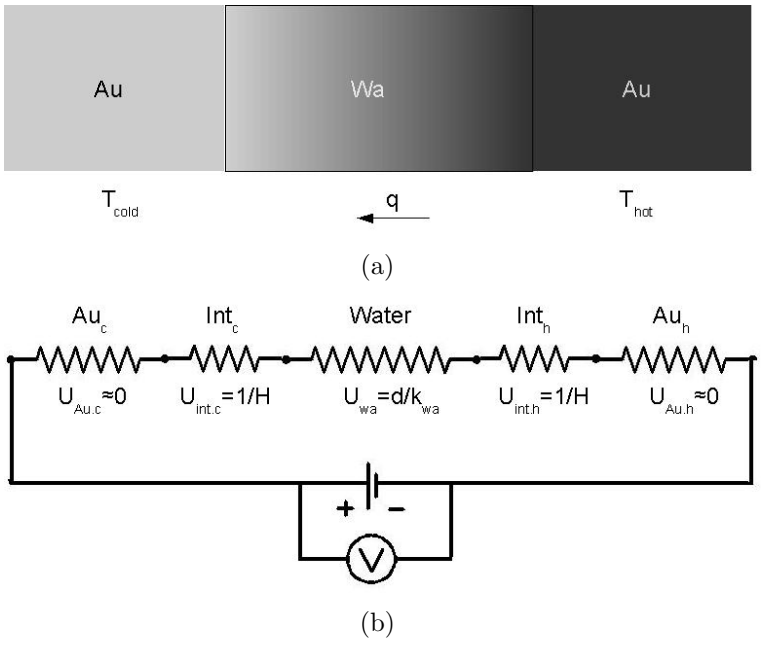

Figure 4.8: Schematic view of the slab system gold-water-gold (a) when the non-equilibrium thermal system reaches steady state conditions and (b) the analogous electrical circuit. See text for the definition of the variables in the schemes.

The system of two slabs of gold, each with a thickness a and thermal conductivity k_{Au}, separated by a box of water of thickness d and thermal conductivity k_{Wa}, as illustrated schematically in figure 4.8(a), can be compared to a system of resistances in series, as shown in figure 4.8(b). With this analogy, the system can be mathematically described using relations analogous to Ohm's Law, that is

$$\Delta V = R\ I \quad \Leftrightarrow \quad \Delta T = U\ q \quad , \tag{4.30}$$

where ΔV is the voltage, I is the intensity of current and R is the resistance. The variable U is the "thermal resistance" the heat flux q faces when progressing between two points with a temperature difference of ΔT.

For the case shown in figure 4.8(b), this "thermal resistance" U can be translated into a group of resistances in series as

$$U = U_{Au.h} + U_{Int.h} + U_{Wa} + U_{Int.c} + U_{Au.c} \quad , \tag{4.31}$$

that is, the sum of the thermal resistance imposed by the water U_{Wa}, gold $U_{Au.h}$ and $U_{Au.c}$, and interface of these two materials $U_{Int.h}$ and $U_{Int.c}$.

Similarly to what is done ahead in sections 6.2.1 and 6.2.2, each of these thermal resistances can be obtained by solving the Fourier-Biot equation (equation 2.5) for a slab system, as the one presented here. Therefore, the thermal resistance within the water can be quantified as

$$U_{Wa} = \frac{\Delta T}{q} = \frac{d}{k_{Wa}} \quad , \tag{4.32}$$

while the thermal resistance within the gold is

$$U_{Au.h} = U_{Au.c} = \frac{\Delta T}{q} = \frac{a}{k_{Au}} \tag{4.33}$$

and the resistance due to the interface is

$$U_{Int.h} = U_{Int.c} = \frac{\Delta T}{q} = \frac{1}{H} \quad . \tag{4.34}$$

Using these three equations in equation 4.31, we obtain

$$U = \tfrac{a}{k_{Au}} + \tfrac{1}{H} + \tfrac{d}{k_{Wa}} + \tfrac{1}{H} + \tfrac{a}{k_{Au}} \quad . \tag{4.35}$$

As can be noted from this equation, if the thickness a of the gold slabs is known, the value of H can be determined if the value of the "thermal resistance" is extrapolated to $d = 0$.

More concretely, if the thickness d of the water box varies for otherwise similar slab

systems and these are simulated until steady state is reached, then the values of ΔT and q, obtained from the simulations statistics, can be used in

$$\frac{\Delta T}{q} = \frac{2a}{k_{Au}} + \frac{2}{H} + \frac{1}{k_{Wa}}d \tag{4.36}$$

and the value of H can be estimated through the fitting parameters obtained by linear regression.

Although not shown in this thesis, these equations can be simplified without inducing a considerable change in the value of the heat transfer coefficient. As the thermal conductivity of gold is much higher than the thermal conductivity of water, the thermal resistance in the gold is assumed to be negligible, i.e. equation 4.35 can be approximated to

$$U = \frac{2}{H} + \frac{1}{k_{Wa}}d \tag{4.37}$$

and equation 4.36 can be simplified to

$$\frac{\Delta T}{q} = \frac{2}{H} + \frac{1}{k_{Wa}}d \quad . \tag{4.38}$$

In this thesis, spherical systems are also simulated and it is also required to evaluate the amount of heat propagated through a curved surface. For this reason, in the next section, the method used to evaluate the value of the heat transfer coefficient for spherical systems is described.

4.5 Determination of the heat transfer coefficient - spherical system

The spherical systems studied in chapter 8 model the temperature evolution of initially hot gold nanoparticles embedded in cold water. Although an approximation, it is possible to estimate the value of the heat transfer coefficient H for a curved bare gold-

water interface.

In the systems tested, each nanoparticle is assumed to be approximately spherical. Therefore, in spherical coordinates, the temperature variation is non-zero on the radial component.

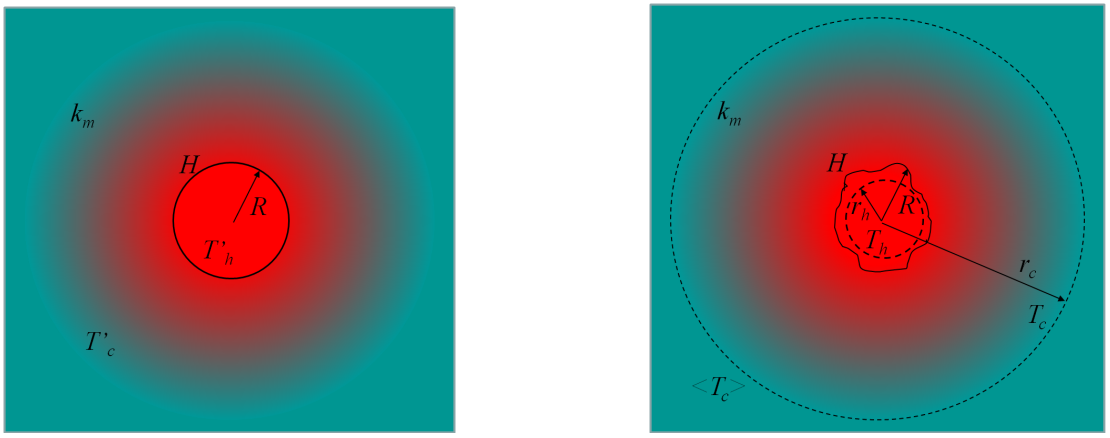

(a) (b)

Figure 4.9: The system of (a) a perfectly spherical nanoparticle and of (b) a more realistic nanoparticle embedded in water, at steady state, under the two thermostats method. In the perfect system, a constant temperature T'_h in the whole nanoparticle and a constant temperature T'_c for the very far away is imposed by the two thermostats. For the realistic system, on average, the nanoparticle is coupled to a thermostat at temperature $< T_h >$ and the water beyond radius r_c is set to a temperature $< T_c >$. Temperatures $< T_h >$ and $< T_c >$ match, respectively, temperatures T'_h and T'_c of the perfect system.

Let us consider a perfect system, as the one described in section 6.2.1, where a spherical particle of radius R and constant temperature T'_h is embedded in water with a constant thermal conductivity k_{Wa}. At steady state, figure 4.9(a), the system presents a temperature profile, where very far away from the particle the temperature is T'_c. Using a method similar to the one previously demonstrated for a slab system (section 4.4), the temperature difference ΔT is proportional to the heat flow Q by

$$\Delta T = U\ Q \quad , \text{with} \quad U = U_i + U_{Wa} \quad , \tag{4.39}$$

where U is the "thermal resistance", due to the gold-water interface U_i and due to the conduction in the water U_{Wa}.

When the heat transfer is limited by the gold-water interface, and as explained later in section 6.2.2, equation 4.39 reduces to

$$U_i = \frac{\Delta T}{Q} = \frac{1}{4\pi H R^2} \quad . \tag{4.40}$$

When the heat transfer is limited by the thermal conduction in the water, it is shown later in section 6.2.1 that equation 4.39 reduces to

$$U_{Wa} = \frac{\Delta T}{Q} = \frac{1}{4\pi k_{Wa} R} \quad . \tag{4.41}$$

Therefore, for a perfect gold sphere embedded in an infinite medium and where the heat transfer through the gold-water interface and through the water are comparable, equation 4.39 becomes

$$\frac{\Delta T}{Q} = \frac{T_h' - T_c'}{Q} = \frac{1}{4\pi H R^2} + \frac{1}{4\pi k_{Wa} R} \quad . \tag{4.42}$$

Unfortunately, the simulated systems (figure 4.9(b)) have constraints/limitations that need to be taken into account. For instance, each nanoparticle is not a perfect sphere, that is, at certain radii, both water molecules and gold atoms are present. Also, due to the limitations of the simulated systems, it is impossible to simulate an infinite medium. Therefore, the simulated system has a size constraint. Beyond a distance r_c from the nanoparticle centre and until the limits of the simulation box, the water is thermostated to a temperature $< T_c >$, while the gold atoms are thermostated to a temperature $< T_h >$, meaning that the temperature distribution within the thermostated regions is not equal to a constant value, but instead has an average value of $< T_c >$ and $< T_h >$, respectively. Finally, although the average temperatures of the thermostated regions $< T_h >$ and $< T_c >$ agree with T_h' and T_c' of the perfect system, if equation 4.42 is applied to specific radii r_c and r_h (where only gold atoms are present), the temperatures are locally T_c and T_h, respectively (see figure 4.9(b)). Therefore, equation 4.42 re-written for a finite system becomes

$$\frac{\Delta T}{Q} = \frac{T_h - T_c}{Q} = \frac{1}{4\pi H r_h^2} + \frac{r_c - r_h}{4\pi k_{Wa} r_h r_c} \tag{4.43}$$

for the simulated systems, where the value of the heat flow Q can be determined by fitting equation

$$T(r) = T_c - \frac{Q}{4\pi k_{Wa} r_c} + \frac{Q}{4\pi k_{Wa}} \frac{1}{r} \tag{4.44}$$

to the temperature profile of the non-thermostated water.

Knowing the value of heat flow Q, and choosing the first corona of thermostated water at radius r_c at temperature T_c and the last corona with only gold atoms at radius r_h at temperature T_h, equation 4.43 can be rearranged and used to obtain the heat transfer coefficient H by

$$H = \left(4\pi r_h^2 \frac{\Delta T}{Q} + \frac{r_h \left(r_h - r_c \right)}{k_{Wa} r_c} \right)^{-1} \quad . \tag{4.45}$$

4.6 Verification of nanoparticle melting

As described in chapter 5.1, the nanoparticles used in the simulations are produced by initially creating a perfect crystalline particle, and then by simulating the annealing process. While performing the annealing of the gold nanoparticle, it is necessary to verify that the entire nanoparticle is melted before starting the cooling process. For that, two methods are used:

- **Radial Distribution Functions (RDF):** The RDF represents the probability of finding particles at a distance r of a reference particle. For a crystal, where long range order is anticipated, the RDF will have several well defined peaks. For a liquid, which is known to present only local order (mostly within their first neighbours), the RDF should present two broad peaks.

- **Diffusion coefficient:** for solids the diffusion coefficient is $<< 10^{-9}$ m^{2}s^{-1}, while for liquids the diffusion coefficient is of the order of or greater than 10^{-9} m^{2}s^{-1}.

4.7 Analysis of crystal lattice defects

Due to the annealing conditions used (chapter 5), the gold nanostructures are subjected to changes in their crystal structure. These changes are identified by calculating an order parameter that quantifies the local structural order near each atom. The calculation of this order parameter for each atom follows the description by Morris[91]. For this equation, N_q wave vectors $\mathbf{q}$ are established so that the definition of the reciprocal

lattice in a perfect crystal lattice is respected[92] for any vector $\mathbf{r}$ connecting an atom to its nearest neighbours Z, i.e.,

$$e^{i\mathbf{q}\cdot\mathbf{r}} = 1 \quad . \tag{4.46}$$

Taking this into account, the order parameter ψ is then defined as

$$\psi = \left| \frac{1}{N_q} \frac{1}{Z} \sum_{\mathbf{r}} \sum_{\mathbf{q}} e^{i\mathbf{q}\cdot\mathbf{r}} \right|^2 \quad , \tag{4.47}$$

where the number of neighbours Z are found within a distance r_a of the atom, chosen to be between the first- and second-neighbours shells in a perfect lattice. The sum over $\mathbf{r}$ runs over each of the Z neighbours, while the sum over $\mathbf{q}$ runs over each of the N_q wave vectors.

This quantity ψ may have different meanings, depending on the set of reciprocal lattice vectors used. If, for each atom, the reciprocal lattice vectors are determined from a set of three first neighbours, then the determination of the variable ψ gives the local order of that atom in its environment. In this case, ψ can be referred to as a *local order parameter*. On the other hand, if a single set of reciprocal lattice vectors is used to evaluate the quantity ψ for each atom, then ψ measures the relative orientation of the crystal planes of the nanostructure with respect to the chosen set of reciprocal lattice vectors. In this case, ψ can be referred to as a *relative order parameter*. Therefore, if the first option is used, then the values of ψ evaluate the order in the nanostructure, while if the second approach is chosen, the result achieved is equivalent to the one obtained experimentally, for instance, by X-ray diffraction.

To evaluate either the relative or local order parameter for each atom in a nanostructure, a C++ program was developed. In this program, the primitive vectors $\vec{a_1}$, $\vec{a_2}$ and $\vec{a_3}$ are determined by considering the unit cell that encloses the atom. The set of primitive vectors is determined by obtaining the vectors between the central atom and three of its surrounding nearest neighbours, which are within a distance r_a of each other and of the central atom. For the case of the local order parameter, this is done for each atom of the nanostructure, while for the relative order parameter method this is only done for the atom with coordinates closest to (0, 0, 0). Once the primitive vectors are determined, the reciprocal lattice vectors of $\vec{b_1}$, $\vec{b_2}$ and $\vec{b_3}$ are calculated

$$\vec{b_1} = 2\pi \frac{\vec{a_2} \times \vec{a_3}}{\vec{a_1} \cdot (\vec{a_2} \times \vec{a_3})} \ , \qquad \vec{b_2} = 2\pi \frac{\vec{a_3} \times \vec{a_1}}{\vec{a_1} \cdot (\vec{a_2} \times \vec{a_3})}$$
$$\text{and} \qquad \vec{b_3} = 2\pi \frac{\vec{a_1} \times \vec{a_2}}{\vec{a_1} \cdot (\vec{a_2} \times \vec{a_3})} \ , \tag{4.48}$$

where together with $(\vec{b_1} + \vec{b_2})$, $(\vec{b_2} + \vec{b_3})$ and $(\vec{b_3} + \vec{b_1})$, these reciprocal lattice vectors form the set of the wave vector $\mathbf{q}$. Once the groups of reciprocal lattice vectors are determined, the vectors connecting each atom to its first neighbours, i.e., the set of vectors $\mathbf{r}$, are obtained. With these two groups of vectors, it is then possible to determine the local order parameter given by equation 4.47, where values close to 1 identify a structure approaching a perfect crystal, while closer to zero are of an amorphous structure.

By associating ranges of the value of ψ with a certain colour and size of an atom, as shown in figure 4.10, it is possible to colour code each atom of the system according to its ψ value[2]. Using this, a colour mapping of the crystal order of the nanostructure can be obtained.

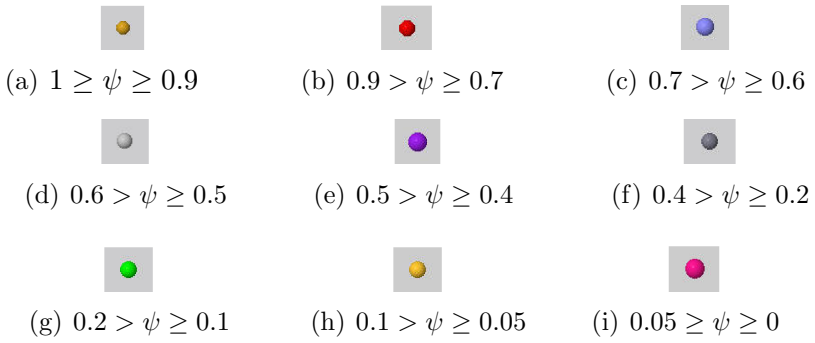

(a) $1 \geq \psi \geq 0.9$ (b) $0.9 > \psi \geq 0.7$ (c) $0.7 > \psi \geq 0.6$

(d) $0.6 > \psi \geq 0.5$ (e) $0.5 > \psi \geq 0.4$ (f) $0.4 > \psi \geq 0.2$

(g) $0.2 > \psi \geq 0.1$ (h) $0.1 > \psi \geq 0.05$ (i) $0.05 \geq \psi \geq 0$

Figure 4.10: Colour scheme, obtained with the visualisation tool Jmol[93], attributed to the range of values of ψ. Values closer to 1 correspond to a crystal, while closer to zero correspond to an amorphous structure.

[2]This colour scheme is only valid when the visualisation program Jmol[93] is used. In some cases, the visualisation tool VMD[94] is used instead and the colour scheme no longer applies.

4.7.1 Order parameter performance

The reliability of the order parameter used was evaluated as follows. Several defects were separately created in an otherwise perfectly crystalline cube with 2048 gold atoms: 5, 10 and 100 vacancies, a twin boundary and a stacking fault. Each system was subsequently relaxed for 10 ps, in NVT conditions, at 10 K temperature. The location of defects is then compared as indicated by the order parameter evaluation. As an example, the results obtained for the stacking fault and for the twin boundary are shown here, while the analysis for the other defects is shown in appendix C.

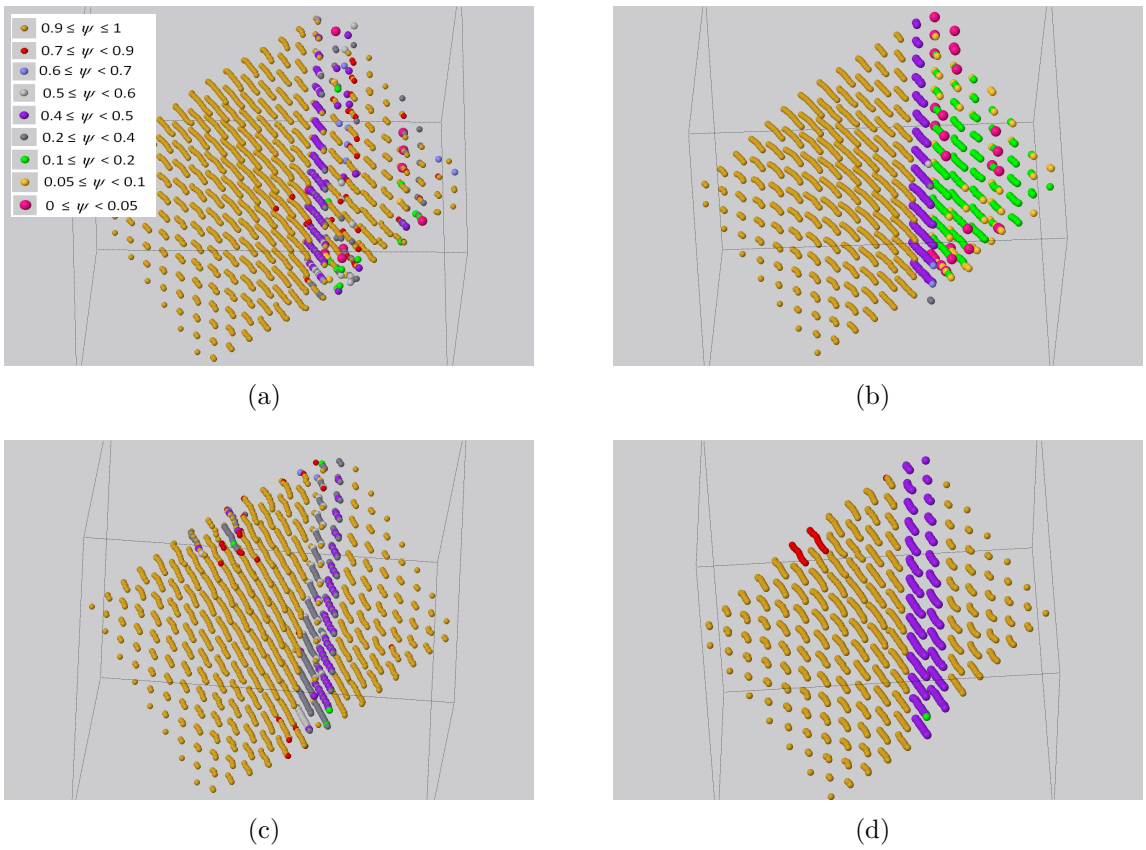

Figure 4.11: Order parameter colour scheme for two created defects. The top two figures are of a twin boundary defect analysed with (a) the local order parameter and (b) the relative order parameter program. The bottom figures are of a stacking fault analysed with (c) the local order parameter and (d) the relative order parameter program.

As can be seen from figure 4.11, the visualisation of the twin boundary and the stacking fault is slightly different, depending on the method used. For the local order

parameter approach, the twin boundary is identified by a layer of atoms with lower ψ, separating two regions of atoms with high order (i .e., high value of ψ), while a stacking fault is recognisable by two layers of atoms with lower ψ separating two regions with high ψ value. As for the relative order parameter method, the stacking fault presents a similar colour scheme to the local order parameter, while the twin boundary is identified by a plane of atoms with lower ψ separating two regions of atoms with different order parameters (i.e., two regions with different colours).

In terms of detection of vacancies in the system, results presented in appendix C, there is no significant difference between the two evaluation methods. Neither of the methods allows the identification of vacancies, independently of their number.

In conclusion, the local order parameter provides a better description for the order of the system and identifies the planar defects present in the nanostructures. For this reason, the local order parameter is chosen to evaluate the nanostructures created.

Chapter 5

Production of nanoparticles and analysis of defects

One of the main systems studied in this thesis comprises gold nanoparticles embedded in water. This system is studied by means of molecular dynamics (MD) simulations. In order to perform any simulations with nanoparticles, it is necessary to first create models of nanoparticles similar to the ones used experimentally, so that the simulations give insight into the systems investigated in experiment.

The simulation methods used to create the nanoparticles mimic the annealing processes employed experimentally[21, 95] and referred in section 3.1. However, due to limitations on the computational time, faster cooling rates are used.

During the production of the nanoparticles, the minimum cooling rate and time needed to allow crystallisation are identified, although these values are expected to change with the size of the nanoparticle. In addition, the importance of the cooling rate on the nanoparticle structure is also demonstrated. Once the nanoparticles are created, their crystal structure is evaluated and the detected defects are compared with imperfections identified experimentally.

In this chapter, the annealing process of the nanoparticles is described, including the verification of the melting of the nanoparticle core (before starting the cooling process), and remarks regarding the cooling rate are also presented. Following this, the defects present in each of the nanoparticles are evaluated with the order parameter method, described in section 4.7.

5.1 Annealing of nanoparticles

For the smaller nanoparticles, the simulation of the annealing process was performed by heating gold nanoparticles created from a perfect face centered cubic (FCC) cube. The fast heating process was terminated when the particle melted and the cooling process was started, at a slower rate. If the cooling rate was slow enough, atoms could reorganise and give rise to crystal structures. On the other hand, if the cooling rate was too fast, it quenched the structure into an amorphous configuration.

Due to limitations on the simulation time, the biggest nanoparticle was obtained through a different process. For this case, a gold sphere was cut from a bigger FCC cube and it was submitted to the cooling process, which started from a temperature lower than the melting point, to allow surface rearrangement.

5.1.1 Systems simulated and conditions used

Independently of the nanoparticle size, the heating and cooling processes were performed in the NVT ensemble using a Nosé-Hoover thermostat, briefly described in section 4.1.4, with a relaxation time of 0.1 ps, and a simulation time step of 1 fs. The interactions between gold atoms were described by the Sutton-Chen potential, described in section 4.1.1. The remaining simulation criteria used: the number of atoms N, the initial temperature of the system being annealed T_i, the temperature the system reaches before the cooling process starts T_h, the final temperature of the system T_f (after the cooling process), the heating s_h and cooling rates s_c (where the temperature step per simulation length, as well as the temperature variation per picosecond are given) are summarised in table 5.1.

It has been observed experimentally and computationally that larger nanoparticles (above $10^3 - 10^4$ atoms) can suffer surface melting, leading to surface change, at temperatures below the melting temperature[3]. Therefore, while performing the annealing of the gold nanoparticles, it was verified that the entire nanoparticle was melted before starting the cooling process by employing the methods described in section 4.6.

Table 5.1: Conditions and results obtained from the annealing of nanoparticles with different number of atoms. The experimental melting temperature T_{me} is obtained from reference [96].

N	T_i [K]	T_h [K]	T_f [K]	s_h [K/ps]	s_c [K/ps]	$\langle OP \rangle_{10K}$	ϕ [nm]	T_{mc} [K]	T_{me} [K]
256	200	800	300	100K/100ps	10K/100ps (0.1K/ps)	0.602	≈ 2	≈ 600	-
500	200	800	300	100K/100ps	10K/100ps (0.1K/ps)	0.816	≈ 2.5	≈ 600	≈ 600
864	200	800	300	100K/100ps	10K/100ps (0.1K/ps)	0.836	≈ 3	≈ 700	≈ 800
1372	200	800	300	100K/100ps	10K/100ps (0.1K/ps)	0.917	≈ 3.5	700-800	≈ 900
2048	300	800	300	100K/100ps	100K/100ps (1K/ps)	0.606	≈ 4	≈ 800	≈ 1000
					50K/100ps (0.5K/ps)	0.639			
					20K/100ps (0.2K/ps)	0.746			
		900	200	100K/100ps	100K/100ps (1K/ps)	0.655			
					50K/100ps (0.5K/ps)	0.743			
					20K/100ps (0.2K/ps)	0.832			
					10K/100ps (0.1K/ps)	0.855			
					5K/100ps (0.05K/ps)	0.839			
5324	200	1000	200	100K/10ps	20K/10ps (2K/ps)	0.402	≈ 5.5	≈ 900	≈ 1100
					20K/50ps (0.4K/ps)	0.750			
10976	200	1000	300	100K/10ps	10K/100ps (0.1K/ps)	0.849	≈ 7	900-1000	≈ 1150
32000	200	1400	300	100K/20ps	20K/100ps (0.2K/ps)	0.7137	≈ 10	≈ 1200	≈ 1230
					10K/100ps (0.1K/ps)	0.680			
84895	-	900	300	-	10K/10ps (1K/ps)	0.950	≈ 14	N/A	≈ 1250

5.2 Computational results for the annealing process

Gold nanoparticles, when compared with other materials such as silver and copper, exhibit a strong dependence of the melting temperature with the nanoparticle size[96, 97]. This dependence is stronger for nanoparticles with diameters smaller than 5 nm. For particles with diameter larger than 10 nm, experiments show that the melting point occurs at temperatures similar to those of bulk gold (1337 K).

The last four columns in table 5.1 present results related with the production of the nanoparticles. The first column contains the value of $\langle OP \rangle_{10K}$, an average value of the local order parameter previously desribed in section 4.7. This averaged value is a quantitative measure of the long range order of the created nanoparticle at temperature T_f, after being allowed to relax for 10 ps at 10 K. The next column is the diameter ϕ of the simulated nanoparticles, estimated by taking into account the number of atoms in the particle N and the volume per atom in an FCC (face-centered cubic) unit cell $V_{cell/at}$, that is,

$$\phi = 2\sqrt[3]{\frac{3}{4\pi} N V_{cell/at}} \ . \tag{5.1}$$

The last two columns present the melting temperatures of the particles. The computational melting temperature T_{mc} is estimated using the two methods described in section 4.6 and based on the data shown in the graphs and snapshots present in appendix D. The value of the experimental melting temperature T_{me} is obtained from reference [96]. In general, all computational values are below the experimental values. The only exceptions are for the smaller particle with approximately 2.5 nm diameter and the bigger particle with approximately 10 nm diameter, where both temperatures present similar values.

In the rest of this section we present conclusions regarding the nanoparticle core melt, estimates of the minimum cooling rate for crystallisation of the particles and comments on the variation of the crystal structure with the cooling rate used.

5.2.1 Verification of the melting of the particle core

As pointed out, two methods (described in section 4.6) are used to determine the melting of the nanoparticles. To reinforce these statements, two extra approaches are used in two of the nanoparticles created, to verify that the core of the nanoparticles reaches a melted stage before the start of the cooling process:

- **Method 1 - Core particle RDF** *vs* **Entire particle RDF:** after removing approximately 75 % of the outer atoms, the RDF is again determined. This RDF can then be compared with the RDF for the entire particle.

- **Method 2 - Differentiation of central atoms:** in the entire nanoparticle, a central plane of atoms is marked (in this case, by changing the colour of the atoms in the visualisation tool), before starting the melting process. At the end of the heating process, the particle can be divided at the position of the previously marked plane and, visually, one can check whether the atoms that were initially in that plane remain there (melting has not occurred) or if they have moved out of the plane and the particle core has melted.

In figure 5.1, the results of these two approaches are displayed. For the first method, results are presented for the particle with approximately 4 nm diameter (2048 atoms), while for the second method the particle with approximately 5.5 nm in diameter (5324 atoms) is used. As can be verified in figure 5.1(a), for the approach of core particle RDF *vs* entire particle RDF, the two curves are very similar in shape, as for example, there is no evidence of the second and third neighbours.

As for the second approach, figure 5.1(b) shows the plane of marked atoms at the beginning of the simulations. At the end of the heating process, as can be verified in figure 5.1(c), the atoms that were initially at coordinate $z = 0$ diffused, leading to the conclusion that the core of the particle is completely melted at 1000 K.

5.2.2 Estimate of the minimum cooling rate for crystallisation

When liquid gold is cooled down, its internal structure rearranges and its final state can be amorphous or crystalline. Its final structure depends, among other aspects, on the cooling rate used. Slow cooling rates allow for atomic restructuring that gives rise to ordered planes of atoms, while faster rates leave more imperfections in the structure, tending to a more amorphous final state.

In this section, the minimum cooling rate s_c and cooling time t_c needed to obtain a crystallised nanoparticle is determined with the particles of approximately 5.5 and 4 nm diameter.

For the first nanoparticle, with diameter approximately 5.5 nm, two cooling rates were used to cool down the nanoparticle from 1000 K to 200 K. The first rate decreased the temperature of the system by 20 K every 10 ps of simulation time, equivalent to a

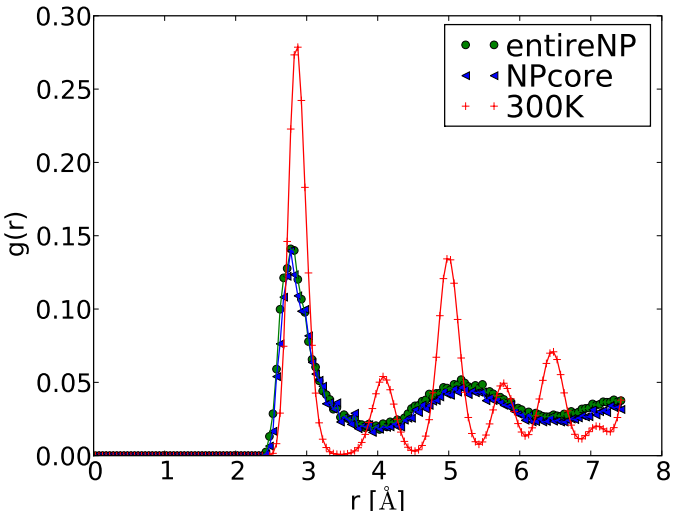

(a)

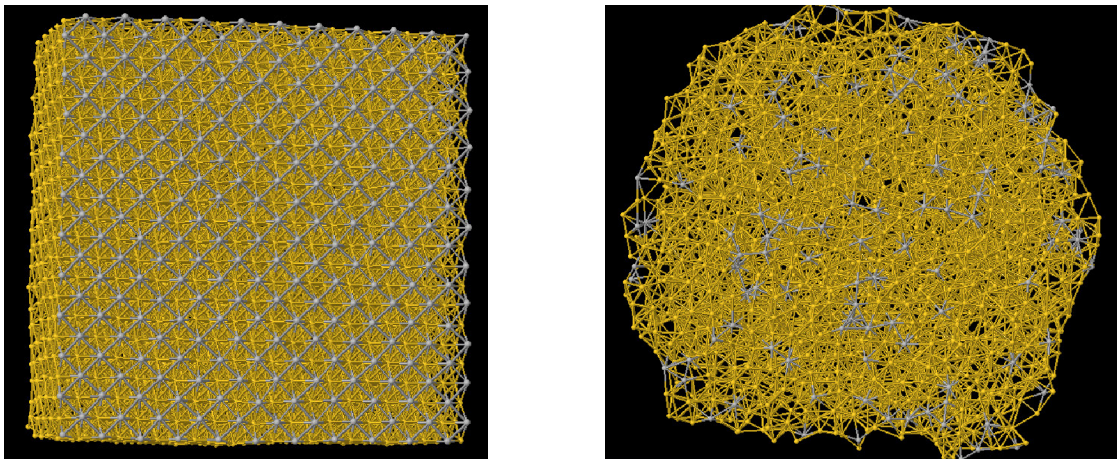

(b) (c)

Figure 5.1: Results regarding the verification of the melting of the nanoparticle core before the start of the cooling process. In figure (a), several radial distribution functions are presented. Curves "entireNP" and "NPcore" are calculated at 800 K, i.e., in the molten globule state, for the core of the nanoparticle (744 atoms) only and for the entire nanoparticle (2048 atoms), respectively, while curve "300K" is the RDF for the entire nanoparticle at 300K. For ease of comparison with the "entireNP" curve, the "NPcore" curve was scaled by a factor of 0.36. The bottom images represent the particle with 5324 atoms, cut at the plane $z = 0$, (b) before the start of the annealing process and (c) when the particle was melted.

(a) (b)

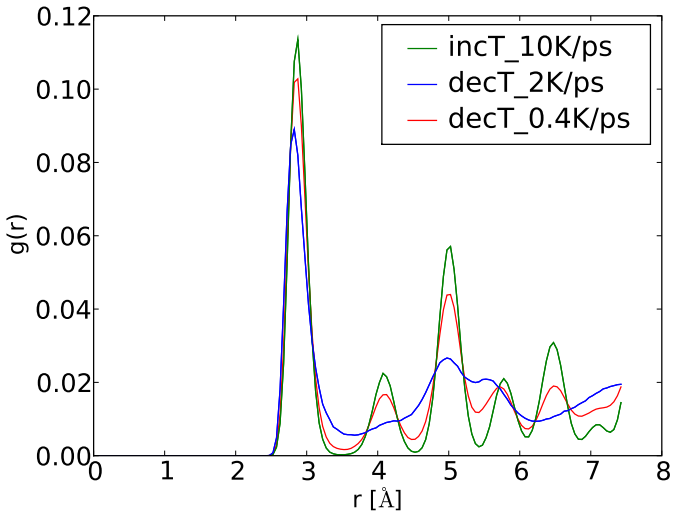

(c)

Figure 5.2: Atomic configuration, at 300 K, of the particle of approximately 5.5 nm diameter (5324 atoms) cooled down from 1000 K with cooling rates of (a) 20K/10ps or 2 K/ps and (b) 20K/50ps or 0.4 K/ps. (c) The radial distribution function, at the end of the 300 K temperature step, for the process of increasing the temperature and for the two cooling processes used.

cooling rate of 2 K/ps, while the second rate emulated a 0.4 K/ps rate, by increasing the running time per temperature step to 50 ps. As shown in figure 5.2(a), for the higher cooling rate of 2 K/ps no local order is visible, while for the slower rate of 0.4 K/ps, in figure 5.2(b), it is possible to visualise the crystal planes even in the core of the nanoparticle. Nevertheless, it is still possible to distinguish several grains with different crystal orientations. This implies that even this slower cooling rate is too fast

to allow the creation of fewer nucleation sites and a fast crystal growth. The presence of local order can also be verified by the RDF in figure 5.2(c). Comparing the curves of the cooling rates ("decT_2K/ps" and "decT_0.4K/ps") with the curve of the increasing temperature ("incT_10K/ps"), it is possible to conclude that for the slower cooling rate the majority of the peaks are well defined and in reasonable agreement with the peaks present before the melting occurs. This is not the case for the higher cooling rate curve, where all peaks except for the first are either not well defined or not present.

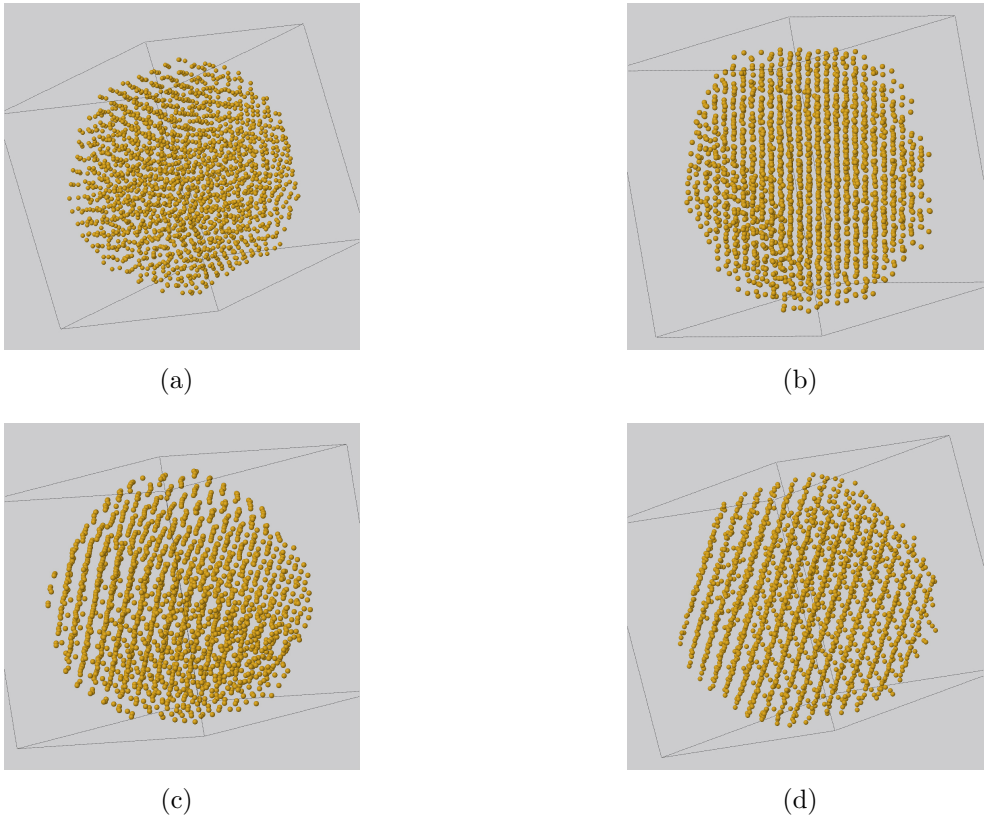

(a) (b) (c) (d)

Figure 5.3: Atomic configuration, at 300 K, of the particle with approximately 4 nm diameter (2048 atoms) cooled down from 900K with cooling rates of (a) 100K/100ps or 1 K/ps, (b) 50K/100ps or 0.5 K/ps, (c) 20K/100ps or 0.2 K/ps and (d) 10K/100ps or 0.1 K/ps.

As for the second simulated nanoparticle, with a diameter of approximately 4 nm (2048 atoms), the two higher cooling rates were used to estimate the cooling time needed to crystallise. For the highest cooling rate, 1 K/ps, the cooling process occurred from 900 K to 200 K, in 100 K steps, with each step being simulated for 100 ps. The

second highest cooling rate was obtained by a similar process, but with temperature steps of 50 K, i.e., equivalent to a cooling rate of 0.5 K/ps. The atomistic configurations resulting from these two cooling processes are shown in figures 5.3(a) and 5.3(b). As can be noted, at the higher cooling rate, although some crystal planes are already beginning to form at the outer layers of the nanoparticle, its centre still seems to be in an amorphous state. For the slower cooling rate of 0.5 K/ps, the presence of crystal planes throughout the nanoparticle is already visible. The RDF results for this particle, shown in figure 5.4(b), also confirm this. For the higher cooling rate of 1 K/ps ("decreasingT_100Ksteps"), the second and third neighbours peaks are still not completely distinct, while for the slower cooling rate of 0.5 K/ps ("decreasingT_50Ksteps") the discrimination of the second and third peaks is clearer.

Taking into account the results from both nanoparticles, we can conclude that a cooling time of the of order 1 ns is needed for the crystallisation of the annealed nanoparticle. The same results also indicate that a crystal structure in the nanoparticle can only start to form with cooling rates of the order of 0.5 K/ps. In the next section, a study of the effects of the cooling rates and initial cooling down temperature (T_h) on the nanoparticle's final crystal structure is presented.

5.2.3 Effect of cooling rate on the crystal structure

According to computational studies described in review [97], a very fast cooling rate is of the order of 50 K/ps. According to the same reference, a realistic cooling rate is in the range of 0.0001-0.005 K/ps. Experimentally, much slower cooling rates, $7 - 10 \times 10^{-13}$ K/ps [96] are used, something impossible to reproduce in simulation.

In order to study the relationship between the cooling rate and the crystal order of a nanoparticle, several cooling rates are explored, using the nanoparticle with diameter of approximately 4 nm (2048 atoms). This nanoparticle was cooled from 800 K or 900 K to 300 K or 200 K, respectively, with temperature steps of 100, 50 and 20 K for the first case (annealing from 800 K) and 100, 50, 20, 10 and 5 K steps for the second case (annealing from 900 K). At each temperature step, the simulation ran for 100 ps, i.e., modelling cooling rates of 1, 0.5 and 0.2 K/ps for the first case and of 1, 0.5, 0.2, 0.1 and 0.05 K/ps for the second case.

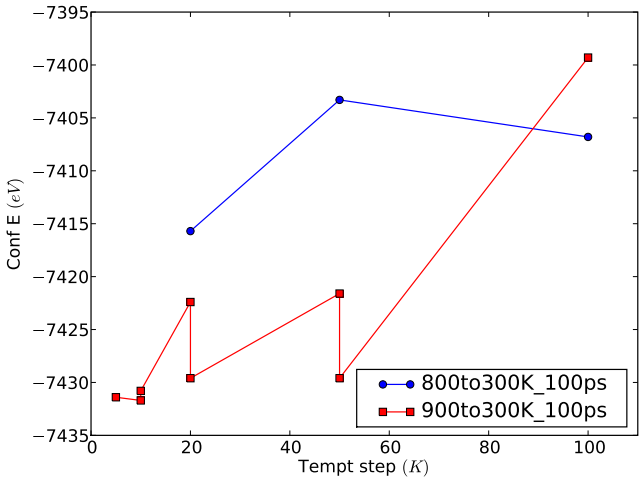

(a)

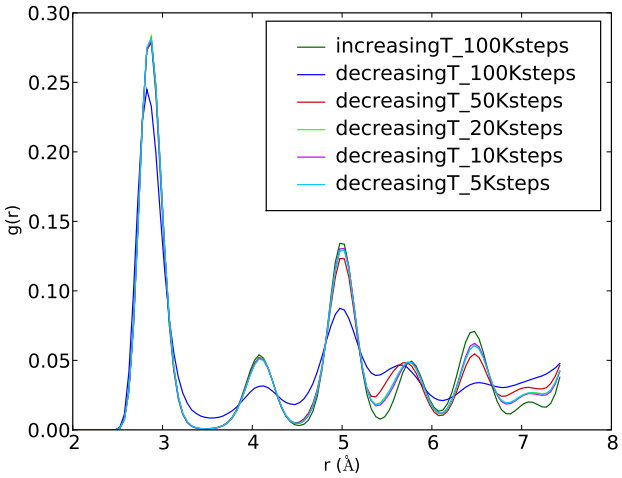

(b)

Figure 5.4: Results for the particle of approximately 4 nm diameter (2048 atoms). (a) Configuration energy versus temperature step for the several cooling processes simulated. All the configuration energies are for the nanoparticles at 300 K. (b) Radial distribution functions after the heating and several cooling processes, for the case when cooling starts at 900 K.

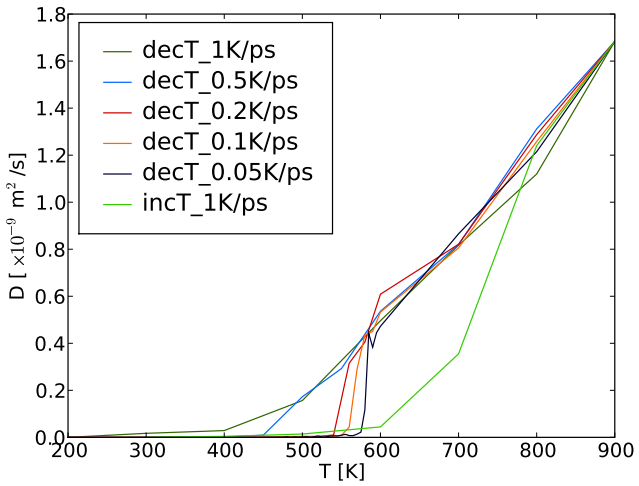

(a)

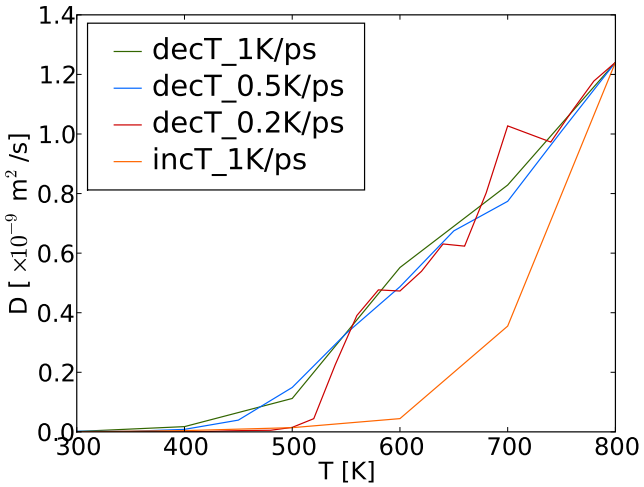

(b)

Figure 5.5: Results for the particle of approximately 4 nm diameter (2048 atoms). (a) Diffusion coefficients for the heating and several cooling processes, for the case when cooling starts at 900 K. For clearer diffusion curves, beyond temperatures of 600 K, the values are plotted at every 100 K. (b) Diffusion coefficients for the heating and the different cooling processes, when the cooling started at 800 K.

The values of the final configuration energy obtained with the different conditions used are plotted in figure 5.4(a). There is an overall tendency to obtain lower values of configuration energy with slower cooling rates, which implies an atomic structure with fewer imperfections. The results of the diffusion coefficient for several cooling rates are presented in figures 5.5(a) and 5.5(b). We can observe that slower cooling rates obtain a significant reduction in the diffusion coefficient at higher temperatures. This implies that particle recrystallisation starts earlier, allowing a better atomic organisation, once again supporting the previous remark. As for the comparison between structures obtained with the same cooling rate, it is evident that nanoparticles with lower configuration energy occur when the cooling process starts with a temperature higher than the melting temperature (figure 5.4(a)). This result suggests that a more stable particle is achieved if the cooling process starts from a temperature higher than T_{mc}. Furthermore, even with such a reduced number of data points, we can verify that for the slower cooling rates of 0.05 and 0.1 K/ps (i.e., temperature step of 5 and 10 K, respectively), there is no significant change in the configuration energy.

Comparing all the radial distribution functions obtained with annealing from 900 K to 300 K with different cooling rates, figure 5.4(b), it is verified that for cooling rates slower than 0.2 K/ps (20 K steps), no significant change in the atomic distribution of the atoms is noted, although we can see from figure 5.4(a), that there is still a reduction in the system configuration energy.

The atomic configurations for some of the cooling rates used are presented in figure 5.3. From these snapshots, it seems that slower cooling rates imply crystallisation of the nanoparticle with bigger grains.

Taking all these observations into account, it was decided that an appropriate cooling rate to allow the formation of crystal structure in the nanoparticles selected, while keeping the computational cost of the simulations tractable, would be of 10K/100ps or 0.1 K/ps. It is important to point out that for bigger nanoparticles, the cooling rate should be even slower, to allow a better atomic rearrangement and the formation of crystal planes. Also, it was decided to start the cooling process with a temperature above the melting temperature of the nanoparticle. The only exceptions were for the bigger nanoparticles, where the annealing conditions were adjusted, so that the computational cost was not excessive. All the conditions imposed to anneal the several assemblies of atoms, in order to create nanoparticles of several sizes, are listed in table 5.1. The results of all the annealed nanoparticles are shown in appendix D.

5.3 Analysis of nanoparticle structure

The crystal structure of the different annealed particles is evaluated by the local order parameter, ψ. This is a single numerical value that measures the degree of order surrounding an atom, with respect to a perfect crystal structure, as explained in more detail in section 4.6.

In table 5.1, the value for the averaged order parameter, $\langle OP \rangle_{10K}$ is presented. This value is related with the the minimised configuration energy, obtained by relaxing the nanoparticle for 10 ps at 10 K. This $\langle OP \rangle$ value is obtained with

$$\langle OP \rangle = \frac{1}{N} \sum_{i}^{N} \psi_i \tag{5.2}$$

where i is the atom index and N is the total number of atoms. As the tabulated values indicate, none of the particles created present a perfect crystal structure. Nevertheless, for most of the nanoparticles, the lower value of the averaged local order parameter is obtained with faster cooling rates. In the following pages, a more detailed analysis for each particle is presented.

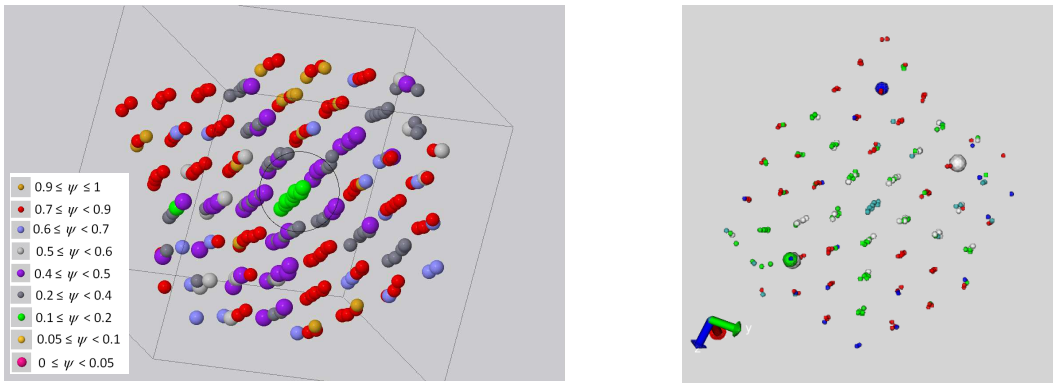

(a) (b)

Figure 5.6: Structure of the particle with diameter of approximately 2 nm (256 atoms), at 300 K, when the (a) local order parameter colour scheme is used. The circle marks the meeting point of five twin boundaries. In (b), the atoms with more than twelve neighbours are highlighted by increased volume. Different perspectives are shown in the two images. Also, two imaging conventions are used, with the left image obtained with Jmol and the right image with VMD.

For the smaller particle annealed, with approximately 2 nm in diameter, the order parameter result is presented in figure 5.6. Five different crystalline orientations

separated by five twin boundaries are visible. The five twin boundaries intersect at a common region, marked with a circle. Additionally, some atoms were identified with more than twelve nearest neighbours, consequently exceeding the maximum number for an FCC structure.

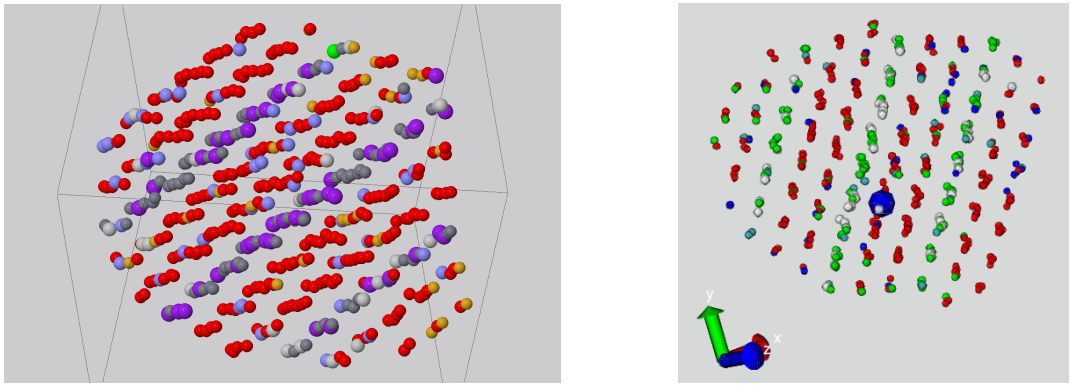

(a) (b)

Figure 5.7: Structure of the particle with diameter of approximately 2.5 nm (500 atoms), at 300 K, when the (a) local order parameter colour scheme is used. In (b), the atoms with more than twelve neighbours are highlighted by increased volume. Different perspectives are shown in the two images. Also, two imaging conventions are used, with the left image obtained with Jmol and the right image with VMD.

The particle shown in figure 5.7, with a diameter of approximately 2.5 nm, presents two parallel twin boundaries between three different crystal orientation zones, at least. A particle with this kind of defect, which has been observed experimentally in [98], is called "lamellar-twinned" particle. Additionally, some atoms were identified with more than twelve nearest neighbours, hence exceeding the maximum number for an FCC structure.

For the case of the particle with a diameter of approximately 3 nm, figure 5.8, five twin boundaries are identified and, similarly to the particle with diameter of approximately 2 nm, seem to be related to a common source region, marked with a circle.

For the particle with approximately 3.5 nm diameter, figure 5.9, a main twin boundary is identified, separating the two main grains with different orientations. Two smaller twin boundaries, located closer to the particle surface, are also present but not evident in the images presented here. Additionally, some atoms were identified with more than twelve nearest neighbours, thus exceeding the maximum number for an FCC structure.

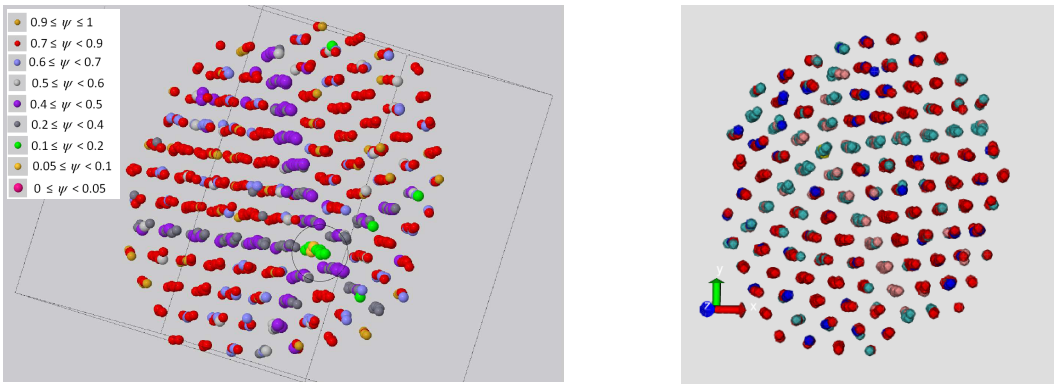

(a) (b)

Figure 5.8: Structure of the particle with diameter of approximately 3 nm (864 atoms), at 300 K, when the (a) local order parameter colour scheme is used. The circle marks the meeting point of five twin boundaries. In (b), the atoms with more than twelve neighbours are highlighted by increased volume. Different perspectives are shown in the two images. Also, two imaging conventions are used, with the left image obtained with Jmol and the right image with VMD.

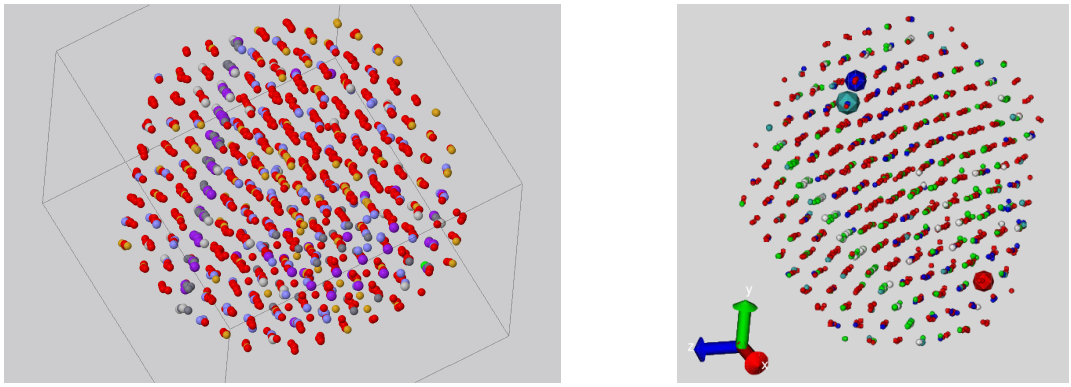

(a) (b)

Figure 5.9: Structure of the particle with diameter of approximately 3.5 nm (1372 atoms), at 300 K, when the (a) local order parameter colour scheme is used. In (b), the atoms with more than twelve neighbours are highlighted by increased volume. Different perspectives are shown in the two images. Also, two imaging conventions are used, with the left image obtained with Jmol and the right image with VMD.

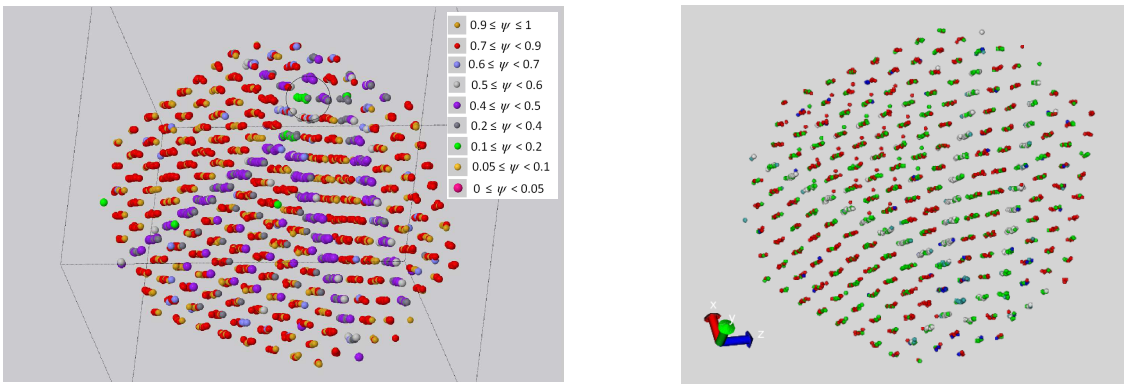

(a) (b)

Figure 5.10: Structure of the particle with diameter of approximately 4 nm (2048 atoms), at 300 K, when the (a) local order parameter colour scheme is used. The circle marks the meeting point of five twin boundaries. In (b), the atoms with more than twelve neighbours are highlighted by increased volume. Different perspectives are shown in the two images. Also, two imaging conventions are used, with the left image obtained with Jmol and the right image with VMD.

As for the particle with approximately 4 nm in diameter, figure 5.10, several crystal grains are visible and separated by twin boundaries that, once again, seem to originate at a particular region, marked with a circle.

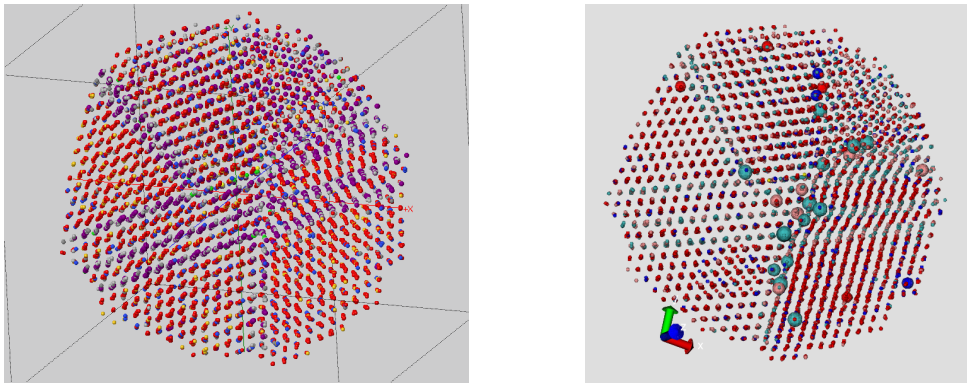

(a) (b)

Figure 5.11: Structure of the particle with diameter of approximately 7 nm (10976 atoms), at 300 K, when the (a) local order parameter colour scheme is used. In (b), the atoms with more than twelve neighbours are highlighted by increased volume. Different perspectives are shown in the two images. Also, two imaging conventions are used, with the left image obtained with Jmol and the right image with VMD.

For the case of the particle with approximately 7 nm diameter, figure 5.11, several crystal domains are visible and separated by twin boundaries. It also presents two

parallel twin boundaries, crossing the middle of the nanoparticle. Additionally, some atoms were identified with more than twelve nearest neighbours, consequently exceeding the maximum number for an FCC structure.

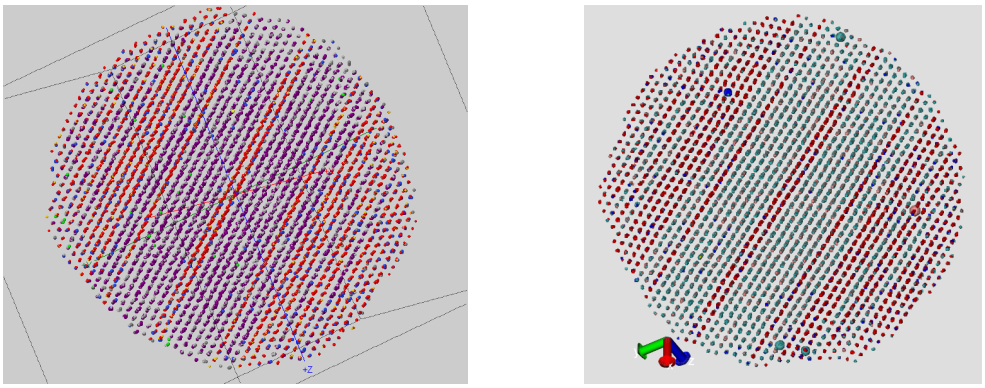

(a) (b)

Figure 5.12: Structure of the particle with diameter of approximately 10 nm (32000 atoms), at 300 K, after being cooled down from 1400 K at a rate of 10K/100ps. In (a), the local order parameter colour scheme is used. In (b), the atoms with more than twelve neighbours are highlighted by increased volume. Different perspectives are shown in the two images. Also, two imaging conventions are used, with the left image obtained with Jmol and the right image with VMD.

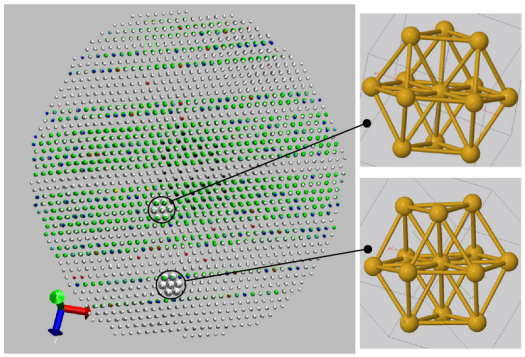

Figure 5.13: Evidence of the regions with HCP (highlighted by top cluster) and FCC (highlighted by bottom cluster) structure in the particle with approximately 10 nm diameter. Main image obtained with VMD, atomic clusters obtained with Jmol.

The particle shown in figure 5.12, with approximately 10 nm diameter, presents several crystal domains. These domains are either in a FCC structure or in an hexagonal closed packed (HCP) structure, as pointed out in figure 5.13. Additionally, some atoms

were identified with more than twelve nearest neighbours, consequently exceeding the maximum number for an FCC structure.

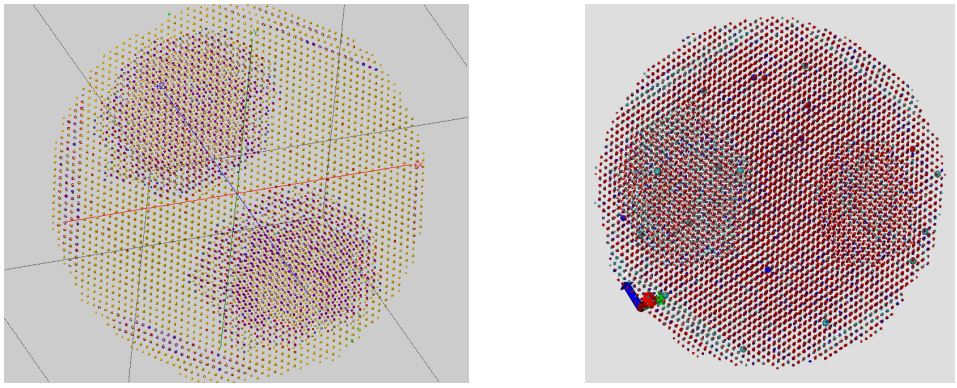

(a) (b)

Figure 5.14: Structure of the particle with diameter of approximately 14 nm (84985 atoms), at 300 K, when the (a) local order parameter colour scheme is used. In (b), the atoms with more than twelve neighbours are highlighted by increased volume. Different perspectives are shown in the two images. Also, two imaging conventions are used, with the left image obtained with Jmol and the right image with VMD.

The defects present in the particle with approximately 14 nm diameter, figure 5.14, are quite different from the ones present in other particles. These differences arise from the different annealing conditions used. As the cooling process did not start from the melting point, due to the excessive computation time required, the core of the nanoparticles does not present any defects. On the other hand, the outer corona of the nanoparticles presents several twin boundaries and areas with HCP structure. Additionally, some atoms were identified with more than twelve nearest neighbours, thus exceeding the maximum number for an FCC structure.

From the particles with 2 nm, 3 nm and 4 nm in diameter, it is evident that the joining point of the five twin boundaries leads to a two dimensional pentagon shape, instead of the regular two dimensional hexagon shape. The source of these five twin boundaries seems to be related to a five-fold star symmetry, cited in [98] and experimentally observed in [99, 100], as shown in figures 5.15(a) and 5.15(b). This is usually due to a nucleation from an icosahedron or decahedron. In figure 5.15(c), we can observe the smallest particle created computationally. Comparing the experimental particle with the computational one, it is possible to note the similarities between the two.

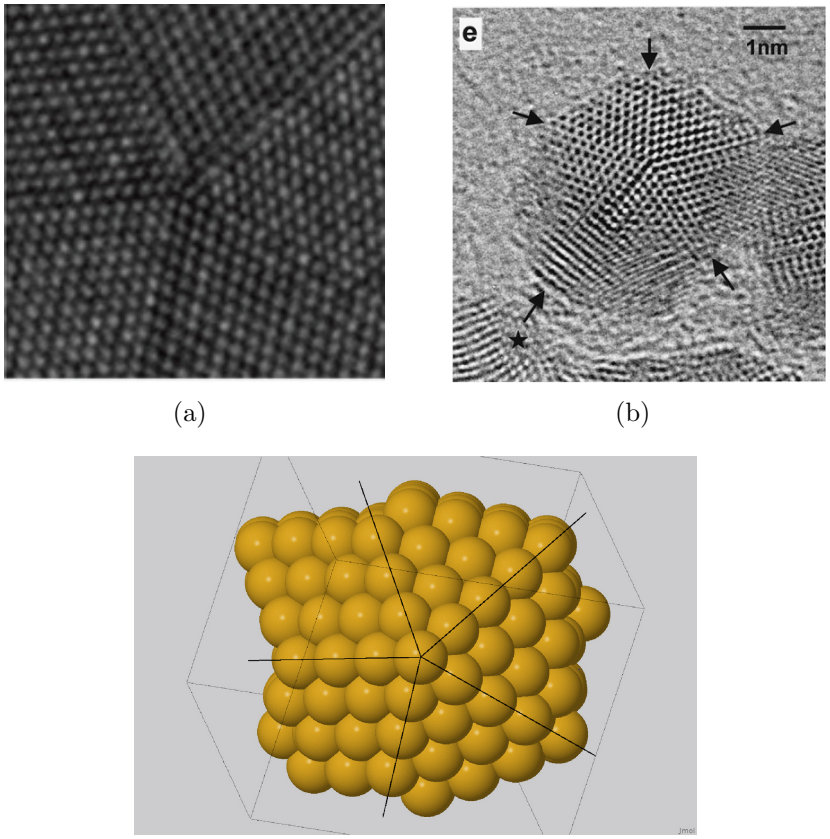

(a) (b)

(c)

Figure 5.15: Images of gold nanoparticles, obtained experimentally and computationally, presenting five-fold symmetries. (a) Zoom of the 17 nm radius defect-free decahedral gold nanoparticle core, obtained experimentally by high-resolution electron microscopy (HREM) by Johnson *et al.*. For more information concerning the particle, please refer to [99]. (b) HREM image of a gold nanoparticle with a 5 nm diameter and obtained experimentally by Oku *et al.*. Twin boundaries are indicated with arrows. For more information about the particle, please refer to [100]. (c) Image of the computationally obtained particle with 256 atoms (diameter of approximately 2 nm).

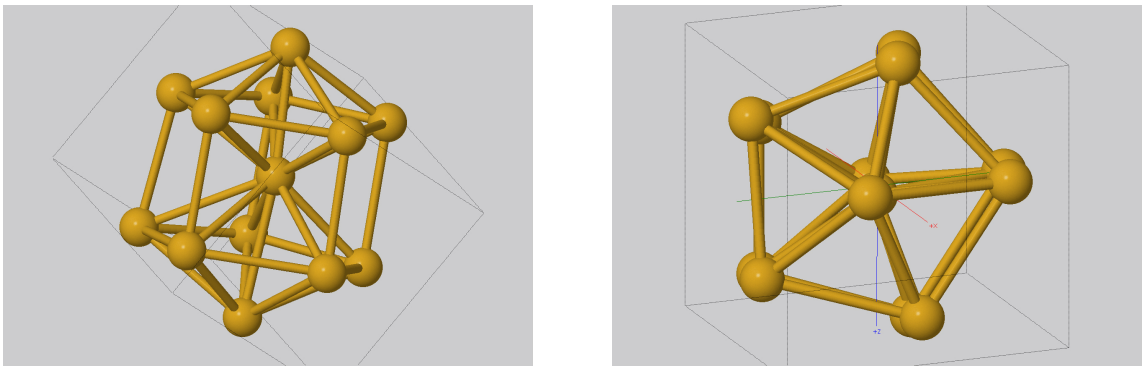

(a) (b)

Figure 5.16: (a) Side and (b) top view of the structure of the twelve neighbours surrounding an atom localised in the intersection of the five twin boundaries.

In figure 5.16, we have a closer look at the base structure of the five-fold star symmetry presented in figure 5.15(c). It is possible to verify that the nucleation does not happen around an icosahedron but instead seems to be based on a cluster with fifteen faces. This state can be associated to the fact that, computationally, the structure did not crystallise at the minimum energy, possibly because the cooling rate was not slow enough.

Most of the particles created, namely the particles with 2 nm, 2.5 nm, 3.5 nm, 7 nm, 10 nm and 14 nm diameters, presented some atoms with thirteen neighbours, as can be verified by the images (b) from figures 5.6 to 5.12. Although this is not expected, since the maximum number of first neighbours should be twelve, this seems to be related with the fact that these atoms tend to be located near the surface of the nanoparticle, thus being less constrained by the surrounding atoms.

The neighbour atoms are selected if the distance between the two atoms is within half the distance between the first and second neighbours of an FCC regular structure. This implies that if the atoms surrounding the central atom are readjusted and if their distance to the central atom is somehow bigger, then a thirteenth atom can be accommodated within this cutoff distance. So, although energetically this would not be a favourable atomic distribution, the fact that this anomaly is located near the surface implies that the atoms are less restrained/stressed. As can be verified in appendix E, at the lower temperature of 10 K most of the nanoparticles no longer present atoms with thirteen neighbours. The only exception is the particle with approximately 7 nm in diameter, which also presents atoms with extra neighbours in the centre of the

nanoparticle and even when the structure is minimised to 10 K. The reason why this happens can be related with the annealing conditions used. For instance, the cooling process did not start at a temperature high enough and the cooling rate used was too fast to allow atomic arrangement.

As for the type of structure yielded by these clusters of thirteen atoms surrounding a central atom, it seems to be a hybrid between the six-fold symmetry, associated with the cuboctahedron formed around the FCC (1 1 1) plane, and the five-fold star symmetry, related to the icosahedron. Several images showing the atomic arrangement of a cluster formed by an atom and its thirteen neighbours are presented in figures E.1 and E.2 in appendix E.

5.4 Summary

This chapter presents the main results concerning the production and characterisation of several nanoparticles obtained by computational methods. The creation of the nanoparticles is modelled by mimicking the annealing processes used experimentally. These particles, which are later on used in chapter 8, aim to resemble the ones used experimentally in biomedical applications, as they do not present a perfect surface and structure.

The results show that the minimum cooling time needed to obtain a nanoparticle with a non-amorphous core is of the order of a few nanoseconds. Furthermore, the cooling rate of the order of 0.5 K/ps is the fastest that still allows crystallisation.

In terms of structure analysis, none of the particles created are defect free. Nanoparticles smaller than 3 nm in radius present mainly twin boundaries separating regions of perfect FCC structure. In some cases, these twin boundaries meet at a two dimensional pentagon shape, in clusters with fifteen faces. The structure of these clusters seems to be related with the five-fold star symmetry of the metastable state of an icosahedron. The nanoparticles bigger than 3 nm in radius show mainly twin boundaries between regions with different crystal orientation. For the nanoparticles with radius bigger than 5 nm, some areas with HCP structures in the middle of FCC crystal structures are identified.

Chapter 6

Analytical and computational studies of heat transfer for bare gold-water systems

6.1 Introduction and motivation

One of the ultimate goals of this thesis is to understand and optimise the use of gold nanoparticles as heat sources or light scatterers for biomedical applications. For that, we explore the thermal and mechanical evolution of a system of hot gold nanoparticles embedded in a colder medium when steady state is reached.

The thermal behaviour of such a system appears, at first sight, obvious: heat flows from the points at higher temperatures to the points at lower temperatures. What is not completely trivial is the mechanism by which heat flow occurs, the influence of the system composition on heat flow and the dependence of the thermal relaxation time on the initial conditions of the system. To explore such a system and answer these questions, it is important to understand the basic ideas and simple concepts of heat transfer, as exposed in section 2.1.

This chapter will therefore start with analytical calculations of heat flow in our system of interest. While performing these calculations, it was necessary to determine the value of one of the parameters - the heat transfer coefficient across a surface - for the gold-water interface. To estimate this value, non-equilibrium molecular dynamics, described in section 4.2, were used. Comments on the value of the heat transfer coefficient and its impact on the overall heat flow are presented.

6.2 Heat flow at extreme conditions, an analytical approach

As discussed in section 2.1, during the first few nanoseconds, the main heat transfer mechanism in a system of hot gold nanospheres embedded in cold water is the heat conduction. The three main heat conduction mechanisms in this system are: conduction in the gold, conduction through the interface and conduction in the water. As the heat flow in this system happens through a chain of these heat conduction mechanisms, it is important to understand which of these can be the bottle neck for the overall heat transfer. For this reason, the heat conduction equation for this simple system of hot gold nanoparticles embedded in water is solved analytically for two extreme conditions:

- The heat flow completely dominated by the thermal conduction in the medium that surrounds the particle.
- The heat flow limited by the heat transfer through the interface between the particle and the medium.

The case of the heat flow being limited by the gold particle is not considered, since gold has a very large thermal conductivity (320 W m^{-1} K^{-2}) when compared to water (0.58 W m^{-1} K^{-2}), which implies that heat should diffuse considerably faster within the gold than in water.

6.2.1 Heat flow dominated by the conduction in the medium

Let us consider a body surrounded by a medium with constant thermal conductivity k_m and at the initial temperature T_c. It is assumed the body is a sphere of radius R and remains at a constant temperature T_h (where $T_h > T_c$). As the system evolves, the temperature of the medium will increase, but it is assumed that the medium is so immense that very far away from the particle the temperature is always T_c. Under these conditions, the system will eventually reach a steady state regime, where the temperature profile between the body and the boundary of the medium remains constant.

In order to solve the heat conduction equation (equation 2.5 presented in page 21), for this system (from $r > R$ to infinity, i.e., no energy source is present in the system) and considering the above description, it is assumed the following boundary conditions, in spherical coordinates, must be obeyed:

- at $r = R$, $T(r) = T_h$
- at $r \to \infty$, $T(r) = T_c$

The equation for heat conduction can be then reduced to

$$\frac{d}{dr}\left[r^2 \frac{dT}{dr}\right] = 0 \tag{6.1}$$

and its solution gives the temperature of the water as

$$T(r) = T_c + \frac{(T_h - T_c)R}{r}, \text{ for } r > R \ . \tag{6.2}$$

Using Fourier's Law (equation 2.1 in page 20), the rate of heat flow (Q_{cond}) can be determine to be

$$Q_{cond} = 4\pi(T_h - T_c)k_m R \ . \tag{6.3}$$

For the case of a gold nanoparticle in water, let us assume that the radius of the particle R is 2 nm, the temperature of the sphere T_h is 800 K and the temperature of the medium T_c is 300 K. The value of the thermal conductivity of the water is 0.58 W m^{-1} K^{-2}.

Substituting these values in equation 6.3, the value for the rate of heat flow is obtained and shown in table 6.1.

Table 6.1: Rate of heat flow at steady state, from analytical results, for the extreme case of heat flow dominated by the heat conduction in the medium.

medium	Q_{cond} (steady state)
water	7.288×10^{-6} J s^{-1} 45.5 eV ps^{-1}

6.2.2 Heat flow dominated by the gold-water interface

When a solid is put into contact with a solid/liquid/gas at a different temperature, a heat flux q at the interface of the two materials occurs and is proportional to the

temperature difference ΔT between the two surfaces (i.e., $q \propto -\Delta T$, for a certain assumed direction), as described by Newton in 1701[15]. The equation that describes this heat flux, also known as Newton's cooling law, is

$$-k_{mat}\nabla T = q = -H\Delta T \quad , \tag{6.4}$$

where $H = k_{mat}h_{mat}$ is related to the properties, geometry and dimensions of the interface. where H can be interpreted as the resistance imposed by the interface to the heat transfer and is related to the properties, geometry and dimensions of the interface. H can also be expressed in terms of either of the materials (1 or 2) that constitute the interface: $H = k_{mat1}h_{mat1} = k_{mat2}h_{mat2}$, where k_{mat} is the thermal conductivity and $1/h_{mat}$ is a characteristic thickness that reflects the resistance imposed by the interface. This H (in some references also labelled as G) is known as *heat transfer coefficient*[16, 101], *surface conductance, coefficient of surface heat transfer*[102], *interfacial thermal conductance*[60], *interface conductance*[56] or *Kapitza conductance*[56, 60, 61]. This heat transfer coefficient exists at the interface between any distinct materials and it is attributed to an interruption on the regular propagation of phonons. One of the main models justifies it as due to the difference in densities and sound speeds between the two materials, which leads to an acoustic-impedance mismatch[57]. This causes a change on the heat conduction at the interface between dissimilar materials. For instance, this model seems to explain the results in reference [52], where the temperature profile of systems of heated metal nanoparticles embedded in glass are investigated with ultrafast pump-probe spectroscopy. Another competing model, the diffuse mismatch model, suggests that every phonon that hits the interface "loses" its memory, leading to a reduction of the heat transfer through the interface[57]. According to reference [103], for a metal-liquid helium interface, the transferred heat can be due to the interaction between the conduction electrons and the reflected phonons in the liquid helium.

Let us now consider the analysis of the system under study, for the limiting case of the heat transfer dominated by the interface gold-water. As the interface involves two materials, the rate of heat transfer is going to be solved independently for the gold and the water. Therefore, the heat conduction equation will be solved in (I) from the point of view of the gold particle releasing heat to the surrounding medium and in (II) from the standpoint of the water absorbing the heat released by the particle.

I. Particle releasing heat to the surrounding medium

For this approach, the particle is modelled as a body with thermal conductivity k_p surrounded by a medium with thermal conductivity k_m. The medium has a high heat capacity so that its temperature is always at a constant value of T_c. Let us suppose the particle is a sphere of radius R and it is initially at temperature T_h (where $T_h > T_c$). Furthermore, the thermal conductivity of the particle is assumed to be very high when compared to the heat transfer coefficient of the surface H, so that the temperature in the particle is always homogeneous. In these conditions, the system will reach the uniform temperature of T_c after some time.

With these assumptions, the temperature equation for the particle is predicted to be independent of the distance to the centre of the sphere, as long as it is limited to R.

The heat equation, in spherical coordinates, for this system, based on equation 2.5, in page 21, is

$$k_p \left[\frac{1}{r^2} \frac{\partial}{\partial r} \left(r^2 \frac{\partial T}{\partial r} \right) \right] = c_p \rho_p \frac{\partial T}{\partial t} \tag{6.5}$$

and the following boundary and initial conditions must be obeyed:

- at $r < R$ and $t = 0$, $T(t) = T_h$
- at $r < R$ and $t \to \infty$, $T(t) = T_c$
- at $r = R$, the temperature gradient is $\frac{\partial T}{\partial r} = h_p(T_c - T(t))$, where h_p represents the inverse of the material's thickness that the heat would have to propagate by conduction. This thickness would impose a resistance on the heat propagation, equivalent to the one set by the interface between the two materials.
- at $r < R$, the temperature gradient is $\frac{\partial T}{\partial r} = 0$

Solving equation 6.5, the solution obtained for the temperature of the body is

$$T(t) = T_c - (T_c - T_h) e^{-\frac{3H}{c_p \rho_p R} t} \tag{6.6}$$

and using equation 2.1, the rate of heat flow (Q_i) can be determined as

$$Q_i = 4\pi R^2 H (T(t) - T_c) \quad . \tag{6.7}$$

From equation 6.6, a relaxation time τ can be obtained as

$$\tau = \frac{c_p \rho_p R}{3H} \quad . \tag{6.8}$$

This variable τ, also known as convection time[18], will be referred to as the "interface relaxation time" here to avoid confusion. It can be interpreted as the time scale over which the temperature of the body changes by $1/e$ of the maximum possible temperature change.

Using this interface relaxation time, it is also possible to estimate the distance that the heat will flow due to conduction in the medium only. This distance L is given by

$$L \propto \sqrt{\alpha_m \tau} = \sqrt{\frac{k_m}{c_m \rho_m} \tau} \quad , \tag{6.9}$$

where α_m is the thermal diffusivity of the medium.

If this distance is considerably bigger than the radius of the particle, then the conduction in the medium does not limit the heat transfer in the system; rather, heat flow across the body-medium interface is the limiting factor. On the other hand, if the distance L is of the same order of magnitude or smaller than the radius of the particle, then the heat flow in the medium may be the limiting step in the heat flow in the system.

For the system of a gold nanoparticle in water, the radius of the particle R is assumed to be 2 nm, the initial temperature of the sphere $T(t = 0) = T_h$ is 800 K and the temperature of the medium T_c is 300 K. The value of the heat transfer coefficient used is the one obtained experimentally from macroscale measurements and presented in reference [15], with value approximately 100 W m^{-2} K^{-1}. Using these figures and the values of the other variables presented in appendix B, the values in table 6.2 are obtained.

Table 6.2: Analytical results for the extreme case of heat flow dominated by the interface, for the situation where the particle is releasing heat to the surrounding medium.

medium	$Q_i(t = 0)$	τ	L
water	2.51×10^{-12} J s^{-1}	1.66×10^{-5} s	1.56×10^{-6} m
	1.57×10^{-5} eV ps^{-1}	16.6 μs	1.56 μm

II. Medium absorbing the heat from the particle

For this case, the same system as in approach (I) is considered and only the boundary conditions are changed. The particle is now kept at a constant temperature T_h, while the medium is initially at temperature T_c (where $T_c < T_h$). In these conditions, the system will reach the uniform temperature of T_h after some time.

To solve the heat equation for this system (from the sphere border to infinity) and from the above description, the following boundary and initial conditions, in spherical coordinates, must be obeyed:

- at $r > R$ and $t = 0$, $T(t) = T_c$
- at $r > R$ and $t \to \infty$, $T(t) = T_h$
- at $r = R$, the temperature gradient is $\frac{\partial T}{\partial r} = h_m(T(t) - T_h)$, where h_m represents the inverse of the medium's thickness that the heat would have to propagate by conduction. This thickness would impose a resistance on the heat propagation, equivalent to the one set by the interface between the two materials.
- at $r > R$, the temperature gradient is $\frac{\partial T}{\partial r} = 0$, since it is assumed that the interface dominates the heat transfer in the system, hence the heat conduction in the medium is fast enough to justify a uniform temperature distribution.

For this case, the heat conduction equation (equation 2.5) becomes

$$k_m \left[\frac{1}{r^2} \frac{\partial}{\partial r} \left(r^2 \frac{\partial T}{\partial r} \right) \right] = c_m \rho_m \frac{\partial T}{\partial t} \quad . \tag{6.10}$$

Solving the left hand side of this equation, the solution for the rate of heat flow Q_i is obtained

$$Q_i = -4\pi R^2 H(T(t) - T_h) \quad . \tag{6.11}$$

Applying the previous equation to the case of a gold nanoparticle in water and substituting the values from the previous approach (I) for the variables R, T_h and T_c, the result in table 6.3 is obtained.

Table 6.3: Analytical results for the extreme case of heat flow dominated by the interface, for the case of the medium absorbing the heat released by the particle.

medium	$Q_i(t=0)$
water	2.51×10^{-12} J s^{-1}
	1.57×10^{-5} eV ps^{-1}

6.2.3 Intermediate conclusion

For the system and conditions stated and using the values of the rate of heat flow obtained for the two cases considered above, it is possible to conclude that the rate of heat flow through the surface of the gold nanoparticles is smaller, by several order of magnitudes, than the heat flow through the water. That leads us to conclude that the heat flow through the system is limited by the gold-water interface, for the value of heat transfer coefficient H used.

This conclusion is also reinforced by the fact that the calculated distance L, over which heat flows during the characteristic thermal relaxation time of a nanoparticle, is around 1000 times larger than the radius of the nanoparticle. This result shows us that the interface relaxation time, which can be interpreted as the time necessary for the particle to cool down is long enough so heat will diffuse in the water, exclusively by conduction, up to a distance of a thousand times the particle radius. This ratio is high enough that we can confirm that the heat conduction in the water does not limit the heat flow in the system.

These conclusions are also supported by the ratio of the rate of the heat flow due to conduction in the medium (Q_{cond} from equation 6.3) and the heat transfer across the interface (Q_i from equation 6.7) given by[1]

$$\frac{Q_{cond}}{Q_i} = \frac{k_m}{RH} \quad . \tag{6.12}$$

If the result from equation 6.12 is larger than 1, the heat flow through the interface dominates; if not, the overall heat flow is limited by the heat conduction in the medium. For the conditions considered, it is possible to determine which nanoparticle radius R separates the two regimes of heat flow, that is

[1]The inverse of this ratio, that is $\frac{RH}{k_m}$, is known as the Biot number. This number is mainly used in systems where the heat transfer due to convection is taken into account, as referred in [16] and [104].

$$R \approx 0.0058\ m = 5.8\ mm \quad .$$

As can be confirmed, this radius is much larger than the nanoparticle. This leads us to conclude that the heat flow will still be limited by the interface, even when much larger nanoparticles than those typically employed in experiments are used.

However, these conclusions are strongly dependent on the coefficient of heat transfer across the interface H. For the above calculations, the value of H used is experimentally determined for macroscopic systems. Yet, evidence suggests (e.g., reference [56]) that values of H for nanoscale systems may be higher by several orders of magnitude. At the time this work was taking place, no reports concerning the value of H for nanoscale systems similar to ours were found, so this value was estimated through computational methods.

6.3 Bare gold-water heat transfer coefficient

The heat transfer coefficient H, for nanoscale systems, is estimated by using non-equilibrium molecular dynamics (NEMD), already described in section 4.2, in several systems of two gold slabs separated by a water layer of varying thickness. The heat source and sink method is applied to the slab configuration, so that one of the gold slabs behaves as a heat source, while the other gold slab is a heat sink. This induces a temperature difference in the system, which will thermally equilibrate after some time. Once the steady state regime is reached, as described in section 4.3, the value of H can be estimated as explained in section 4.4.

In the next few pages the simulated systems and the environment conditions used are presented, together with the results obtained. The following discussion of the results will be linked to the analytical model described in the previous sections, and will motivate the work presented in the next chapters.

6.3.1 Systems and conditions simulated

The simulated slab systems comprised two gold slabs separated by a water box of various thicknesses (see table 6.4). Each gold slab was created as a perfect FCC lattice, so that its 2160 atoms were distributed over six (1 1 1) planes perpendicular to the z axis. The dimension of each gold slab was $50 \times 52 \times 14$ Å^3. Each water box was also built as

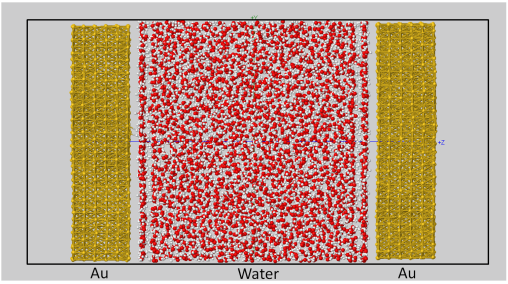

Figure 6.1: Scheme of the system of bare gold slabs separated by a water box and limited by the simulation box in dark grey.

a lattice of water molecules, where the intermolecular distances were set to mimic the water density of 1000 kg m^{-3}. The initial area of each water box, perpendicular to the z axis, was of 47×47 $Å^2$, while the z dimension was changed according to the thickness of water needed. The slab system was then assembled by including each component in the same simulation box, as shown in figure 6.1.

The assembled system was then relaxed for 200 ps under NVT conditions, coupled to a Berendsen thermostat, with a relaxation time of 0.1 ps, at 300 K. The slab conditions were simulated by increasing the z component of the simulation box by approximately 40 Å and by using periodic boundary conditions in three dimensions. A detailed description of the gold-gold, water-gold and water-water interatomic potentials and the cut off distances used is presented in section 4.1.1.

All systems were considered relaxed after 200 ps, as the volume, density of the water slabs and weighted mean temperatures[2] for each gold slabs and water were constant. The average thickness $\langle d_{Wa} \rangle_{rel}$ and density of water layer $\langle \rho_{Wa} \rangle_{rel}$ were also determined, when each system was stable. The evolution of these parameters with time is shown, as an example, in figure 6.2.

At this stage, the systems were set into non-equilibrium conditions with the heat source and sink method, described in sections 4.2.2 and appendix A, for a period of t_{tot}. This method used a 0.1 ps relaxation time and the values for the parameter p presented in table 6.4. Under this non-equilibrium regime, statistics were collected every 5 ps. Using a time interval of 50 ps to calculate the temperature rolling averages and applying the conditions stated in section 4.3, each system was considered to have reached steady state after a time t_{tillSS}. Finally, for each system, the last Δt_{atSS} of statistics were used

[2]Statistics are collected for each slab/corona in the system, as explained in appendix A.3.2. The temperature in each slab/corona contributes to the average temperature of each component in the system with a weight that depends on the number of atoms present in each slab/corona.

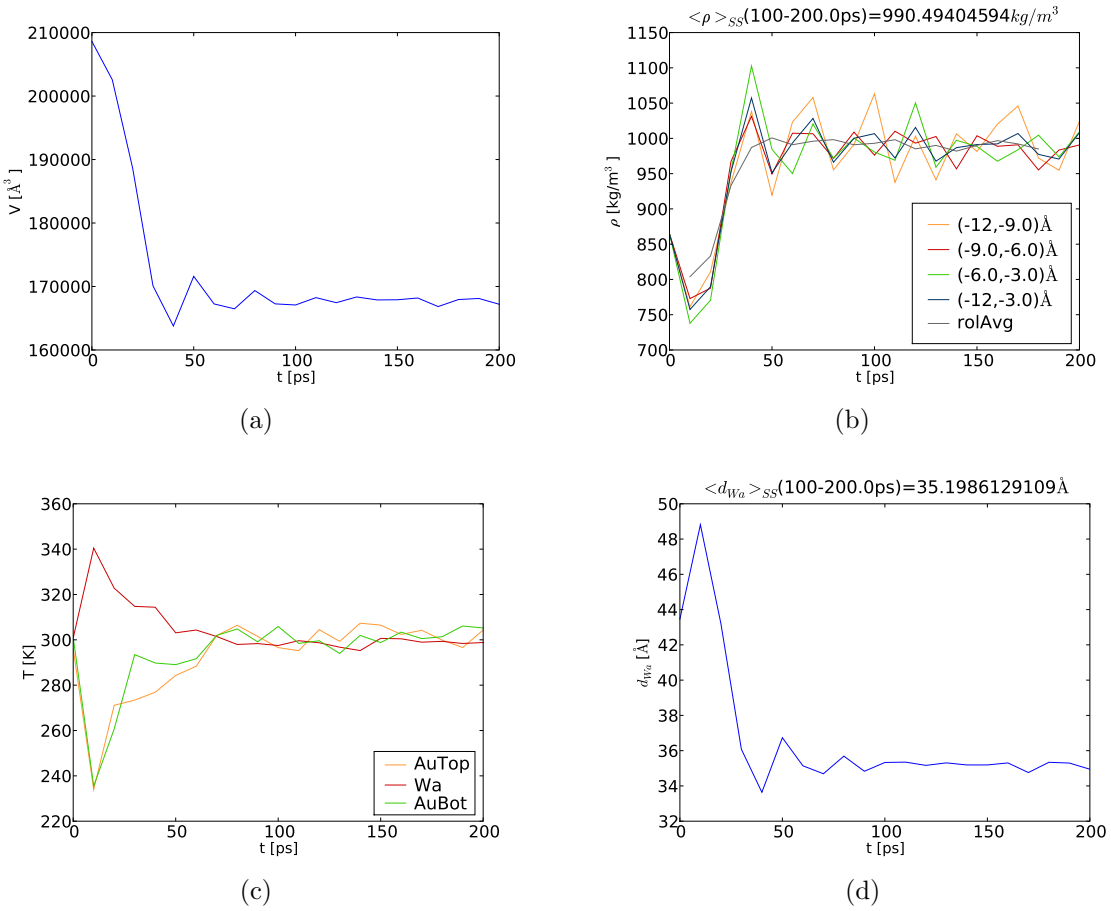

Figure 6.2: (a) Volume, (b) water density for several slab thickenesses (from -12 until -9 Å, from -9 until -6 Å, from -3 Å and from -12 until -3 Å), (c) weighted mean temperature for the different components in the system and (d) water slab thickness evolution over time, when the system of two gold slabs separated by a water slab approximately 35 Å thick is equilibrated. Plots (b) and (d) also present the mean water density and water slab thickness, respectively. The system is considered to be relaxed when all of these parameters are stable.

to determine the average temperatures $\langle T_h \rangle$ and $\langle T_c \rangle$ of each of the gold slabs. as well as the thermal conductivity of the water k_{Wa}. The latter variable was calculated by applying Fourier's law (equation 2.2) to the central water layer with ≈ 10 Å thickness. The average temperature of this central water layer was around 300 K for every system. The values of each of these parameters for each of the systems tested are presented in table 6.4.

Table 6.4: Description of the systems simulated and of the specific conditions used to determine the value of the heat transfer coefficient for the bare gold-water interface.

No. Wa molec.	Relaxation period $\langle d_{Wa}\rangle_{rel}$ [Å]	Relaxation period $\langle \rho_{Wa}\rangle_{rel}$ [kg m^{-3}]	Source sink period p	Source sink period t_{tot} [ps]	Source sink period t_{tillSS} [ps]	Source sink period Δt_{atSS} [ps]	Heat Flux [W m^{-2}]	$\langle T_h\rangle$ [K]	$\langle T_c\rangle$ [K]	k_{Wa} [W m^{-1} K^{-1}]
1125	≈ 9	≈ 1129	0.4	770	≈ 102	320	2.07×10^{11}	≈ 520	≈ 72	-
2250	≈ 22	≈ 999	0.1	1300	≈ 92	900	5.18×10^{10}	≈ 365	≈ 234	≈ 0.42
3375	≈ 35	≈ 990	0.1	785	≈ 127	385	5.18×10^{10}	≈ 373	≈ 226	≈ 0.46
4500	≈ 48	≈ 989	0.1	600	≈ 172	200	1.04×10^{10}	≈ 458	≈ 122	≈ 0.44

6.3.2 Results and discussion

The average temperature values, together with the heat flux, were used to determine the value of the thermal resistance of the system. This thermal resistance served as an intermediate step to determine the heat transfer coefficient for the bare gold-water interface and to estimate the thermal conductivity of water, as explained in section 4.4. The results obtained are displayed in figure 6.3 and table 6.5.

The errors associated with these results are not presented because it is not possible to obtain a realistic estimate. The uncertainties associated with these results need to take into account the random and statistical errors, as well as the limitation due to the method and systems used. These last two error sources, due to their nature, are very difficult to quantify, hence, are not estimated. Regarding the random errors, which are related with the temperature fluctuations in the system, the standard deviation of each averaged temperature was determined to be under 7%. The propagation of this uncertainty to the thermal resistance gives a deviation from the average value of around 9%. We can then estimate that the random errors affecting the thermal conductivity of the water and the heat transfer coefficient should be under 15%.

Table 6.5: Results obtained from the linear regression on the simulation results for the gold-water-gold slab systems.

$U(d) = a \cdot d + b$		$U(d) = \frac{1}{k_{Wa}} \cdot d + \frac{2}{H}$	
a	2.735	k_{Wa}	0.37 W m^{-1} K^{-1}
b	1.917×10^{-8}	H	1.0447×10^{8} W m^{-2} K^{-1}

As can be verified, the value of the thermal conductivity of water obtained with the fit is lower than the ones obtained for each individual system, presented in table 6.4. The reason for this variation could be associated to the section of the system used to obtain each of these values. For the values presented in table 6.4, the water slabs used were of bulk water only. On the other hand, the entire system was used to obtain the value of the thermal resistance used for the fit. As the systems simulated are small, we can expect that the interface effects can be considerable, therefore, lowering the value of the thermal conductivity of water obtained in table 6.5. These values of the thermal conductivity of water are approximately half of the experimental ones (e.g., 0.58 W m^{-1} K^{-1} at 298 K from reference [16]) and also lower than others obtained with computational

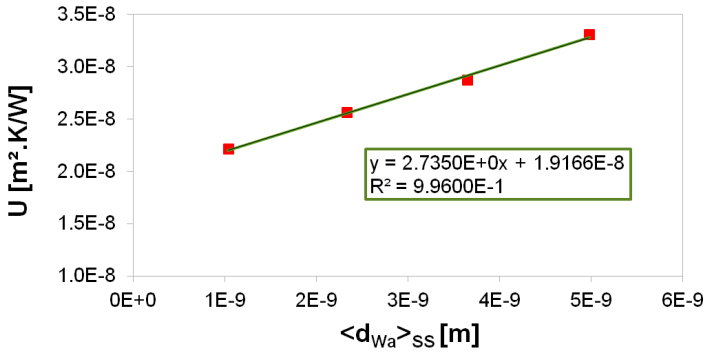

Figure 6.3: Thermal resistance vs water thickness obtained with the simulations of several systems of two gold slabs separated by a water slab. The trend line and equation shown result from a linear regression fit to the points.

methods[82] (0.7-0.87 W m^{-1} K^{-1} at 300-325 K). Initially, it was considered that this difference could be due to a too low average water density of the simulated systems, or to large oscillations in the local water density as a function of the distance from the gold surfaces. Although not shown here, the average water density is approximately 1000 kg m^{-3} and there is a variation of under 5% along the z direction, therefore the density variation cannot account for the low value of the thermal conductivity found. Secondly, the temperature effect on the thermal conductivity was considered. Although not shown here, the thermal conductivity of the water was determined for different water sections within the larger system, which translated into determining the thermal conductivity at different temperatures. The results showed some variation with temperature (under 10%), but these variations are too small to justify the difference in magnitude between our computational results and the experimental values of the thermal conductivity of water. Another possible explanation could be associated with the errors and limitations of the method used. As explained in the previous paragraph, it is not possible to present a realistic estimate of all these errors. What could be estimated was the magnitude due to random errors, which presented values to low to explain the small value of the thermal conductivity obtained in this work.

Regarding the calculated value of H, 104.5 MW m^{-2} K^{-1}, it was compared with reference values in the literature. Computational results by [61] have shown that, for planar systems of self-assembled monolayers (SAMs) with a broad range of surface chemistries (from hydrophobic to hydrophilic) embedded in water, the heat transfer coefficient at the water-SAM interface has values from 40 MW m^{-2} K^{-1}, for hydrophobic

surfaces, to 140 MW m^{-2} K^{-1}, for the hydrophilic surfactants. Experimental results in [56] have shown that planar gold functionalised with 1-octadecanethiol (C_{18}), in order to make the surface hydrophobic, has a heat transfer coefficient of 50 ± 5 MW m^{-2} K^{-1}. The same group has also shown that planar gold functionalised with 11-mercapto-1-undecanol ($C_{11}OH$) becomes hydrophilic, with a value of 100 ± 20 MW m^{-2} K^{-1} for the heat transfer coefficient. The bare gold-water heat transfer coefficient was also obtained experimentally by [105], although this reference was found after the work reported here was done. The value obtained by this group is 105 ± 15 MW m^{-2} K^{-1}. As can be seen, the value of H obtained in our simulations is within the same order of magnitude of all the values presented here, and is even within the error bars of the experimental value of the gold-water heat transfer coefficient.

The value of H estimated from our simulations, 104.5 MW m^{-2} K^{-1}, is several orders of magnitude higher than the values reported in [15] ($H_{eng} = 100 - 300$ W m^{-2} K^{-1}). A possible reason for this difference can be that, in [15], there is no specification of the material solid surface used to do the measurement. To determine the value H_{eng} in [15], it seems the only important condition is determined by which liquid medium (water) is in contact with a solid surface (no compound specified). This lack of detail may signify that at the nanoscale level other elements are present at the surface of the solid (e.g., adsorbed elements) and these may change the properties of the solid surface, which may affect the value of the heat transfer coefficient determined experimentally. Furthermore, the method used to determine such values of heat transfer coefficients may involve more than one interface, as section 10.6 from reference [106] indicates. This implies that the value of H_{ref} is in fact an overall heat transfer coefficient and not a precise value for the specific interface of bare gold and water.

Given that the value of H obtained from our simulations is so different from the ones used in the calculations previously presented, it is important to evaluate how it will affect the heat flow between a particle and the surrounding water. With this new value of H, we recalculate the initial rate of heat flow $Q_i(t = 0)$, for the case of the heat flow dominated by the bare gold-water interface, with equation 6.7. The interface relaxation time τ and the distance L were also recalculated by means of equations 6.8 and 6.9, respectively. The results are shown in table 6.6.

According to Inasawa *et al.*[3], heat dissipates from the particles to the surrounding solvent (water) in approximately 100 ps. Hu and Hartland[49] show that the dissipation

Table 6.6: Analytical results for the extreme case of heat propagation dominated by the interface, with the new value of H, for the situation of the particle releasing heat to the surrounding medium.

medium	$Q_i(t=0)$	τ	L
water	2.62×10^{-6} J s^{-1}	1.593×10^{-11} s	4.52×10^{-8} m
	16.4 eV ps^{-1}	15.93 ps	0.45 nm

time ranges from 10 ps for particles with 4 nm in diameter to 400 ps for 50 nm diameter particles. Both studies present results in line with the interface relaxation time τ obtained.

The new value of rate of heat flow Q_i is of the same order of magnitude as the one obtained for the extreme case of the heat flow dominated by conduction in the medium ($Q_{cond} = 7.288 \times 10^{-6}$ J s^{-1} = 45.5 eV ps^{-1}). This leads us to conclude that, for the studied case of gold nanoparticles embedded in water, the heat flow through the system may either be dominated by the medium conduction or by the water-gold interface.

To understand which of the two heat transfer mechanisms will dominate the overall heat flow in the system, equation 6.12 can be used. With the new value of H, the limit $\frac{Q_{cond}}{Q_i} = 1$, that is, when the rate of heat flow due to the conduction in the medium is equivalent to the rate of heat flow due to the water-gold interface, happens at a radius $R = 5.56 \times 10^{-9}$ m. Therefore, the heat transfer in particles smaller than 5 nm in radius should be dominated by the heat flow through the interface, while in bigger nanoparticles should be limited by the heat conduction in the water. Experimental studies[49] of embedded nanoparticles, ranging from 2 to 25 nm in radius, demonstrated that the heat dissipated by hot nanoparticles embedded in water had a dependence with the square of the radius. As most of the sizes tested were bigger than 5 nm in radius, our argument seems, in a first approximation, reasonable.

6.3.3 Summary

In this chapter, we use computational methods to determine the value of the heat transfer coefficient at the bare gold-water interface, 104.5 MW m^{-2} K^{-1}. This value is several orders of magnitude higher than the initial values found in engineering books ($H_{eng} = 100 - 300$ W m^{-2} K^{-1}, in reference [15]), but in very good agreement with experimental values recently obtained (105 ± 15 MW m^{-2} K^{-1}, in reference [105]).

Moreover, we demonstrate a way to estimate which heat transfer mechanism limits

the overall heat transfer on a system of embedded spherical metal nanoparticles, by using equation 6.12. This equation relates the ratio between the heat flow due to the conduction in the medium and the heat flow due to the metal-medium interface to certain parameters of the system, such as the thermal conductivity of the medium, the radius of the nanoparticle and the heat transfer coefficient at the interface between the two materials. This agrees with previous conclusions based on calculations of the Biot number[66].

When the value of the heat transfer coefficient for the bare gold-water interface was used in equation 6.12 and assuming a medium of water, it was estimated that, for these approximations:

- for particles with $R \leq 5$ nm, the heat flow in the system is determined by the water-gold interface,
- while for particles with $R > 5$ nm, the overall heat transfer is dominated by the heat conduction in the medium.

Finding a dependence of the dominant heat flow mechanism on nanosize particles is both surprising and encouraging, as it provides another variable that can be controlled for the targeted applications. It also provides new questions that are addressed in the next two chapters. In the next chapter, the effect of adding an organic-coating to the gold surface in the value of the heat transfer coefficient at the interface gold-water will be studied. The subsequent chapter treats the dependence of the dominant heat transfer mechanism with the size of the nanoparticle.

Chapter 7

Determination of heat transfer coefficient at the organic-coated gold-water interfaces

In the use of gold nanoparticles for biomedical applications, it is essential that the nanoparticles are passivated with an organic layer, that allows them to target the desired tissues and increase the circulation time in the organism. When the nanoparticles are used, either as heat sources or scatterers, the interface between the nanoparticle and the medium may be a limiting factor on the overall heat transfer in a system of embedded gold nanoparticles. In the previous chapter we demonstrated that, for the case of a bare nanoparticle in water, the heat transfer through the interface seems to dominate when the nanoparticle is smaller than 5 nm in radius. When the nanoparticles are coated with an organic layer, the heat diffused through the interface should be altered by this extra barrier.

In this chapter, we will study the effect of different organic coatings on the heat transfer coefficient at the gold-water interface. Firstly, the systems and conditions used or altered from the procedure employed in the previous chapter are presented. Next, the results obtained are linked to the analytical model presented in the previous chapter. These results are then compared with the value of the heat transfer coefficient obtained in the previous chapter and also with other values present in the literature.

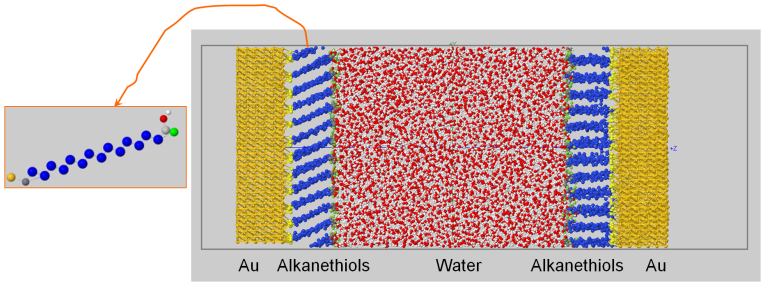

Figure 7.1: Scheme of the system of organic-coated gold slabs separated by a water box and limited by the simulation box in dark grey. On the left, a close up to one of the alkanethiols chain with a carboxylic functional group is also presented.

7.1 Systems and conditions simulated

The simulated slab systems presented in this chapter were composed of two gold slabs separated by a water layer of several different thicknesses. Each gold slab was composed by 2160 gold atoms, distributed over six (1 1 1) atomic planes perpendicular to the z direction and with dimensions of $50 \times 52 \times 14$ Å^3. An assembly of 120 alkanethiols chains, which changed in length and functional groups for specific sets of simulations, was covalently bound to each of the gold surfaces. Each alkanethiol, as shown in figure 7.1, was composed of a sulphur head, followed by a tail of nine or fifteen united atom carbons (that is, each pair of hydrogen atoms was embedded in the corresponding carbon atom) and finished with the functional group. This functional group was either an all-atom carboxylic acid (-COOH) or methyl group (-CH_3). The alkanethiols, each spaced by 5 Å from its neighbours in an hexagonal arrangement, were tilted by $\approx 30°$ with respect to the z axis and were positioned so that each sulphur atom sits in the middle of three gold atoms[107]. Each water box was also built as a lattice of water molecules, where the intermolecular distances were set to mimic the water density of 1000 kg/m^3. The area of each water box, perpendicular to the z axis, was of 47×47 Å^2, while the z dimension changed, accordingly to the thickness of water needed. The slab system was then assembled, along the z direction, by including each component in the same simulation box, as shown in figure 7.1.

The slab conditions were obtained by increasing the z component of the simulation box by approximately 40 Å and by using periodic boundary conditions in three dimensions. The intra- and interatomic interactions between the different atomic species in the system were regulated by the potentials and cut off distances described in section 4.1.1.

The relaxation process was done under NVT conditions, with the slab system coupled to a Berendsen thermostat, with a relaxation time of 0.1 ps, at 300 K, with statistics collected for slab segments approximately 2 Å thick and perpendicular to the z direction.

The adaptation and relaxation of the organic components to the inorganic part was performed with a step-wise relaxation method. Initially, each assembled system was relaxed, for 10 ps, with the sulphur atoms and the water molecules frozen, that is, with constant positions and null velocities. This allowed the relaxation of the alkane chains and functional groups, as well as of the gold slabs. During the following 10 ps, the sulphurs were free to move and adsorb to the gold slab, while the water molecules were still frozen. Finally, every atom in the system was free, allowing the interaction of the alkanethiols with the water. At this stage, consecutives runs of 10 ps were done, until the system's volume, density of the water slabs and weighted mean temperatures for each of the gold slabs, organics (named "Ths" in the following graphs) and water were constant. After a total time t_{rel}, each system was considered to be relaxed.

The average thickness $\langle d_{Wa} \rangle_{rel}$, and density $\langle \rho_{Wa} \rangle_{rel}$ of the water layer were also determined, when each system was stable. The evolution of these parameters with time is shown, as an example, in figure 7.2. The details specific to each system and to their relaxation process are given in table 7.1.

When each system was considered relaxed, non-equilibrium conditions were set for a period of t_{tot}, These conditions used the heat source and sink method, described in sections 4.2.2 and appendix A, with a relaxation time of 0.1 ps, that imposed a heat flux of 7.76×10^9 W m^{-2} . Statistics were collected every 1 ps, for slab segments approximately 2 Å thick and perpendicular to the z direction. Each system was considered to be at steady state after a time t_{tillSS}, by applying the conditions described in section 4.3 to evaluate the temperature rolling averages of the gold slabs calculated with a 20 ps interval. The last 100 ps of simulation time were used to evaluate the statistics of the system at steady state. These statistics allowed the calculation of the average temperatures and average positions of the slab segments. These averaged values were then used to obtain the z positions of the fourth $\langle z_c \rangle$ and fourth to last $\langle z_h \rangle$ gold slab segments and corresponding temperatures $\langle T_c \rangle$ and $\langle T_h \rangle$, needed to determine the value of the heat transfer coefficient, according to the method described in section 4.4. Moreover, the averaged temperature profile of the central water slabs was used to determine the thermal conductivity of the water k_{Wa}. The latter observable was calculated by applying Fourier's law (equation 2.2) to the central water layer with ≈ 10 Å thickness. The

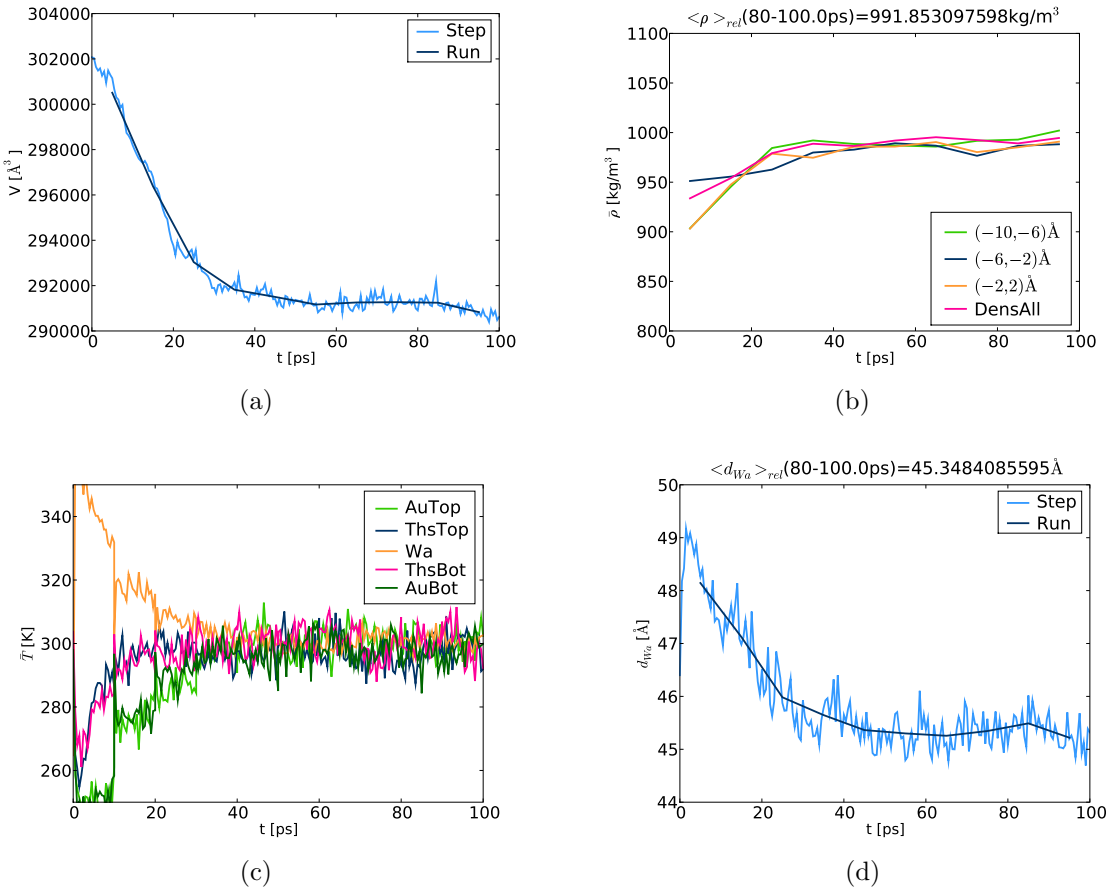

Figure 7.2: (a) System's volume (per time step and at the end of each run), (b) water density, at the end of each run, for several layers (between -10 and -6 Å, -6 and -2 Å and -2 and 2 Å) and for the whole water, (c) weighted mean temperature for the several layers in the system and (d) water slab thickness evolution (per time step and at the end of each run) over time, when the system of two gold slabs, coated with mercaptohexadecanoic acids (S-$(CH_2)_{15}$-COOH), are separated by a water slab approximately 45 Å thick. Images (b) and (d) also present the mean water density and water slab thickness, respectively, for the last 20 ps of simulation. The system is considered to be relaxed when all of these parameters are stable.

average temperature of this central water layer was around 300 K for every system. The values of each of these variables are presented in table 7.1, for all the systems analysed.

Table 7.1: Description of the systems simulated and of the specific conditions used to determined the value of the heat transfer coefficient for the organic-coated gold-water interfaces. During the heat source and sink method, the heat flux imposed was of 7.7643×10^9 W m^{-2} for every simulation. Once steady state conditions were reached, the last 100 ps of simulation were used to collect the statistics that give rise to values of $\langle z_c \rangle$, $\langle T_c \rangle$, $\langle z_h \rangle$, $\langle T_c \rangle$ and k_{Wa}.

Alkanethiols	No. Wa	Relaxation per.			Source sink		$\langle z_c \rangle$	$\langle T_c \rangle$	$\langle z_h \rangle$	$\langle T_h \rangle$	k_{Wa}
		$\langle d_{Wa} \rangle_{rel}$	$\langle \rho_{Wa} \rangle_{rel}$	t_{rel}	t_{tot}	t_{tillSS}					
	molec.	[Å]	[kg/m^3]	[ps]	[ps]	[ps]	[Å]	[K]	[Å]	[K]	[W m^{-1} K^{-1}]
S-$(CH_2)_9$-COOH	2560	≈ 30	≈ 987	110	400	≈ 165	≈ -36	≈ 168	≈ 32	≈ 436	≈ 0.50
	3840	≈ 45	≈ 993	110	350	≈ 124	≈ -43	≈ 151	≈ 41	≈ 443	≈ 0.43
mercaptodecanoic acid	5120	≈ 58	≈ 986	130	650	≈ 190	≈ -49	≈ 143	≈ 46	≈ 461	≈ 0.46
	7680	≈ 90	≈ 989	120	750	≈ 416	≈ -66	≈ 103	≈ 63	≈ 492	≈ 0.44
S-$(CH_2)_{15}$-COOH	2560	≈ 30	≈ 1000	110	500	≈ 170	≈ -42	≈ 163	≈ 40	≈ 429	≈ 0.49
	3840	≈ 45	≈ 992	120	550	≈ 167	≈ -49	≈ 152	≈ 48	≈ 450	≈ 0.43
mercaptohexadecanoic acid	3375	≈ 60	≈ 973	140	650	≈ 190	≈ -58	≈ 136	≈ 54	≈ 463	≈ 0.42
	7680	≈ 90	≈ 988	130	650	≈ 329	≈ -72	≈ 103	≈ 69	≈ 494	≈ 0.49
S-$(CH_2)_9$-CH_3	2560	≈ 32	≈ 994	110	650	≈ 356	≈ -38	≈ 82	≈ 35	≈ 537	≈ 0.38
	3840	≈ 47	≈ 981	110	600	≈ 324	≈ -44	≈ 74	≈ 44	≈ 556	≈ 0.42
mercaptodecane	5120	≈ 59	≈ 989	130	650	≈ 360	≈ -50	≈ 52	≈ 49	≈ 582	≈ 0.42
	7680	≈ 92	≈ 982	130	650	≈ 442	≈ -66	≈ 31	≈ 68	≈ 623	≈ 0.41

7.2 Results and discussion

The average temperature and position values, together with the value of the heat flux were used to estimate a value for the thermal conductivity of water and to calculate the heat transfer coefficient for the interfaces between several organic-coated gold slabs and water, as explained in section 4.4. The results obtained are displayed in table 7.2 and figure 7.3. These heat transfer coefficients, as already pointed out in reference [56], include three or four linked processes:

1. Heat flow from the gold to the sulphur head group.
2. Flow of heat through the alkane chain.
3. Vibrational energy flow from the functional group to the contacting water.
4. And it may also include the flow of heat from the contacting water to the bulk water phase.

Table 7.2: Results obtained from the linear regression on the simulation results for systems of two organic-coated gold slabs separated by a water layer.

Alkanethiol	$U(d) = a \cdot d + b$		$U(d) = \frac{1}{k_{Wa}} \cdot d + \frac{2}{H}$	
	a	b	k_{Wa}	H
	[m K W^{-1}]	[m^2 K W^{-1}]	[W m^{-1} K^{-1}]	[W m^{-2} K^{-1}]
S-$(CH_2)_9$-COOH	2.5828	2.5711×10^{-8}	0.39	7.78×10^7
S-$(CH_2)_{15}$-COOH	2.6373	2.5794×10^{-8}	0.38	7.76×10^7
S-$(CH_2)_9$-CH_3	2.9901	4.8908×10^{-8}	0.33	4.09×10^7

When an organic coating exists between the gold and the water, the value of the heat transfer coefficient reduces from 104.5 MW m^{-2} K^{-1}, for the case of bare gold-water interface, to approximately 78 MW m^{-2} K^{-1}, for the case of hydrophilic alkanethiols or to 41 MW m^{-2} K^{-1} for the alkanethiols with the hydrophobic functional group. This reduction on the heat transfer coefficient with the decrease of hydrophilicity of the functional group is in good agreement with other studies[51, 55, 56, 61]. Experimental results in [56], where planar gold surfaces coated with hydrophobic and hydrophilic alkane chains are used, show values of 50 ± 5 MW m^{-2} K^{-1} for the hydrophobic surface coated with 1-octadecanethiol (C_{18}) and 100 ± 20 MW m^{-2} K^{-1} for the hydrophilic

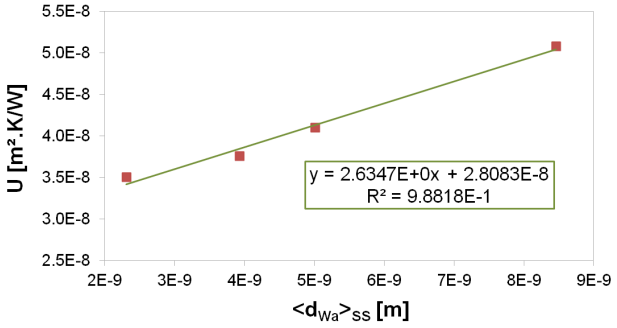

(a)

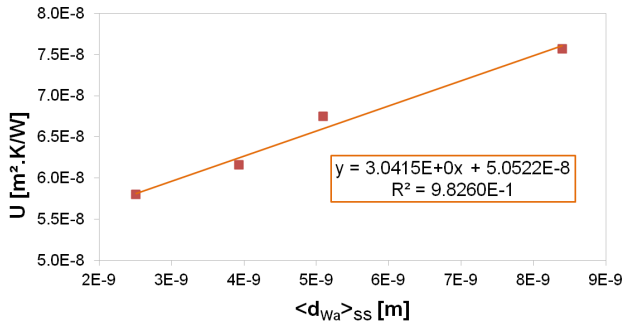

(b)

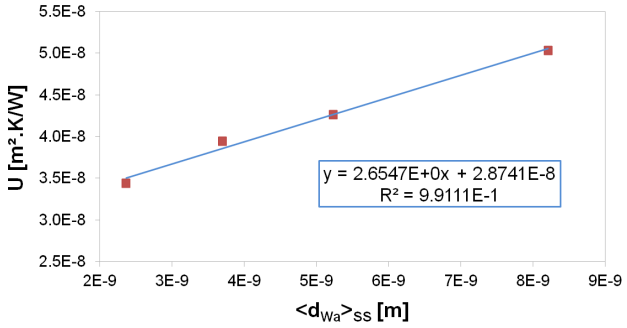

(c)

Figure 7.3: Thermal resistance vs water thickness obtained with the simulations of several systems of two organic-coated gold slabs separated by a water slab. Each trend line and equation shown result from a linear regression fit to the points.

case where the gold is functionalised with 11-mercapto-1-undecanol ($C_{11}OH$). Another experimental study, present in [51], also samples the heat transfer coefficient of different chemical bonding species. Systems of Au/CH_3-C_{11}-Si/Qz present a heat transfer coef-

ficient of 36 MW m^{-1} K^{-2}, while an amine- and bromine-terminated surface (Au/NH_2-C_{11}-Si/Qz and Au/Br-C_{11}-Si/Qz) give values of 39 and 47 MW m^{-1} K^{-2}, respectively. The surface with the strongest bond, present in the system Au/SH-C_{11}-Si/Qz, obtained a rate of heat transfer through the interface of 68 MW m^{-1} K^{-2} Computational work from [61], where the heat transfer coefficients for several SAMs-water planar interfaces were calculated, also verified it to vary from 40 to 140 MW m^{-2} K^{-1} as the hydrophilicity increases. One of the SAMs was an undecanethiol ($S(CH_2)_{10}CH_3$), which had a heat transfer coefficient of 50 MW m^{-2} K^{-1}. This value agrees well with the experimental value (50 ± 5 MW m^{-2} K^{-1}) and is remarkably close to the one determined in this work (41 MW m^{-2} K^{-1}). The differences between the two values determined by computational methods could be related to the absence of a gold layer and the different force fields used in reference [61]. Nevertheless, quantitatively, the values obtained in this work show a very good agreement with the experimental and computational work cited.

When the length of the alkane chain increased by seven carbons, the value of the heat transfer coefficient did not vary considerably. This nonvariation is also in agreement with other studies. Experimental work[55] with embedded gold nanorods coated with PEGs and alkanethiolates acids of different lengths report that the value of the heat transfer coefficient did not change signifcantly with the length of the coating. For instance, nanorods coated with mercaptoundecanoic acid ($CH_3(CH_2)_9COOH$) led to a value of 175 ± 75 MW m^{-2} K^{-1}, while when the alkane chain increased to a mercaptohexadecanoic acid ($CH_3(CH_2)_{14}COOH$) the value reduced to 163 ± 35 MW m^{-2} K^{-1}. Another group[50] also determined experimentally the value of the heat transfer coefficient of alkanethiolated chains of several lengths coated in a thin film of gold. They measured a value of 220 MW m^{-2} K^{-1}, which was alkane length independent. This nonvariation of the heat transfer coefficient with the alkane length should be due to the very fast energy transport along the alkane chain, which was measured to be 0.95 km s^{-1}.

Using our values of the heat transfer coefficient for the organic-coated gold-water interfaces in equation 6.12, we can estimate the particle size at which there is a transition between the two heat transfer mechanisms. Therefore, the transition of the heat flow dominated by the interface to the heat propagation limited by the conduction in the medium happens for the nanoparticle radius of 7.5 nm for the hydrophobic organic coating and 14.2 nm for the gold coated with hydrophilic alkanethiols.

As already discussed in section 6.3.2, the value of the thermal conductivity of water is smaller than experimental and computational results. Nevertheless, it is in good

agreement with the values obtained from the individual slab systems, stated in table 7.1.

Finally, the variables determined here do not present an error associated, due to reasons already explained in section 6.3.2.

7.3 Summary

In this chapter, we extend the work done in the previous chapter by introducing an organic coating between the gold and the water. We then use computational methods to determine the value of the heat transfer coefficient at different types of interfaces.

The introduction of an organic layer reduces the value of the heat transfer coefficient (104.5 MW m^{-2} K^{-1}, for the bare gold-water interface) by $\approx$ 25% for the case of hydrophilic head group (78 MW m^{-2} K^{-1}), and by $\approx$ 60% for the case of the hydrophobic head group (41 MW m^{-2} K^{-1}). Consequently, the transition between the heat transfer dominated by the interface to the heat flow limited by the conduction in the medium happens for nanoparticle radii of 7 and 14 nm, respectively. As discussed, this reduction is in good agreement with other experimental and computational work. Furthermore, the increase of the chain length of the organic coating does not change significantly the value of the heat transfer coefficient.

Chapter 8

Studies on heat release in a spherical geometry

One of the main goals of this thesis is to study the thermal variations when hot gold nanoparticles are embedded in a colder medium (water or an organic liquid, for instance). The previous chapters studied systems in a slab configuration and focused on the effect of the interface between the gold and the water on the dominant heat transfer mechanism. It was shown in chapter 6 that the size of the nanoparticle can influence the overall dominant heat flow. More specifically, for the case of bare gold and water, nanoparticles with radius smaller than 5 nm should have a heat flow limited by the interface gold-water, while for bigger nanoparticles the overall heat transfer should be dominated by the conduction in water. This heat flow transition is investigated now by computational methods, using systems of spherical gold nanoparticles embedded in water. In particular, simulations with gold nanoparticles of several sizes embedded in water are performed. In the second part of this chapter, the effect of the temperature of the nanoparticle in the overall heat flow is investigated. For this study one spherical nanoparticle is used, and its temperature is varied. In both studies, non-equilibrium molecular dynamics simulations are performed.

This chapter will start with the systems and conditions used to study the effect of the nanoparticle size on the heat propagation. For the analysis of the data, the analytical solution of the water temperature profile in such spherical systems, as described in section 6.2.1, is used. The temperature profiles, temperature differences at the interface and within the water are discussed. In the second part of this chapter, the simulation conditions used to study the effect of the gold nanoparticle temperature on the overall

heat transfer are presented. The main results and comments on the temperature profiles at the gold-water interface and within the water are also explained.

8.1 Dependence of heat flow with nanoparticle size

As previously concluded in section 6.3.2, the calculated value of the heat transfer coefficient for the bare gold-water interface led to interesting predictions. When the radius of the nanoparticle is greater than 5 nm, a transition between the heat flow dominated by the bare gold-water interface, to the heat transfer limited by the conduction in the medium is expected.

This transition is tested here by employing non-equilibrium methods, already described in section 4.2, in several systems of gold nanoparticles embedded in water. The main difference between the several systems is the nanoparticle's size. The radius R_{NP} of the nanoparticle ranges from approximately 1 to around 7 nm. To minimise the number of degrees of freedom in the systems tested, the temperature difference imposed in each system is constant and is controlled by the two thermostats method. Each system is simulated until a steady state regime is reached, identified by respecting the conditions described in section 4.3. At this stage, the temperature profiles can be analysed and the value of the heat transfer coefficient H associated with each nanoparticle is estimated.

In the next few sections, the systems under study and the simulations conditions used are explained, as well as the results obtained. The discussion of results is linked to the conclusions previously drawn in section 6.3.2 and also gives new insights on the possible dependence on the value of the heat transfer coefficient.

8.1.1 Systems and conditions simulated

All the simulated systems used gold nanoparticles, approaching a spherical geometry, embedded in water boxes. Most of the nanoparticles resulted from the annealing process presented in chapter 5. The only exception was for one of the smallest nanoparticles, where a perfect gold octahedron was constructed. The water box was initialised as a water cube, with side L approximately 10 nm. In this cube, 823875 water molecules were arranged in a simple cubic lattice, so as to reproduce the bulk water density of 1 kg m^{-3}. This water box was then relaxed for 1 ps, under NVT conditions, where the temperature of the system was controlled to 300 K by a Nosé-Hoover thermostat with a

relaxation time of 0.1 ps. The water force field used was described in section 4.1.1. Due to the high number of water molecules, this method was not computationally efficient. Therefore, the resulting configuration of this water box was cut to build smaller water boxes needed for the several simulated systems. Each of the smaller water boxes was large enough to allow, once the system was assembled and relaxed, a distance between the nanoparticle surface and the thermostated water of approximately 30 Å (refer to section 4.3 to the scheme of the system's configuration). The only exception was for the case of the nanoparticle with a diameter approximately 4 nm. As this system was used to test the implementation of the two thermostats method for spherical systems, a cubic lattice water box was used from the beginning of the relaxation period.

Each system with an embedded nanoparticle, periodic in the three dimensions, was then relaxed under NPT conditions, coupled to a Nosé-Hoover thermostat and barostat, with fluctuation times of 0.1 and 1 ps respectively, at 310 K and 1 atm. The gold-gold, water-gold and water-water interatomic potentials and the cut off distances used were described in section 4.1.1.

All systems were considered to be relaxed once the system's volume, density of the water coronae and weighted mean temperatures for each component in the system were stable. As an example, the evolution of these variables with time is shown, for one of the spherical systems, in figure 8.1. The average density of the water layer $\langle \rho_{Wa} \rangle$ was also determined when each system was stable. The details specific to each system and to their relaxation process are given in table 8.1.

After each system was relaxed, the non-equilibrium conditions were imposed, with statistics being collected every 0.5-1 ps, for coronae with 2 Å thickness. For each system, the two thermostats method, described in section 4.2.1 and appendix A, was applied for a time t_{tot}, where the nanoparticle temperature was set to 600 K, while the thermostated water was set to 310 K, with a 0.1 ps fluctuation time for both thermostats. Under these non-equilibrium conditions, the temperature rolling averages of the non-thermostated water were calculated with a time interval of 20 ps. Critically examining this temperature profile according to the conditions present in section 4.3, each system was considered to be under a steady state regime after a time t_{tillSS}. Beyond this time mark, the last Δt_{atSS} picoseconds of statistics were processed to determine the average temperatures and coronae radii for the simulated system. With these averaged values, the method described in section 4.5 was used to obtain the maximum radius r_h, and corresponding temperature T_h, where only gold atoms are present and the smaller corona radius r_c where the thermostated water, at temperature T_c, starts. The heat

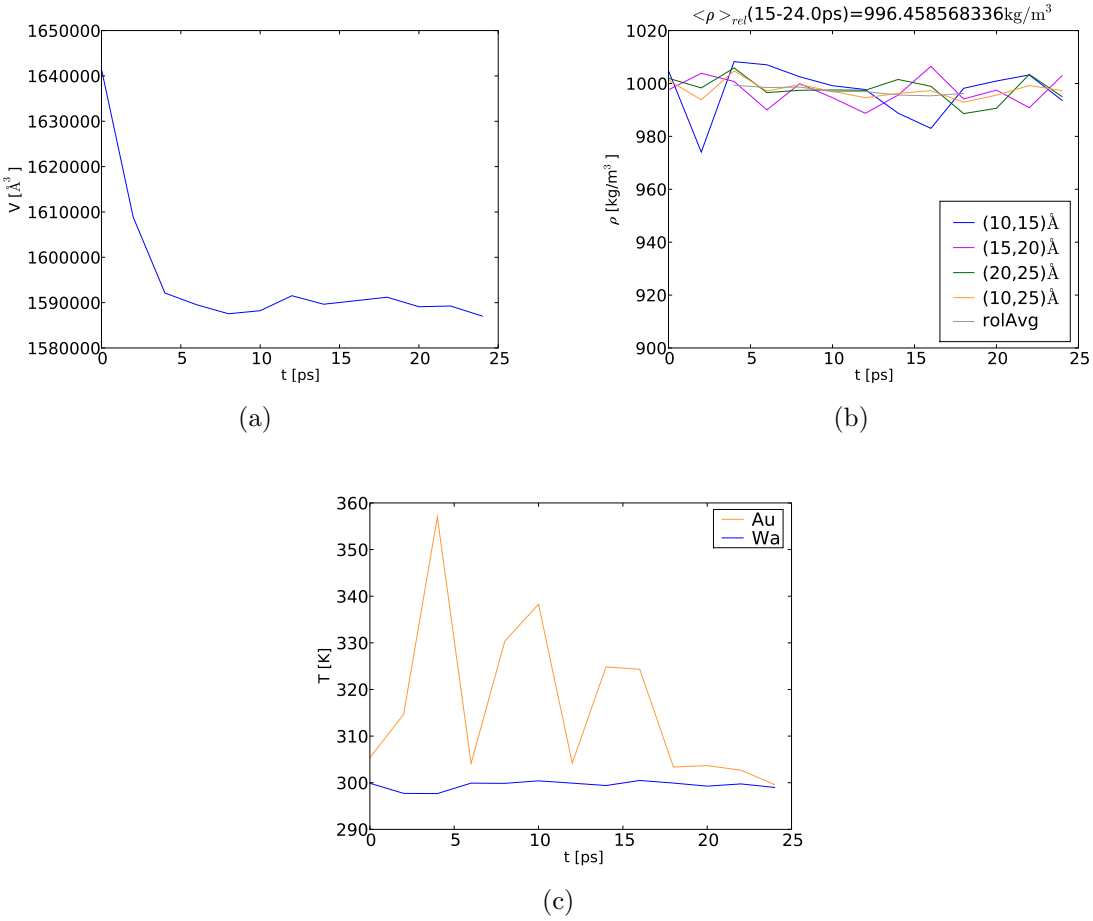

Figure 8.1: (a) System's volume, (b) water density for several water coronae (with radius from 10 to 15 Å, 15 to 20 Å, 20 to 25 Å and from 10 to 25 Å) and (c) weighted mean temperature evolution for each component over time, for a system of a gold nanoparticle of approximately 4 nm in diameter embedded in a water box of side approximately 11.6 nm. The system is considered to be relaxed when all these parameters are stable.

flow Q was determined from the fit of equation 4.44 to the temperature profile of the non-thermostated water and using the experimental value of the thermal conductivity of water presented in appendix B. Finally, using the values of these five parameters, the value of the heat transfer coefficient H was also obtained, as explained in section 4.5. In table 8.1, the values of each of these variables are presented, for each of the systems analysed.

Table 8.1: Description of the spherical systems simulated and of the specific conditions used to determined the transition of the dominant heat transfer mechanism with the nanoparticle size.

R_{NP}	No. Au	No. Wa	Relax. period			Two Therm. period			Heat flow	$\langle r_h \rangle$	$\langle T_h \rangle$	$\langle r_c \rangle$	$\langle T_c \rangle$
	atoms	molec.	t_{rel}	L	$\langle \rho_{Wa} \rangle_{rel}$	t_{tot}	t_{tillSS}	Δt_{atSS}					
[nm]			[ps]	[Å]	[kg m^{-3}]	[ps]	[ps]	[ps]	[W]	[Å]	[K]	[Å]	[K]
≈ 1	231 (oct.)	26928	24	93.34	≈ 996	150	≈ 33	100	4.15×10^{-7}	5	≈ 593	47	≈ 311
≈ 1	256	26980	16	93.37	≈ 995	150	≈ 39	110	4.77×10^{-7}	5	≈ 598	45	≈ 312
≈ 1.3	500	31856	44	98.85	≈ 992	150	≈ 29	100	7.51×10^{-7}	7	≈ 600	49	≈ 312
≈ 2	2048	52099	24	116.64	≈ 996	215	≈ 60	100	1.58×10^{-6}	11	≈ 630	57	≈ 315
≈ 3.5	10976	80882	40	137.78	≈ 992	250	≈ 99	100	4.14×10^{-6}	27	≈ 588	67	≈ 319
≈ 5	32000	157757	21	174.19	≈ 989	240	≈ 123	100	6.83×10^{-6}	43	≈ 558	87	≈ 323
≈ 7	84895	217472	40	199.81	≈ 989	280	≈ 139	100	1.27×10^{-5}	65	≈ 524	99	≈ 336

8.1.2 Results and discussion

One of the aims of this study is to investigate if the dominant heat transfer mechanism changes as the size of the nanoparticle increases. Therefore, the temperature difference at the gold-water interface ΔT_i is compared to the temperature drop due to the conduction in the non-thermostated water ΔT_{Wa}. As can be verified in figure 8.2 and table 8.2, the temperature drop at the interface decreases, while the temperature difference in the non-thermostated water increases, as the size of the nanoparticle increases. In particular, when the nanoparticle increases from a radius of approximately 1 to 7 nm, the temperature drop at the interface decreases by 100 K, while in the non-thermostated water is increased only by 30 K. Therefore, for the nanoparticle sizes of 1-3 nm in radius, it is clear that the interface is the limiting factor on the overall heat transfer, as the temperature change at the interface is 3 to 7 times bigger than the temperature drop in the water. As the nanoparticle reaches a radius of 5 nm, the interface becomes less dominant and when the radius is 7 nm, the differences in temperature at the interface and at the non-thermostated water are of comparable magnitudes, as shown by ratio $\frac{\Delta T_i}{\Delta T_{Wa}}$ in table 8.2.

Table 8.2: Temperature difference at the interface ΔT_i, the temperature drop in the medium of non-thermostated water ΔT_{Wa} and the ratio of these two quantities, for each of the nanoparticle sizes simulated.

R_{NP} [nm]	ΔT_i [K]	ΔT_{Wa} [K]	$\frac{\Delta T_i}{\Delta T_{Wa}}$	H [MW m^{-2} K^{-1}]	τ [ps]
≈ 1 (octa.)	≈ 195	≈ 30	6.5	≈ 733	1.34
≈ 1	≈ 205	≈ 30	6.8	≈ 891	1.06
≈ 1.3	≈ 180	≈ 35	5.1	≈ 753	1.60
≈ 2	≈ 145	≈ 45	3.2	≈ 665	2.85
≈ 3.5	≈ 130	≈ 50	2.6	≈ 320	9.98
≈ 5	≈ 100	≈ 50	2.0	≈ 235	19.45
≈ 7	≈ 90	≈ 60	1.5	≈ 247	24.64

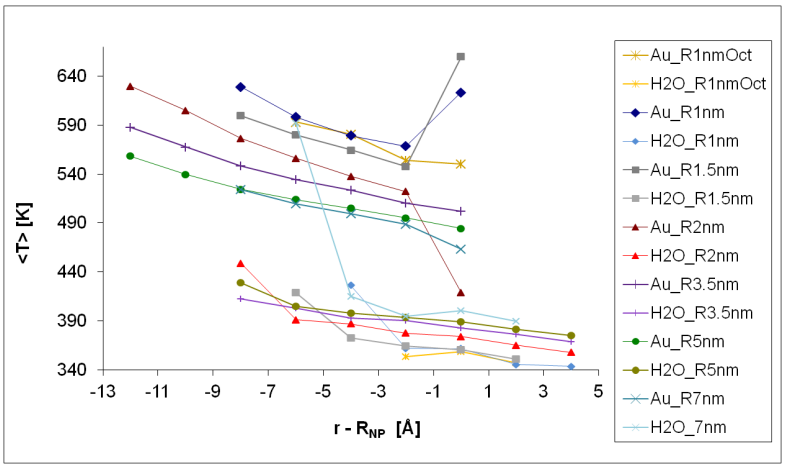

(a)

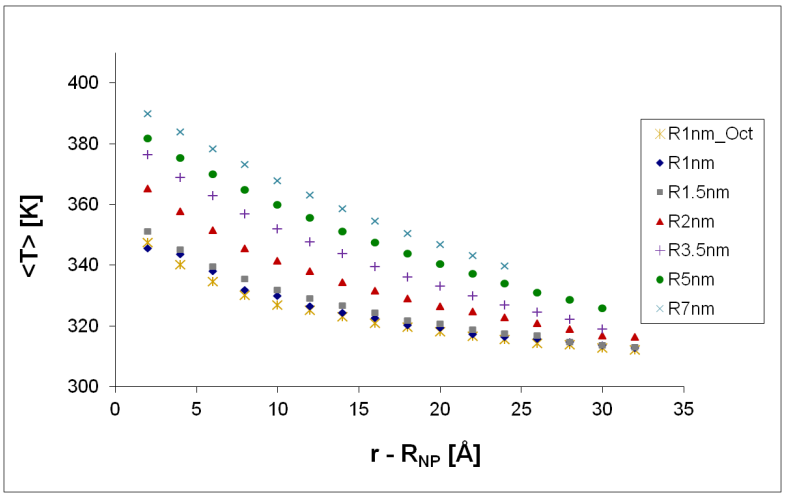

(b)

Figure 8.2: (a) Temperature drop at the gold-water interface and (b) temperature profile at the non-thermostated water for hot nanoparticles of different sizes embedded in cold water. The distance $r - R_{NP}$ represents the corona radius shifted by the radius of the nanoparticle. Note that because of the surface roughness, the coronae between positions -8 and 0 Å contain both gold and water.

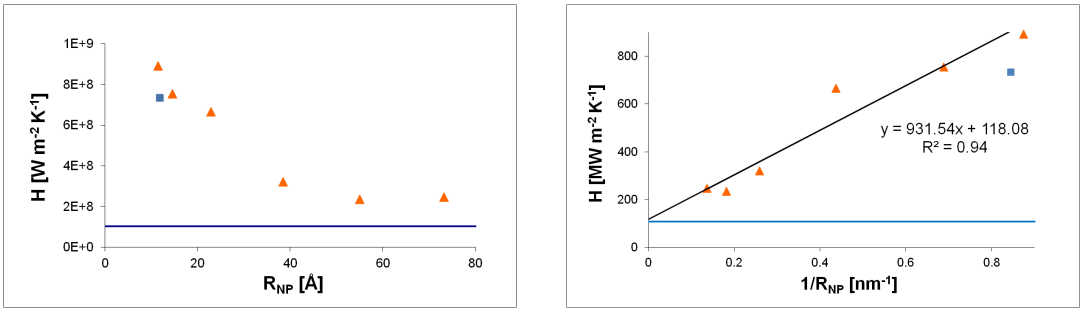

(a) (b)

Figure 8.3: (a) Heat transfer coefficient for different sizes of the gold nanoparticles. The triangles refer to the nanoparticles computationally created, while the square refers to a perfect octahedron gold nanoparticle. The blue line is the heat transfer coefficient value obtained with the slab configuration in section 6.3.2. (b) Heat transfer coefficient is plotted versus the inverse nanoparticle radius, so to extrapolate the value of the heat transfer coefficient for a flat surface.

The value of the heat transfer coefficient at the gold-water interface was calculated for the different sizes of gold nanoparticles. The values, presented in table 8.2 and plotted in figure 8.3, show a dependence of the heat transfer coefficient with the nanoparticle size, in agreement with other computational studies consisting of hydrated small hydrocarbon droplets[66] and ZnO particles embedded in tetradecane[66].

For nanoparticles with radii smaller than 5 nm, the value of the heat transfer coefficient increases from 5 to 9 times with respect to the value obtained with the slab configuration, as the nanoparticle size decreases. Our results are consistent with available experimental data. Experimental observations[49] done on nanoparticles of several averaged sizes (4, 15, 26, 40 and 50 nm in diameter) suspended in aqueous solution and examined by pump-probe spectroscopy measured a variation of the relaxation time from almost 400 ps, for the 50 nm diameter particle, to 10 ps, for the particles with 4 nm in diameter. These experimental results corroborate our computational ones, as an increase on the heat transferred through the interface as the nanoparticle size decreases, led to a smaller interfacial relaxation time τ, shown in table 8.2. These values of τ were obtained by using each nanoparticle radius and corresponding heat transfer coefficient in equation 6.8. The results from experiment also suggest that, for the smallest nanoparticle, the relaxation time associated with the heat dissipated from the gold to the water is comparable to the time scale for the electron-phonon coupling (a few picoseconds), which is also in line with our results.

Due to the irregular surface structure of these nanoparticles, shown in section 5.3,

it is difficult to determine if this increase on the value of the heat transfer coefficient is caused by the decreasing size of the nanoparticle or by changes in the surface roughness. For this reason, a system containing an embedded perfect gold octahedron with approximately 1 nm radius was assembled. This perfect nanoparticle, with a surface that presented only (1 1 1) planes, was created with the "cluster coordinates generator"[108]. The value of the heat transfer coefficient for this perfect particle was found to be smaller than the one for the annealed nanoparticle with similar radius. One of the possible explanations to this reduction could be due to a smaller surface contact area between the gold and the water for the octahedron particle. Results obtained with the "solvent accessible surface area" tool from VMD do not support this hypothesis, as the annealed particle measured a contact area (2224 $Å^2$) similar to the octahedron particle (2228 $Å^2$). The second interpretation of this result, could be due to the difference in the heat propagation through the edges and the surface planes present in the nanoparticle. As the number of edges is smaller and the area of each surface plane is larger in this perfect particle than in the annealed particle (that is, the roughness decreases), this lead us to conclude that heat propagates slower through the surface than through the edges. This conclusion does not seem to agree with the work done by Little[109], where he analytically demonstrated that an increase in the microscopic roughness (that is, when the surface roughness is comparable to the phonon wavelength) reduced the heat flow across an interface. The conflict between the results by Little and our own is only apparent, though. Little's conclusion does not apply to our systems, as in our case the surface roughness of the nanoparticles is smaller than the phonon wavelength. Nevertheless, although only two different surfaces were tested for this nanoparticle size, the value of the heat transfer coefficient is still at least seven times bigger than for a flat surface. Hence, in spite of the fact that the surface configuration seems to affect the value of the heat transfer coefficient, the size of the nanoparticle is a main factor on the change of the heat transfer coefficient.

When the nanoparticle radius is bigger than 5 nm, the heat transfer coefficient calculated in this work approaches the one determined for a flat surface in section 6.3.2. For the two nanoparticles simulated, the value of the heat transfer coefficient is twice the value for the flat surface.

As is verified in figure 8.3, the heat transfer coefficient varies considerably with the nanoparticle size. Extrapolating this variable to an infinite radius equivalent to a slab system, the heat transfer coefficient has the value of 118 MW m^{-2} K^{-1} (figure 8.3(b)), which agrees with the computational value obtained in section 6.3.2

of 104.5 MW m^{-2} K^{-1} and the experimental value from reference [105] of 105 $\pm$ 15 MW m^{-2} K^{-1}. As the size of the nanoparticle decreases, the heat transfer coefficient increases from 250 MW m^{-2} K^{-1}, for the particle with 7 nm radius, to 890 MW m^{-2} K^{-1} for the smaller nanoparticle with 1 nm in radius. Although of the same order of magnitude, our values for the smaller nanoparticles are bigger than the experimental results obtained with citrate stabilised Pt particles[53] of 10 nm diameter (130 MW m^{-2} K^{-1}) and AuPd nanoparticles of 4 nm in diameter and coated with different organic components[54] (145$\pm$55 MW m^{-2} K^{-1} and 250$\pm$90 MW m^{-2} K^{-1}). This difference could be due to the fact that the experimental nanoparticles have an organic coating, which should decrease the heat transferred through the interface. For bigger particles, as is the case of organic-coated Au-core/AuPd-shell nanoparticles with a diameter of 20 nm[54], the experimental value of 230$\pm$50 MW m^{-2} K^{-1} is similar to our computational value of 235-250 MW m^{-2} K^{-1} obtained for the bigger nanoparticles. Furthermore, these experimental results lead the authors to conclude that the heat transfer coefficient is insensitive to the nanoparticle coating and diameter. In contrast, this variation of the heat transfer coefficient with the particle size has been pointed out by Lervik *et al.*[66] and Hu *et al.*[64]. For the first case, the dependence of the heat transfer coefficient with nanoparticle size was studied, by NEMD simulations, in systems of alkane nanodroplets of diameters between 2 and 12 nm embedded in water. Their results showed a strong reduction of the heat transfer coefficient from 250 to 90 MW m^{-2} K^{-1} as the size of the nanodroplet increases[66]. As for Hu *et al.*, ZnO particles, with radii between 10 and 30 Å were embedded in tetradecane and heated up with a extremely high heat flux, also under non-equilibrium conditions. Their calculated heat transfer coefficients[64] decreased from 35-40 MW m^{-2} K^{-1} for the smaller particles to 6-12 MW m^{-2} K^{-1} for the bigger nanoparticles. Regarding the dependence of the heat transfer coefficient with the size of the nanoparticle, and as already explained in these two references, this can be due to a surface tension effect. The surface tension and solid free energy increases with the radius of the nanoparticle, which leads to a stiffer interface and, therefore, a lower heat transfer. Another explanation to this increase on the heat transfer coefficient as the nanoparticle size decreases could be the variation of the water density surrounding the nanoparticle. As shown in figure 8.4, the density of water molecules around the nanoparticle increases as its size decreases, an effect also observed by others[75]. This could be due to the lower coordination number of the gold atoms close to the surface, which allow a bigger interaction area between the gold atoms and the water. We propose that the increase in the number of water molecules per unit area of the

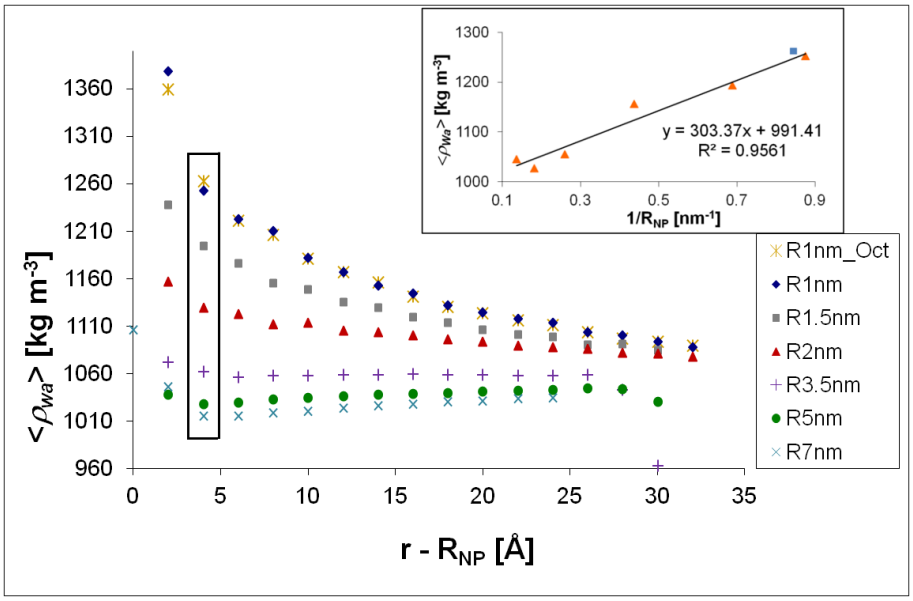

Figure 8.4: Averaged mass density profile, at steady state, for the non-thermostated water embedding the hot nanoparticles of different radii. The distance $r - R_{NP}$ represents the corona radius shifted by the radius of the nanoparticle. In the inset, the mass density for the second corona of non-thermostated water (radius of 75 Å), highlighted in the main graph by the rectangle, is plotted versus the inverse of the nanoparticle radius. The orange triangles refer to the nanoparticles computationally created, while the blue square refers to a perfect octahedron gold nanoparticle.

gold surface increases the interaction between the water and the gold and is responsible for the increase in the heat transfer coefficients as the nanoparticle radius decreases.

As pointed out, the experimental results do not seem to verify the dependence of the heat transfer coefficient with the nanoparticle size, a dependence which was found in this work and other computational studies. The reason could be because the organic coating used in the experimental tests was not the same for every nanoparticle, besides the fact that the smaller and bigger nanoparticles differed in composition. Also, the challenges involved on the experimental procedures are still too great to allow results with small uncertainty and comparable conclusions.

In the next section, the influence of the nanoparticle temperature on the heat transfer coefficient will be investigated.

8.2 Dependence of heat flow with the temperature of the nanoparticle

As the results obtained in the previous section confirmed, there is a dependence of the heat transfer coefficient at the interface with the size of the nanoparticle. This raises questions to a possible dependence of the heat transfer coefficient with other parameters, such as the temperature difference imposed at the interface. Besides this information, the study of the temperature profile of systems of hydrated gold nanoparticles set to different temperatures also provides indications on the effects of the use of different laser fluences in media impregnated with radiation absorbers.

In this section, the system of a spherical gold nanoparticle with a diameter of approximately 4 nm is used to explore the relation between the heat transfer coefficient and the nanoparticle temperature. The system conditions used are similar to the ones described in section 8.1.1 for the nanoparticle with 2048 atoms, with the exception of the variation of the temperature $\langle T_h \rangle$ associated to the nanoparticle's thermostat. The maximum temperature simulated was of 600 K, as higher temperatures made the nanoparticle decompose. The changes in these conditions and their implications in the heat flow Q, heat transfer coefficient H and remaining variables are presented in table 8.3. Although peculiar, the decomposition of the nanoparticle at high temperatures was already observed in computational work done in reference [65]. In this reference, gold nanoparticles solvated in octane started to disintegrate when temperatures higher than 1200 K were reached. The reason why our particles disintegrate at lower temperatures could be due to the difference in the potentials used.

Table 8.3: Description of the specific conditions applied to the spherical system of a gold nanoparticle of radius approximately 2 nm embedded in a water box. The two thermostats method was used to change the temperature of the nanoparticle. This allowed to determine the dependence of the heat transfer coefficient with the temperature difference imposed in the system.

$\langle T_h \rangle$ [K]	t_{tot} [ps]	Δt_{tillSS} [ps]	t_{atSS} [ps]	Heat flow [W]	$\langle r_h \rangle$ [Å]	$\langle T_h \rangle$ [K]	$\langle r_c \rangle$ [Å]	$\langle T_c \rangle$ [K]	H [MW m^{-2} K^{-1}]	ΔT_i [K]	ΔT_{Wa} [K]	$\frac{\Delta T_i}{\Delta T_{Wa}}$
400	250	≈ 109.5	100	4.61×10^{-7}		≈ 398		≈ 311	≈ 439	≈ 50	≈ 15	3.3
450	250	≈ 67.5	100	7.60×10^{-7}	13	≈ 452		≈ 312	≈ 459	≈ 80	≈ 20	4.0
500	250	≈ 85.5	100	1.21×10^{-6}		≈ 503	57	≈ 313	≈ 627	≈ 100	≈ 30	3.3
550	250	≈ 96.5	100	1.51×10^{-6}		≈ 552		≈ 314	≈ 624	≈ 125	≈ 40	3.1
600	215	≈ 60.5	100	1.58×10^{-6}	11	≈ 630		≈ 315	≈ 665	≈ 150	≈ 50	3.0

8.2.1 Results and discussion

To study the dependence of the heat transfer coefficient on the nanoparticle temperature, we start by analysing the temperature drop at the gold-water interface and within the non-thermostated water (figure 8.5). As expected, both temperature drops increase with the increase of the nanoparticle's temperature. But contrary to the case where the size of the nanoparticle changed, the ratio between the two temperature drops is constant when the temperature of the nanoparticle increases. Therefore, there is no change on the dominant heat transfer mechanism.

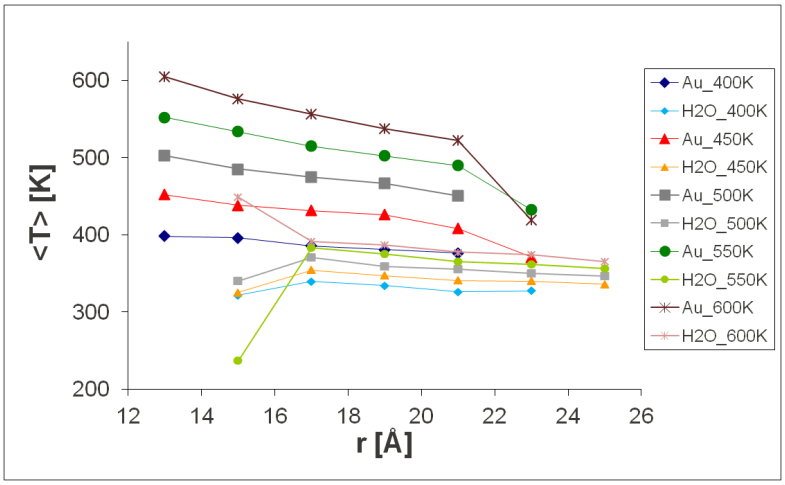

(a)

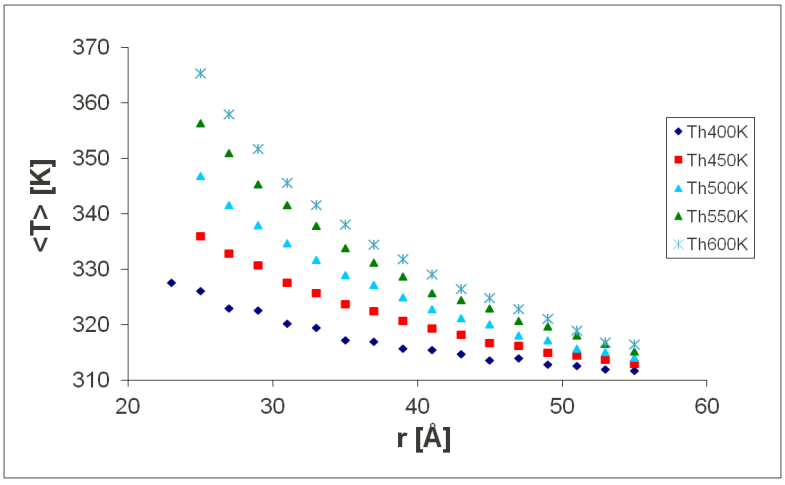

(b)

Figure 8.5: (a) Temperature profile at the gold-water interface and (b) temperature drop at the non-thermostated water for the nanoparticle (diameter $\approx$ 4 nm) set to different temperatures embedded in cold water.

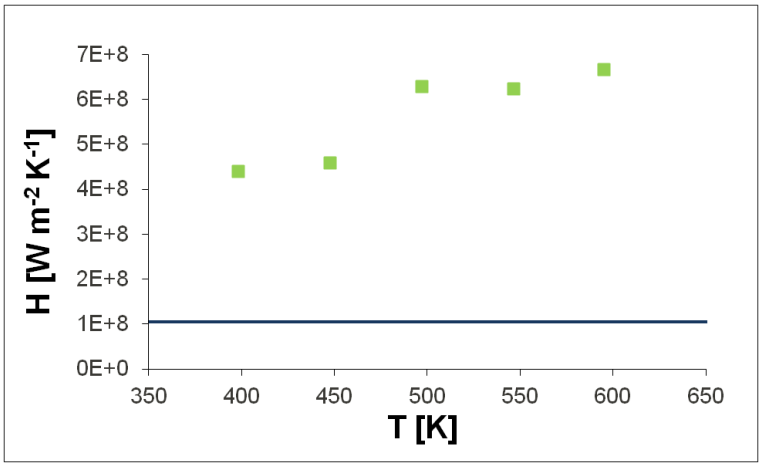

Figure 8.6: Heat transfer coefficient for different temperatures of the gold nanoparticles of diameter ≈ 4 nm. The blue line is the heat transfer coefficient value obtained with the slab configuration.

The heat transfer coefficient at the gold-water interface as the temperature of the gold nanoparticle changes was calculated. The values, listed in table 8.3 and plotted in figure 8.6, show an increase of the heat transfer coefficient as the nanoparticle's temperature increases. For an increase in temperature of 1.5 times (equivalent to an increase of 200 K), the heat transfer coefficient also increases by an equivalent factor.

On the other hand, the mass density of the non-thermostated water, plotted in figure 8.7, shows a decrease on the water density surrounding the nanoparticle as the temperature increases. In line with the reasoning from the previous section, this should mean a decrease of the heat transfer coefficient with the increase of the nanoparticle temperature. As pointed out, this is not the case here and the explanation for these contradictory results is still not known. One factor considered was the change on the thermal conductivity of the water with the temperature[1]. According to reference [110], the thermal conductivity of water increases non-linearly with the temperature, reaching a plateau around 0.7 W m^{-1} K for temperatures higher than 360 K. Hence, one could reasonably assume that this increase of the thermal conductivity contributes to an enhanced heat flow through the interface, even when the density of the water surrounding the nanoparticle decreased. However, the change in temperature profile resulting from the deviation of the thermal conductivity suggest that this effect is not significant

[1]It is worth stating that the determination of the heat transfer coefficient presented in this chapter used the constant value of the thermal conductivity of the water at room temperature, stated in appendix B.

enough to justify the variation of the heat transfer coefficient observed. In addition, this increase of the heat transfer coefficient with the nanoparticle's temperature also contradicts the computational results from references [62], [63] and [65]. In reference [65], gold nanoparticles (radius of 1.3 nm) embedded in octane were heated up to temperatures ranging from 500 K to 1200 K, and the value of the heat transfer coefficient calculated reduced from 100 to 50 MW m^{-2} K^{-1}. When similar simulations were performed in water, the heat transfer coefficient varied from 170 to 150 MW m^{-2} K^{-1}, as the nanoparticle's temperature changed from $\approx$ 570 K to $\approx$ 730 K. As for references [62] and [63], Luo *et al.* used equilibrium and non-equilibrium molecular dynamics in Au-SAM-Au junctions to determine the thermal conductance at the Au-SAM interface, for mean temperatures ranging from 50 to 400 K. They verified an increase of the thermal conductance with the increase of the temperature, until a plateau is reached around 150-250 K. The justification provided for this plateau is related with the populations of vibration modes (phonons). The authors verified an increase on the low frequency modes in both components as the temperature increases. Simultaneously, only the organic components presented an increase on the intermediate frequency modes. This latter anharmonicity depressed any further increase on the thermal conductance. In our case, as the system was of gold nanoparticles embedded in water, it is credible to expect that the populations of vibration modes in a gold nanoparticle will be different than on the slab system, and likely to expand for the intermediate frequency range. Taking this assumption into account, the same line of reasoning as in Luo *et al.* can be used to justify the increase of the heat transfer coefficient at the gold-water interface with the increase of the nanoparticle's temperature. That is, it is plausible to expect that, for the temperature range studied, the populations of vibration modes of the gold and the water match and grow with the temperature, leading to an increase on the heat transfer through phonon-phonon interaction.

8.3 Summary

In this chapter, we explore the systems of hot gold nanoparticles in water by non-equilibrium molecular dynamics. As a first study, we investigate the effect of the nanoparticle size in the temperature profile and heat propagation in this type of systems. We verify that, as the radius of the nanoparticle increases from 1 to 7 nm, the heat transfer through the interface stops being the dominant heat transfer mechanism,

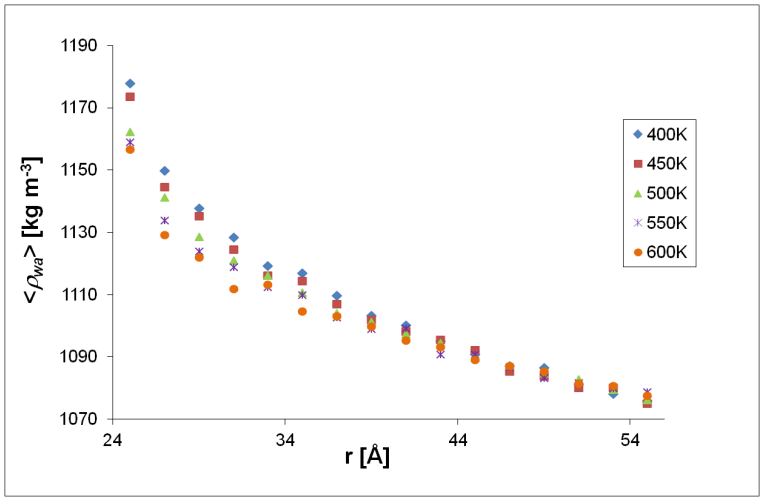

Figure 8.7: Averaged mass density profile, at steady state, for the non-thermostated water embedding the hot nanoparticle (diameter $\approx$ 4 nm) set to different temperatures.

as predicted from the results shown in chapter 6. In fact, the temperature drop at the interface reaches similar values to the temperature difference within the water when the nanoparticle radius is around 5-7 nm. This lead us to conclude that, although for smaller nanoparticles the heat flow in the system is limited by the interface, for nanoparticle sizes of 5-7 nm, the rate of heat transfer through the interface approaches the magnitude of the rate of the heat propagated in the water due to conduction.

Our results also show a dependence on the value of the heat transfer coefficient at the bare gold-water interface with the size of the nanoparticle. For the nanoparticles with radii smaller than 5 nm, the value of the heat transfer coefficient is considerably higher than for the nanoparticles with radii of 5-7 nm. Extrapolating its value for a particle with an infinite radius, we obtain a value very close to the one determined in chapter 6 for the slab system. We also investigate if this strong dependence of the heat transfer coefficient as the size of the nanoparticle decreases could be due mainly to surface effects. Our results show that, although the surface of the nanoparticle has a considerable effect on the heat transfer through the interface, the size of the nanoparticle is the main contributor for the variation of the heat transfer coefficient.

In the second part of this chapter, we use the nanoparticle with radius of approximately 2 nm to study the effect of the nanoparticle temperature on the heat transfer coefficient at the interface and on the temperature profile for the case of hydrated gold nanoparticles. Our computational results demonstrate that the temperature drop at the gold-water interface and within the water increases with the same rate as the tem-

perature of the nanoparticle. This leads us to conclude that there is no change on the dominant heat transfer mechanism as the nanoparticle temperature varies. As for the heat transfer coefficient, we detect an increase of its value proportional to the increase of the nanoparticle temperature.

Chapter 9

Conclusions

The aims of this body of work was to study the possible use of gold nanoparticles as heat sources for biomedical applications. To further understand the use of the mentioned gold nanostructures, computational methods allied to analytical calculations were used. In the next few paragraphs, the main conclusions drawn during the duration of this thesis are presented.

To start this thesis, we decided to computationally create gold nanoparticles, by mimicking the annealing process used experimentally. This annealing process involved rapidly heating the gold nanostructure until it melted, followed by a slower cooling period. Each nanoparticle was also characterised by assessing the local degree of order, at the atomic level, with respect to a perfect FCC structure and by calculating an average value of the nanoparticle's local order parameter. In chapter 5, the annealing and characterisation results of the particles with radii ranging from approximately 1 to 7 nm were presented. Our results showed that a non-amorphous core was obtained when the cooling period was around a few nanoseconds. Likewise, 0.5 K/ps was the fastest cooling rate that still allowed crystallisation. Slower cooling rates and longer cooling periods allowed the creation of nanoparticles with a higher degree of order, as demonstrated by the values of the local order parameter. None of the created particles was defect free, as each nanoparticle presented twin boundaries. For some of the particles smaller than 3 nm in radius, the twin boundaries even met at a two dimensional pentagon shape, composed by clusters of fifteen faces. For the nanoparticle of around 5 nm in radius, regions of HCP structure were identified in the middle of the FCC crystal structure.

In chapter 6, we analysed the system of gold nanospheres embedded in water by

analytical methods. We started by analytically solving the heat conduction equation for the simple system of a metallic nanosphere embedded in water. We determined the heat flow for the extreme cases of the heat transfer being dominated by the conduction in water and by the heat transfer at the particle-water interface. The ratio of these two heat flows was linearly dependent on the thermal conductivity of the medium and inversely proportional to the radius of the nanoparticle and the heat transfer coefficient at the interface between the two materials. This led us to investigate the value of the heat transfer coefficient for the bare gold-water interface by non-equilibrium molecular dynamics. The value obtained was of 104.5 MW m^{-2} K^{-1}, which was shown to be in very good agreement with experimental and computational results. Using this value on the ratio of the heat flows, it was estimated that for nanoparticles sizes up to 5 nm in radius, the overall heat flow should be dominated by the heat transfer at the gold-water interface, while for bigger particles, the heat conduction in the water should limit the overall heat flow in the system of spherical gold nanoparticles embedded in water.

We then proceeded our work by considering the effect of several organic coatings between the gold and the water on the heat transfer at the interface. In chapter 7, non-equilibrium methods were employed to determine the heat transfer coefficient of several organic-coated gold-water interfaces. Independently of the organic coating tested, the value of the heat transfer coefficient decreased relative to that of the bare gold-water interface. For the gold coated with hydrophilic alkanethiols, the heat transfer coefficient was of 78 MW m^{-2} K^{-1}, while a smaller value of 41 MW m^{-2} K^{-1} was determined for the hydrophobic case. Consequently, the heat transfer mechanism which limits the overall heat propagation in the system should change for nanoparticle's radii of 7 and 14 nm for hydrophilic and hydrophobic nanoparticles, respectively. Also, when increasing the length of the alkane chain, our results did not identify a considerable change on the value of the heat transfer coefficient, in agreement with other experimental and computational results. Our results led us to conclude that the organic coating introduced a barrier on the heat transferred at the interface, acting then as a shield of the hot nanoparticle to the surrounding medium. Moreover, the hydrophilicity of the organic coating had a bigger effect on the heat transferred at the interface than the thickness of the organic coating.

Motivated by the results obtained in chapter 6, that is, the dependence of the dominant heat transfer mechanism with the nanoparticle size, systems of hot gold nanoparticles embedded in water were explored by non-equilibrium molecular dynamics. In chapter 8, the effect of the size and temperature of the nanoparticle on the tempera-

ture profile and heat propagation were investigated. Regarding the nanoparticle size, as the nanoparticle radius increased, the dominance of the heat transfer through the interface decreased, as predicted in chapter 6. This was identified by a considerable reduction of the temperature drop at the interface, while the temperature difference within the water was not greatly affected. When the nanoparticle reached a radius of 5-7 nm, the temperature drop at the interface was similar to the one in the water. This led to the conclusion that, for radius of around 5-7 nm, the heat released by the interface approaches the heat conducted in the water. Furthermore, the value of the heat transfer coefficient increased as the nanoparticle size decreased. As the size of the nanoparticle reached radii of 1 nm, this effect was bigger. Although for smaller particles the shape/surface of the nanoparticle can affect the value of the heat transfer coefficient, preliminary results indicated that the size had also an important contribution. As for the effect of the nanoparticle temperature, our computational results showed that the temperature drop at the interface increased at the same rate as the temperature difference within the water. Thus, the dominant heat transfer mechanism was unaffected. As for the heat transfer coefficient, its value increased proportionally with the temperature of the nanoparticle.

In summary, we quantified the heat transfer at the interface between the water and gold (bare and organic-coated), using non-equilibrium molecular dynamics. Our results showed that the organic coating acts as a heat shield between the hot gold and the water. By changing the hydrophilicity of the head group, a change on the heat transfer between the gold and the water was confirmed, while the thickness of the organic layer does not change the heat transfer coefficient significantly. We then associated this nanoscale parameter, the heat transfer coefficient, with a macroscale model. This link allowed us to predict a transition of the dominant heat transfer mechanism at particle's radii of a few nanometers. We then tested this prediction with computer simulations of hot bare gold nanoparticles embedded in water. Our computational models verified that, as the nanoparticle size increased, the heat transfer through the interface became less dominant, with respect to the heat conduction in water. These models also allowed us to detect a dependence of the heat transfer coefficient at the gold-water interface with the size of the nanoparticle, but not such a remarkable dependence with the nanoparticle temperature. These studies have contributed to the understanding of the impact of nanoscale variables, such as the nanoparticle size and the gold-water

interfaces, in the heat transfer at larger scales. As the models resembled as closely as possible the biological environments and conditions where the gold nanostructures will be used, our findings are important factors to take into account for the use of gold nanostructures for biomedical applications.

9.1 Future work

The work developed so far presented very interesting results and allowed us to draw important conclusions regarding the use of gold nanoparticles as heat sources or scatterers in biological media. Nevertheless, several questions remain open and various conditions can still be explored with non-equilibrium molecular dynamics.

In section 8.2.1, it was suggested that the dependence of the heat transfer coefficient with the temperature of the nanoparticle could be understood by the increased amplitude and coupling between the nanoscale gold and the water phonon spectrum. This work could be extended with the analysis of the populations of vibrational modes on this system. For instance, the approach used in references [62] and [63] to determined the vibration density of states could be the basis for this analysis.

Regarding the use of organic-coated nanoparticles as heat sources, the effect of the density of the alkanethiols on the surface of the nanoparticles and of the alkane termination in the heat propagation of embedded gold nanoparticles is a relevant issue to be addressed by computational methods. For instance, the arrangement and dynamics of the alkanethiols may vary with their densities, which can directly influence the heat propagated to the water.

Also, another issue not explored with the computational model is the time scale needed to heat up a water box, due to the heat released by a hot nanoparticle, to temperatures high enough to induce apoptosis and not necrosis. With the spherical system used, it should be possible to mimic several laser patterns. For instance, a continuous wave laser behaviour could be obtained by controlling the temperature of a hot nanoparticle in a non-thermostated water box. On the other hand, a pulsed laser could be simulated by removing all thermostats from a system of a hot gold nanoparticle embedded in water and allow it to relax. The overall increase in temperature could be evaluated, as well as the time needed to obtain the heat dissipation through the interface and conduction in the medium.

Bibliography

[1] Mark Winter. Gold: the essentials. http://www.webelements.com/gold/, 2009.

[2] Haley D. Hill, Jill E. Millstone, Matthew J. Banholzer, and Chad A. Mirkin. The role radius of curvature plays in thiolated oligonucleotide loading on gold nanoparticles. *ACS Nano*, 3(2):418–424, February 2009.

[3] Susumu Inasawa, Masakazu Sugiyama, and Yukio Yamaguchi. Laser-induced shape transformation of gold nanoparticles below the melting point: The effect of surface melting. *The Journal of Physical Chemistry B*, 109(8):3104–3111, March 2005.

[4] V. Pustovalov, L. Astafyeva, and B. Jean. Computer modeling of the optical properties and heating of spherical gold and silica-gold nanoparticles for laser combined imaging and photothermal treatment. *Nanotechnology*, 20(22):225105, 2009.

[5] K. Michaelian, N. Rendn, and I. L. Garzn. Structure and energetics of Ni, Ag, and Au nanoclusters. *Physical Review B*, 60(3):2000, July 1999.

[6] K. R. Catchpole and A. Polman. Plasmonic solar cells. *Optics Express*, 16(26):21793–21800, December 2008.

[7] Jure Strle, Damjan Vengust, and Dragan Mihailovic. Inorganic molecular-scale MoSI nanowire-gold nanoparticle networks exhibit self-organized critical self-assembly. *Nano Letters*, 9(3):1091–1095, March 2009.

[8] Min Li, Yu-Cheng Lin, Chao-Chin Wu, and Hsiao-Sheng Liu. Enhancing the efficiency of a PCR using gold nanoparticles. *Nucl. Acids Res.*, 33(21):e184, November 2005.

[9] Asmaa Elbakry, Alaa Zaky, Renate Liebl, Reinhard Rachel, Achim Goepferich, and Miriam Breunig. Layer-by-Layer assembled gold nanoparticles for siRNA delivery. *Nano Letters*, 9(5):2059–2064, May 2009.

[10] Xiangyang Shi, Suhe Wang, Sasha Meshinchi, MaryE. Van Antwerp, Xiangdong Bi, Inhan Lee, and James R. Baker Jr. Dendrimer-entrapped gold nanoparticles as a platform for cancer-cell targeting and imaging. *Small*, 3(7):1245–1252, 2007.

[11] Hugh H. Richardson, Michael T. Carlson, Peter J. Tandler, Pedro Hernandez, and Alexander O. Govorov. Experimental and theoretical studies of light-to-heat conversion and collective heating effects in metal nanoparticle solutions. *Nano Letters*, 9(3):1139–1146, March 2009.

[12] Ling Tong and Ji-Xin Cheng. Gold nanorod-mediated photothermolysis induces apoptosis of macrophages via damage of mitochondria. *Nanomedicine*, 4(3):265–276, March 2009.

[13] Andrew A. Burns, Jelena Vider, Hooisweng Ow, Erik Herz, Oula Penate-Medina, Martin Baumgart, Steven M. Larson, Ulrich Wiesner, and Michelle Bradbury. Fluorescent silica nanoparticles with efficient urinary excretion for nanomedicine. *Nano Letters*, 9(1):442–448, January 2009.

[14] Masato Yonezawa, Takanobu Otsuka, Nobuo Matsui, Hideki Tsuji, Kohichi H. Kato, Akihiko Moriyama, and Taiji Kato. Hyperthermia induces apoptosis in malignant fibrous histiocytoma cells *invitro*. *International Journal of Cancer*, 66(3):347–351, 1996.

[15] S. Kakaç and Y. Yener. *Heat Conduction*. Taylor & Francis, 3rd edition, December 1992.

[16] M. Necati Özişik. *Heat Transfer, a Basic Approach*. McGraw-Hill Inc., 1985.

[17] Charles Kittel. *Introduction to Solid State Physics*. John Wiley & Sons, 8th edition, November 2004.

[18] R. Carminati, P. Chantrenne, S. Dilhaire, S. Gomez, N. Trannoy, G. Tessier, and Sebastian Volz. *Microscale and Nanoscale Heat Transfer*. Springer, January 2007.

[19] S. R. Domen. Comment on 'Convection currents in a water calorimeter'. *Physics in Medicine and Biology*, 31(10):1166–1168, April 1986.

[20] Satish K. Nune, Nripen Chanda, Ravi Shukla, Kavita Katti, Rajesh R. Kulkarni, Subramanian Thilakavathy, Swapna Mekapothula, Raghuraman Kannan, and Kattesh V. Katti. Green nanotechnology from tea: phytochemicals in tea as building blocks for production of biocompatible gold nanoparticles. *Journal of Materials Chemistry*, 19(19):2912–2920, 2009.

[21] D. Porath, Y. Goldstein, A. Grayevsky, and O. Millo. Scanning tunneling microscopy studies of annealing of gold films. *Surface Science*, 321(1-2):81–88, December 1994.

[22] T. F. Young, J. F. Chang, and H. Y. Ueng. Study on annealing effects of Au thin films on Si. *Thin Solid Films*, 322(1-2):319–322, June 1998.

[23] Rizia Bardhan, Nathaniel K. Grady, Joseph R. Cole, Amit Joshi, and Naomi J. Halas. Fluorescence enhancement by Au nanostructures: Nanoshells and nanorods. *ACS Nano*, 3(3):744–752, March 2009.

[24] Zhen Yang, Xiaoning Yang, and Zhijun Xu. Molecular dynamics simulation of the melting behavior of PtAu nanoparticles with coreshell structure. *The Journal of Physical Chemistry C*, 112(13):4937–4947, April 2008.

[25] Joel Henzie, Eun-Soo Kwak, and Teri W. Odom. Mesoscale metallic pyramids with nanoscale tips. *Nano Letters*, 5(7):1199–1202, July 2005.

[26] Mathias Brust, Merryl Walker, Donald Bethell, David J. Schiffrin, and Robin Whyman. Synthesis of thiol-derivatised gold nanoparticles in a two-phase liquidliquid system. *Journal of the Chemical Society, Chemical Communications*, (7):801–802, January 1994.

[27] Mohammad Eghtedari, Anton V. Liopo, John A. Copland, Alexander A. Oraevsky, and Massoud Motamedi. Engineering of hetero-functional gold nanorods for the in vivo molecular targeting of breast cancer cells. *Nano Letters*, 9(1):287–291, January 2009.

[28] Kristin B. Cederquist and Christine D. Keating. Curvature effects in DNA:Au nanoparticle conjugates. *ACS Nano*, 3(2):256–260, February 2009.

[29] M Kumaresan and Cr Srinivas. Lasers for vascular lesions: Standard guidelines of care. *Indian Journal of Dermatology, Venereology, and Leprology*, 77(3):349, 2011.

[30] Rajesh Sardar, Alison M. Funston, Paul Mulvaney, and Royce W. Murray. Gold nanoparticles: Past, present, and future. *Langmuir*, 25(24):13840–13851, 2009.

[31] A. M. Schwartzberg, C. D. Grant, T. van Buuren, and J. Z. Zhang. Reduction of HAuCl4 by Na2S revisited: the case for au nanoparticle aggregates and against Au2S/Au core/shell particles. *Journal of Physical Chemistry C*, 111(25):8892–8901, 2007.

[32] Jin Zhong Zhang. Biomedical applications of Shape-Controlled plasmonic nanostructures: A case study of hollow gold nanospheres for photothermal ablation therapy of cancer. *The Journal of Physical Chemistry Letters*, 1(4):686–695, February 2010.

[33] Marites P. Melancon, Wei Lu, Zhi Yang, Rui Zhang, Zhi Cheng, Andrew M. Elliot, Jason Stafford, Tammy Olson, Jin Z. Zhang, and Chun Li. In vitro and in vivo targeting of hollow gold nanoshells directed at epidermal growth factor receptor for photothermal ablation therapy. *Molecular Cancer Therapeutics*, 7(6):1730–1739, June 2008.

[34] Ayush Verma and Francesco Stellacci. Effect of surface properties on nanoparticle-cell interactions. *Small*, 6(1):12–21, 2010.

[35] M.R. Melancon, W. Lu, and C. Li. Gold-based magneto/optical nanostructures: challenges for in vivo applications in cancer diagnostics and therapy. *MRS Bulletin*, 34(6):415–421, 2009.

[36] B. Devika Chithrani, Arezou A. Ghazani, and Warren C. W. Chan. Determining the size and shape dependence of gold nanoparticle uptake into mammalian cells. *Nano Letters*, 6(4):662–668, April 2006.

[37] Guodong Zhang, Zhi Yang, Wei Lu, Rui Zhang, Qian Huang, Mei Tian, Li Li, Dong Liang, and Chun Li. Influence of anchoring ligands and particle size on the colloidal stability and in vivo biodistribution of polyethylene glycol-coated gold nanoparticles in tumor-xenografted mice. *Biomaterials*, 30(10):1928–1936, April 2009.

[38] Hak Soo Choi, Wenhao Liu, Preeti Misra, Eiichi Tanaka, John P Zimmer, Binil Itty Ipe, Moungi G Bawendi, and John V Frangioni. Renal clearance of quantum dots. *Nature Biotechnology*, 25(10):1165–1170, October 2007.

[39] Particle shape & particle size analyzers, rheometers & viscometers. http://www.malvern.com/malvern/kbase.nsf/allbyno/KB000782, July 2010.

[40] Huang-Chiao Huang, Sutapa Barua, David B. Kay, and Kaushal Rege. Simultaneous enhancement of photothermal stability and gene delivery efficacy of gold nanorods using polyelectrolytes. *ACS Nano*, 3(10):2941–2952, October 2009.

[41] Aki Ito, Hajime Saito, Kazutaka Mitobe, Yoshihiro Minamiya, Naoko Takahashi, Kiyotomi Maruyama, Satoru Motoyama, Yoshihisa Katayose, and Junichi Ogawa. Inhibition of heat shock protein 90 sensitizes melanoma cells to thermosensitive ferromagnetic particle-mediated hyperthermia with low curie temperature. *Cancer Science*, 100(3):558–564, March 2009.

[42] O. Ekici, R. K. Harrison, N. J. Durr, D. S. Eversole, M. Lee, and A. Ben-Yakar. Thermal analysis of gold nanorods heated with femtosecond laser pulses. *Journal of Physics D: Applied Physics*, 41(18):185501, September 2008.

[43] Jose H. Hodak, Ignacio Martini, and Gregory V. Hartland. Spectroscopy and dynamics of nanometer-sized noble metal particles. *The Journal of Physical Chemistry B*, 102(36):6958–6967, 1998.

[44] V. Kotaidis, C. Dahmen, G. von Plessen, F. Springer, and A. Plech. Excitation of nanoscale vapor bubbles at the surface of gold nanoparticles in water. *The Journal of Chemical Physics*, 124(18):184702, 2006.

[45] Yusheng Dou, Leonid V. Zhigilei, Nicholas Winograd, and Barbara J. Garrison. Explosive boiling of water films adjacent to heated surfaces: a microscopic description. *The Journal of Physical Chemistry A*, 105(12):2748–2755, 2001.

[46] D. Keith Roper, W. Ahn, and M. Hoepfner. Microscale heat transfer transduced by surface plasmon resonant gold nanoparticles. *The Journal of Physical Chemistry C*, 111(9):3636–3641, March 2007.

[47] E. Sassaroli, K. C. P. Li, and B. E. O'Neill. Numerical investigation of heating of a gold nanoparticle and the surrounding microenvironment by nanosecond laser pulses for nanomedicine applications. *Physics in Medicine and Biology*, 54(18):5541–5560, September 2009.

[48] Alexey N. Volkov, Carlos Sevilla, and Leonid V. Zhigilei. Numerical modeling of short pulse laser interaction with Au nanoparticle surrounded by water. *Applied Surface Science*, 253(15):6394–6399, May 2007.

[49] Min Hu and Gregory V. Hartland. Heat dissipation for au particles in aqueous solution: relaxation time versus size. *J. Phys. Chem. B*, 107(5):1284, 2003.

[50] Zhaohui Wang, David G. Cahill, Jeffrey A. Carter, Yee Kan Koh, Alexei Lagutchev, Nak-Hyun Seong, and Dana D. Dlott. Ultrafast dynamics of heat flow across molecules. *Chemical Physics*, 350(13):31–44, June 2008.

[51] Mark D. Losego, Martha E. Grady, Nancy R. Sottos, David G. Cahill, and Paul V. Braun. Effects of chemical bonding on heat transport across interfaces. *Nature Materials*, 11(6):502–506, 2012.

[52] Vincent Juvé, Mattia Scardamaglia, Paolo Maioli, Aurelien Crut, Samy Merabia, Laurent Joly, Natalia Del Fatti, and Fabrice Vallée. Cooling dynamics and thermal interface resistance of glass-embedded metal nanoparticles. *Physical Review B*, 80(19):195406–6, November 2009.

[53] Orla M. Wilson, Xiaoyuan Hu, David G. Cahill, and Paul V. Braun. Colloidal metal particles as probes of nanoscale thermal transport in fluids. *Physical Review B*, 66(22):224301, December 2002.

[54] Zhenbin Ge, David G. Cahill, and Paul V. Braun. AuPd metal nanoparticles as probes of nanoscale thermal transport in aqueous solution. *The Journal of Physical Chemistry B*, 108(49):18870–18875, December 2004.

[55] Joshua Alper and Kimberly Hamad-Schifferli. Effect of ligands on thermal dissipation from gold nanorods. *Langmuir*, 26(6):3786–3789, March 2010.

[56] Zhenbin Ge, David G. Cahill, and Paul V. Braun. Thermal conductance of hydrophilic and hydrophobic interfaces. *Physical Review Letters*, 96(18):186101–4, May 2006.

[57] David G. Cahill, Wayne K. Ford, Kenneth E. Goodson, Gerald D. Mahan, Arun Majumdar, Humphrey J. Maris, Roberto Merlin, and Simon R. Phillpot. Nanoscale thermal transport. *Journal of Applied Physics*, 93(2):793–818, January 2003.

[58] Samy Merabia, Pawel Keblinski, Laurent Joly, Laurent J. Lewis, and Jean-Louis Barrat. Critical heat flux around strongly heated nanoparticles. *Physical Review E*, 79(2):021404, February 2009.

[59] Jean-Louis Barrat and Franois Chiaruttini. Kapitza resistance at the liquid-solid interface. *Molecular Physics: An International Journal at the Interface Between Chemistry and Physics*, 101(11):1605, 2003.

[60] Harshit A. Patel, Shekhar Garde, and Pawel Keblinski. Thermal resistance of nanoscopic liquidliquid interfaces: Dependence on chemistry and molecular architecture. *Nano Letters*, 5(11):2225–2231, November 2005.

[61] Natalia Shenogina, Rahul Godawat, Pawel Keblinski, and Shekhar Garde. How wetting and adhesion affect thermal conductance of a range of hydrophobic to hydrophilic aqueous interfaces. *Physical Review Letters*, 102(15):156101–4, April 2009.

[62] Tengfei Luo and John R. Lloyd. Equilibrium molecular dynamics study of lattice thermal Conductivity/Conductance of Au-SAM-Au junctions. *Journal of Heat Transfer*, 132(3):032401, 2010.

[63] Tengfei Luo and John R. Lloyd. Non-equilibrium molecular dynamics study of thermal energy transport in AuSAMAu junctions. *International Journal of Heat and Mass Transfer*, 53(13):1–11, January 2010.

[64] Ming Hu, Dimos Poulikakos, Costas P. Grigoropoulos, and Heng Pan. Recrystallization of picosecond laser-melted ZnO nanoparticles in a liquid: A molecular dynamics study. *The Journal of Chemical Physics*, 132(16):164504, 2010.

[65] Samy Merabia, Sergei Shenogin, Laurent Joly, Pawel Keblinski, and Jean-Louis Barrat. Heat transfer from nanoparticles: A corresponding state analysis. *Proceedings of the National Academy of Sciences*, 106(36):15113 –15118, 2009.

[66] Anders Lervik, Fernando Bresme, and Signe Kjelstrup. Heat transfer in soft nanoscale interfaces: the influence of interface curvature. *Soft Matter*, 5(12):2407, 2009.

[67] Daan Frenkel and Berend Smit. *Understanding Molecular Simulation: From Algorithms to Applications*. Academic Press, 2nd edition, October 2001.

[68] William Smith. DL_POLY reference webpage. http://www.ccp5.ac.uk/DL_POLY, 2009.

[69] A. P. Sutton and J. Chen. Long-range Finnis Sinclair potentials. *Philosophical magazine letters*, 61(3):139–146, 1990.

[70] M.W. Finnis and J.E. Sinclair. Simple empirical n-body potential for transition metals. *Philosophical Magazine A: Physics of Condensed Matter, Structure, Defects and Mechanical Properties*, 50(1):45–55, 1984.

[71] Jan-Ole Joswig and Michael Springborg. Genetic-algorithms search for global minima of aluminum clusters using a Sutton-Chen potential. *Physical Review B*, 68(8):085408, 2003.

[72] Jonathan P. K. Doye and David J. Wales. Global minima for transition metal clusters described by Sutton-Chen potentials. *New Journal of Chemistry*, 22(7):733–744, 1998.

[73] E. Spohr. Ion adsorption on metal surfaces. the role of water-metal interactions. *Journal of Molecular Liquids*, 64(1-2):91–100, August 1995.

[74] Yusheng Dou, Leonid V. Zhigilei, Zbigniew Postawa, Nicholas Winograd, and Barbara J. Garrison. Thickness effects of water overlayer on its explosive evaporation at heated metal surfaces. *Nuclear Instruments and Methods in Physics Research Section B: Beam Interactions with Materials and Atoms*, 180(1-4):105–111, June 2001.

[75] Shin-Pon Ju. A molecular dynamics simulation of the adsorption of water molecules surrounding an Au nanoparticle. *The Journal of Chemical Physics*, 122(9):094718–6, March 2005.

[76] Valeri Petkov, Yong Peng, Geoff Williams, Baohua Huang, Donald Tomalia, and Yang Ren. Structure of gold nanoparticles suspended in water studied by X-ray diffraction and computer simulations. *Physical Review B*, 72(19):195402, November 2005.

[77] Pim Schravendijk, Nico van der Vegt, Luigi Delle Site, and Kurt Kremer. Dual-scale modeling of benzene adsorption onto ni(111) and au(111) surfaces in explicit water. *ChemPhysChem*, 6(9):18661871, 2005.

[78] Sheng Meng, E. G. Wang, and Shiwu Gao. Water adsorption on metal surfaces: A general picture from density functional theory studies. *Physical Review B*, 69(19):195404, May 2004.

[79] A. Michaelides. Density functional theory simulations of watermetal interfaces: waltzing waters, a novel 2D ice phase, and more. *Applied Physics A*, 85(4):415–425, September 2006.

[80] Ana Vila Verde, Jacqueline M. Acres, and Janna K. Maranas. Investigating the specificity of peptide adsorption on gold using molecular dynamics simulations. *Biomacromolecules*, 10(8):2118–2128, 2009.

[81] L. Nilsson and Mark. Structure and dynamics of the TIP3P, SPC, and SPC/E water models at 298 K. *The journal of physical chemistry. A*, 105(43):9954–9960, 2001.

[82] Frank Römer, Anders Lervik, and Fernando Bresme. Nonequilibrium molecular dynamics simulations of the thermal conductivity of water: A systematic investigation of the SPC/E and TIP4P/2005 models. *The Journal of Chemical Physics*, 137(7):074503–074503–8, August 2012.

[83] Luzheng Zhang, William A. Goddard III, and Shaoyi Jiang. Molecular simulation study of the c(4 x 2) superlattice structure of alkanethiol self-assembled monolayers on Au(111). *The Journal of Chemical Physics*, 117(15):7342–7349, October 2002.

[84] Pradip Kr. Ghorai and Sharon C. Glotzer. Molecular dynamics simulation study of self-assembled monolayers of alkanethiol surfactants on spherical gold nanoparticles. *The Journal of Physical Chemistry C*, 111(43):15857–15862, November 2007.

[85] MacKerell, D. Bashford, Bellott, Dunbrack, J. D. Evanseck, M. J. Field, S. Fischer, J. Gao, H. Guo, S. Ha, D. Joseph-McCarthy, L. Kuchnir, K. Kuczera, F. T. K. Lau, C. Mattos, S. Michnick, T. Ngo, D. T. Nguyen, B. Prodhom, W. E. Reiher, B. Roux, M. Schlenkrich, J. C. Smith, R. Stote, J. Straub, M. Watanabe, J. Wirkiewicz-Kuczera, D. Yin, and M. Karplus. All-atom empirical potential for molecular modeling and dynamics studies of proteins. *J. Phys. Chem. B*, 102(18):3586–3616, 1998.

[86] William L. Jorgensen, Jeffry D. Madura, and Carol J. Swenson. Optimized intermolecular potential functions for liquid hydrocarbons. *Journal of the American Chemical Society*, 106(22):6638–6646, October 1984.

[87] Steven Y. Liem and Kwong-Yu Chan. Simulation study of platinum adsorption on graphite using the Sutton-Chen potential. *Surface Science*, 328(1-2):119 – 128, 1995.

[88] Bjorn Hafskhold, Ichiro Fujihara, and Tamio Ikeshoji. A comparison of non-equilibrium molecular dynamics and NPT monte carlo methods for mixing properties and partial molar. *Molecular Physics*, 90(6).

[89] Philippe Jund and Rémi Jullien. Molecular-dynamics calculation of the thermal conductivity of vitreous silica. *Physical Review B*, 59(21):13707, June 1999.

[90] H. J. C. Berendsen, J. P. M. Postma, W. F. van Gunsteren, A. DiNola, and J. R. Haak. Molecular dynamics with coupling to an external bath. *The Journal of Chemical Physics*, 81(8):3684–3690, October 1984.

[91] James R. Morris. Complete mapping of the anisotropic free energy of the crystal-melt interface in Al. *Physical Review B*, 66(14):1441041–1441047, 2002.

[92] Neil W. Ashcroft and N. David Mermin. *Solid State Physics*. Thomson Learning, January 1976.

[93] Jmol: an open-source java viewer for chemical structures in 3D. http://www.jmol.org/.

[94] William Humphrey, Andrew Dalke, and Klaus Schulten. VMD: visual molecular dynamics. *Journal of Molecular Graphics*, 14(1):33–38, February 1996.

[95] Loren Beitra, Moyu Watari, Takashi Matsuura, Naonobu Shimamoto, Ross Harder, and Ian Robinson. Confocal microscope alignment of nanocrystals for coherent diffraction imaging. *AIP Conference Proceedings*, 1234(1):57–60, June 2010.

[96] Ph. Buffat and J-P. Borel. Size effect on the melting temperature of gold particles. *Physical Review A*, 13(6):2287, June 1976.

[97] Francesca Baletto and Riccardo Ferrando. Structural properties of nanoclusters: Energetic, thermodynamic, and kinetic effects. *Reviews of Modern Physics*, 77(1):371, May 2005.

[98] L. D. Marks. Experimental studies of small particle structures. *Reports on Progress in Physics*, 57(6):603–649, 1994.

[99] Craig L. Johnson, Etienne Snoeck, Manex Ezcurdia, Benito Rodriguez-Gonzalez, Isabel Pastoriza-Santos, Luis M. Liz-Marzan, and Martin J. Hytch. Effects of elastic anisotropy on strain distributions in decahedral gold nanoparticles. *Nature Materials*, 7(2):120–124, February 2008.

[100] Takeo Oku and Kenji Hiraga. Atomic structures and stability of hexagonal BN, diamond and Au multiply-twinned nanoparticles with five-fold symmetry. *Diamond and Related Materials*, 10(3-7):1398–1403, March 2001.

[101] S. Kakac and Y. Yener. *Heat Conduction*. Taylor & Francis, 3rd edition, December 1992.

[102] H. S. Carslaw and J. C. Jaeger. *Conduction of Heat in Solids*. OUP Oxford, 2nd edition, March 1986.

[103] W. A. Little. Kapitza resistance between helium and metals in the normal and superconducting states. *Physical Review*, 123(2):435–441, July 1961.

[104] J.H Van Sant. The spot-insulated plate. *Nuclear Engineering and Design*, 8(2):247–250, August 1968.

[105] A. Plech, V. Kotaidis, S. Grsillon, C. Dahmen, and G. von Plessen. Laser-induced heating and melting of gold nanoparticles studied by time-resolved X-ray scattering. *Physical Review B*, 70(19):195423, November 2004.

[106] John H. Perry. *The Chemical Engineers' Handbook*. McGraw-Hill Professional, 4th edition, 1963.

[107] Frank Schreiber. Structure and growth of self-assembling monolayers. *Progress in Surface Science*, 65(58):151–257, November 2000.

[108] Dana Glasner, Anatoly I. Frenkel, Britt Hedman, and Piero Pianetta. Geometrical characteristics of regular polyhedra: Application to EXAFS studies of nanoclusters. *AIP Conference Proceedings*, 882(1):746–748, February 2007.

[109] W. A. Little. Unimportance of surface roughness upon the Kapitza resistance. *Physical Review*, 123(6):1909–1911, 1961.

[110] M. Ramires, J. Fareleira, C. Nieto de Castro, M. Dix, and W. Wakeham. The thermal conductivity of toluene and water. *International Journal of Thermophysics*, 14(6):1119–1130, 1993.

[111] Martin Chaplin. Water models. http://www.lsbu.ac.uk/water/models.html, June 2009.

[112] H. J. C. Berendsen, J. R. Grigera, and T. P. Straatsma. The missing term in effective pair potentials. *The Journal of Physical Chemistry*, 91(24):6269–6271, November 1987.

Appendix A

Implementation of the NEMD methods in the MD code

The entries used on the MD program, DL_POLY_3.09, and the different subroutines created to implement the two thermostats and the heat source and sink methods are now briefly described.

Before choosing which non-equilibrium MD approach to use, it is necessary to declare what kind of system is being simulated. For that, the entry $sysType \;\; s$ needs to be added to the CONTROL file. If s is 1, then the simulated system is spherical, the gold nanoparticle must be placed in the centre of the water box and the two thermostat method must be used. The nanoparticle is coupled to a thermostat at temperature T_{hot}, while the water beyond a distance $\frac{L}{2} - d$ Å(where L is size of the water box and d is described later in section A.3 as the thickness of the slabs or coronae) is kept at a temperature T_{cold}. On the other hand, if s is smaller than 1, then the system simulated has a slab geometry, as the parallelepiped systems described in section 4.2.1 and 4.2.2. If s is 0, then the simulated system is composed by two gold slabs separated by a water box, where the identification of the gold slabs assumes that the centre of the simulation box is within the water layer. In this system, the gold slabs are set at different temperatures by either the two thermostats or the heat source and sink method.

A.1 Implementation of the two thermostats method

The two thermostats method uses *ensemble nvt twoThermostats* τ T_{cold} T_{hot} entry in the CONTROL file. This entry requires the thermostat fluctuation time τ[1] in picoseconds, and the desired targeted hot and cold temperatures T_{cold} and T_{hot} in Kelvin. The default values are $\tau = 0.1$, $T_{cold} = 300$ and $T_{hot} = 500$.

The two temperatures T_{cold} and T_{hot} are maintained at each of the regions in the system by two Berendsen thermostats. Each targeted temperature is obtained by rescaling, at each time step, the atomic velocities on the specific region by a quantity χ_{hot} or χ_{cold}, determined with equation 4.22. As a precaution, T_{hot} cannot be high enough to cause the disintegration of the nanoparticle, as the system will behave in a non-physical way and the program will not work correctly.

A.2 Implementation of the heat source and sink method

The entry *ensemble nvt SourceSink* τ p indicates that a non-equilibrium simulation, with heat source and heat sink conditions, is requested. The heat source and sink method implemented in DL_POLY_3.09 is designed to work with a two gold slab system, where a constant heat flux q between the energy source and the energy sink gold slab is controlled. In order to set the constant heat flux in the system, the user must specify the two input parameters: a relaxation time τ in picoseconds and a value p. The default values are $\tau = 0.1$ and $p = 0.2$. This parameter p has two meanings, depending on its value. If bigger than 100, p is the value of the heat flux in W m^{-2}. This value p, together with τ equals to Δt, can be directly used in equation 4.23 to determine the amount of energy ΔE added to/removed from the hot/cold gold slab. Once this value of ΔE is known, equation 4.29 can be used to calculate the rescaling factors $\alpha_{\pm}$. The $\alpha_{\pm}$ values are then used to rescale the velocities with equation 4.20. On the other hand, if p is smaller than 100, then it denotes a percentage. This provides a way to determine the energy added and removed from the system, given by a percentage of the initial kinetic energy of all gold atoms, i.e,

[1]It is advisable to use a small value for τ (e.g., 0.1 ps), in order to guarantee a stable temperature of the hot and cold slabs. Like this, it is expected that the system reaches a steady state regime in a reasonable amount of simulation time.

$$\Delta E_0 = \frac{p}{100}\frac{fN}{2}k_B T \quad . \tag{A.1}$$

Using ΔE_0, it is possible to determine the heat flux associated with this added energy, over a time τ (as Δt) and for the area of the system being tested, with equation 4.23. The calculation of q is done at the initial stage of the simulation, as part of the system's preparation, in subroutine *getNbSlabs*(...).

A.3 Monitoring the evolution of the system

In order to monitor the progress of the heat flow in the system and to assess when the steady state regime is reached, it is necessary to keep track of the evolution of its temperature profile. This required the implementation of monitoring tools in the MD code.

Initially, and depending on the gold geometry, the system is divided into slabs or coronae (described in section A.3.1) and the temperature of each slab/corona is calculated (described in section A.3.2).

A.3.1 Division of system into slabs or coronae

The division of system depends on the geometry of the gold structure. For the case of the spherical gold nanoparticles embedded in water, the system is divided in coronae, while for the systems in layers, a slab segmentation is chosen. The thickness of the slabs/coronae can be set from the CONTROL file by the entry *spaceBetSlabs* d, with d in ångströms. The default value is $d = 2.0$. This entry is used by subroutine *getNbSlabs*(...) as a preparation for the system analysis. For the system with gold layers (with or without an organic coating) separated by a layer of water, the number of slabs for the gold layers is determined independently from the rest of the system. For the cases of spherical nanoparticles in water, the coronae are always set from the nanoparticle's centre to the maximum size of the box.

This subroutine is called before the simulation starts, to determine the number of slabs or coronae that constitute each part of the system for the rest of the simulation. With this procedure and for the case of the slab system, if the system's size fluctuates during the run, the number of slabs in the system will remain constant, but the thickness of each slab will vary. Nevertheless, as the simulation starts from a relaxed configura-

tion, the thickness of each of the control slabs is not expected to change significantly from the initial input value.

A.3.2 Determination of the temperature per slab or corona

The temperature of each slab or corona in the system is only dependent of the number of atoms present in each section, i.e., the temperature can be determined by

$$T = \frac{\sum_i m_i v_i^2}{(3N + 3M + 6O)k_B} \quad , \tag{A.2}$$

where T is the slab/corona temperature, N is the number of gold atoms, M is the number of atomic constituents of the alkanethiols, O is the number of water molecules in the slab/corona, m_i and v_i are the mass and velocity, respectively, of the atom i present in the slab considered, and k_B is the Boltzmann constant. For the particular case of water, two methods can be used to evaluate the contribution of the water per section (slab or corona). In the first method, implemented in the DL_POLY code, the number of water molecules is determined by counting the number of oxygen atoms in the section, while the kinetic energy component is determined for all atoms present in the slab. For instance, if a certain water molecule is divided between two slabs/coronae, only the section that has the oxygen atom will take the molecule into account on O, but the kinetic energy will be divided between the slabs/coronae. Since the biggest contribution comes from the oxygen atom, it is expected that this approximation will not introduce a considerable error to the final result. A second method, not implemented in the DL_POLY code, also considers that the number of water molecules is determined by counting the number of oxygen atoms in the section, but in this case the entire water molecule contributes to the kinetic energy component. The down side of this method is that the section's limits are not respected.

Although not shown here, both these methods yield very similar results for bulk water. When the bulk water conditions are disturbed, as for the water close to a surface, the first method produces fictitious temperature values. For this reason, and when relevant, the first method is avoided in this work.

For a slab system, due to fluctuations in the system, the thickness of each control slab can change during the simulation. Thus, every time the evaluation of the temperatures of the slabs is requested, the limit of each of the slabs is determined.

Appendix B

Values for the material variables

- Thermal conductivity of gold: $k_{Au} = 320$ W m^{-1} K^{-1}, from [1]
- Density of gold: $\rho_{Au} = 19300$ kg m^{-3}, from [1]
- Specific heat capacity of gold: $c_{Au} = 25.42$ J mol^{-1} K^{-1}= 129.058 J kg^{-1} K^{-1}, from [1]
- Molar mass of gold: $M_{Au} = 196.96$ g mol^{-1}, from [1]
- Diffusivity of gold: $\alpha_{Wa} = 1.28 \times 10^{-4}$ m^2 s^{-1}, obtained from the previous values.
- Thermal conductivity of water: $k_{Wa} = 0.58$ W m^{-1} K^{-1}, from [16]
- Density of water: $\rho_{Wa} = 997.05$ kg m^{-3}, from [16]
- Specific heat capacity of water: $c_{Wa} = 75.338$ J mol^{-1} K^{-1}= 4181.9 J kg^{-1} K^{-1}, from [16]
- Diffusivity of water: $\alpha_{Wa} = 1.46 \times 10^{-7}$ m^2 s^{-1}, from [16]
- Critical temperature of water $T_{cr} = 647$ K, from [42]
- H[1] for water: ~ 100 W m^{-2} K^{-1}, from [15].
- Thermal conductivity of water vapour: $k_{WaVap} = 0.025$ W m^{-1} K^{-1}, from [16]
- Heat capacity of water vapour (at boiling point): $c_{WaVap} = 37.47$ J mol^{-1} K^{-1}= 2080.45 J kg^{-1} K^{-1}, from [16]

[1]The value of H should depend on the two materials and surface state, among other aspects.

- Density of water vapour (at boiling point): $\rho_{WaVap} = 0.5976$ kg m^{-3}, from [16]
- Diffusivity of water vapour: $\alpha_{WaVap} = 2.12 \times 10^{-5}$ m^2 s^{-1}, from [16]

For the DL_POLY potentials:

- For the metallic potentials, the values were mainly obtained from reference [69] and are:
  - $\epsilon = 0.012793$ eV
  - $a = 4.0782$ Å, from website [1]
  - $c = 34.408$
  - $n = 10$
  - $m = 8$
- For the water-gold potentials, the values were obtained from [45]:
  - $D_0 = 6.68 \times 10^{-2}$ eV
  - $\beta_O = 1.3$ Å^{-1}
  - $r_{e1} = 3.7$ Å
  - $\beta_H = 1.3$ Å^{-1}
  - $r_{e2} = -1.0$ Å
  - $r_{on} = 7$ Å
  - $r_{off} = 11$ Å
- For the water-water potentials, the parameters were mainly obtained from the website [111], which are based on the original values given in reference [112]:
  - $q_O = -0.8476$ e
  - $q_H = 0.4238$ e
  - $r_{cut} = 11$ Å
  - $d_{O-H} = 1$ Å

- $d_{H-H} = 1.63299$ Å

- For the gold-sulphur potential, the values were obtained from [83]:
  - $D_e = 0.13798$ eV
  - $r_{eq} = 2.903$ Å
  - $S = 8$

- For the intra-molecular potentials of the alkanethiols (from here onwards, the united atom carbon is named "X"):
  - Charge distribution:
    - C (of carboxylic group): $q_C = 0.75$ e
    - O (of carbonyl group): $q_O = -0.55$ e
    - O (of hydroxyl group): $q_O = -0.61$ e
    - H (of hydroxyl group): $q_H = 0.44$ e
    - X (bonded to carboxylic group): $q_X = -0.03$ e
    - X (remaining united atom carbons): $q_X = 0$
    - C (of methyl group): $q_C = -0.270$ e
    - H (of methyl group): $q_H = 0.09$ e
  - Bond potentials:
    - C=O: $k_{bond} = 65.046$ eV and $r_{eq} = 1.22$ Å, from [85]
    - C-O: $k_{bond} = 19.947$ eV and $r_{eq} = 1.4$ Å, from [85]
    - O-H: $k_{bond} = 47.267$ eV and $r_{eq} = 0.96$ Å, from [85]
    - C-X (for carboxylic acid): $k_{bond} = 17.346$ eV and $r_{eq} = 1.522$ Å, from [85]
    - X-X: $k_{bond} = 22.549$ eV and $r_{eq} = 1.54$ Å, from [84]
    - S-X: $k_{bond} = 19.254$ eV and $r_{eq} = 1.81$ Å, from [84]
    - C-H (of methyl group): $k_{bond} = 27.926$ eV and $r_{eq} = 1.111$ Å, from [85]
    - C-X (of methyl group): $k_{bond} = 19.297$ eV and $r_{eq} = 1.528$ Å, from [85]
  - Angle potentials:
    - O=C-O: $k_{angle} = 4.336$ eV and $\theta_{eq} = 123°$, from [85]
    - O=C-X: $k_{angle} = 6.071$ eV and $\theta_{eq} = 125°$, from [85]

* C-O-H: $k_{angle} = 4.770$ eV and $\theta_{eq} = 115°$, from [85]
* O-C-X: $k_{angle} = 4.770$ eV and $\theta_{eq} = 110.5°$, from [85]
* C-X-X (of carboxylic acid): $k_{angle} = 4.510$ eV and $\theta_{eq} = 108°$, from [85]
* X-X-X: $k_{angle} = 5.464$ eV and $\theta_{eq} = 109.47°$, from [84]
* X-X-S: $k_{angle} = 5.421$ eV and $\theta_{eq} = 114.4°$, from [84]
* H-C-X (of methyl group): $k_{angle} = 3.0008$ eV and $\theta_{eq} = 110.1°$, from [85]
* H-C-H (of methyl group): $k_{angle} = 3.0788$ eV and $\theta_{eq} = 108.4°$, from [85]
* C-X-X (of methyl group): $k_{angle} = 5.0302$ eV and $\theta_{eq} = 115°$, from [85]

– Urey-Bradley potentials:

* O (of carbonyl group) - O (hydroxyl group): $k_{bond} = 18.213$ eV and $r_{eq} = 2.262$ Å, from [85]
* O (of carbonyl group) - X: $k_{bond} = 18.213$ eV and $r_{eq} = 2.262$ Å, from [85]
* H (of methyl group) - X: $k_{bond} = 1.9774$ eV and $r_{eq} = 2.179$ Å, from [85]
* H (of methyl group) - H (of methyl group): $k_{bond} = 0.4683$ eV and $r_{eq} = 1.802$ Å, from [85]

– Torsion potentials:

* H-O-C-X: $A = 0.088896$ eV, $\delta = 180°$ and $m = 2$, from [85]
* O=C-O-H: $A = 0.088896$ eV, $\delta = 180°$ and $m = 2$, from [85]
* O-C-X-X: $A = 0.002168$ eV, $\delta = 180°$ and $m = 6$, from [85]
* O=C-X-X: $A = 0.002168$ eV, $\delta = 180°$ and $m = 6$, from [85]
* C-X-X-X (of carboxylic acid): $A = 0.008239$ eV, $\delta = 0°$ and $m = 3$ from [85]
* X-X-X-X: $A_0 = -0.023579$ eV, $A_1 = 0.122451$ eV, $A_2 = 0.023579$ eV, $A_3 = 0.272936$ eV and $\phi = 0°$, from [84]
* X-X-X-S: $A_0 = -0.023579$ eV, $A_1 = 0.122451$ eV, $A_2 = 0.023579$ eV, $A_3 = 0.272936$ eV and $\phi = 0°$, from [84]
* H-C-X-X (of methyl group): $A = 0.006938$ eV, $\delta = 0°$ and $m = 3$ from [85]

    * C-X-X-X (of methyl group): $A = 0.004336$ eV, $\delta = 180°$ and $m = 2$ from [85]
    * C-X-X-X (of methyl group): $A = 0.006505$ eV, $\delta = 0°$ and $m = 4$ from [85]
    * C-X-X-X (of methyl group): $A = 0.004336$ eV, $\delta = 180°$ and $m = 6$ from [85]

- For the van der Waals interactions, the Lennard-Jones parameters are:
  - Oxygen (SPCE water): $\epsilon = 6.77083 \times 10^{-3}$ eV and $\sigma = 3.166$ Å, from [112]
  - Sulphur: $\epsilon = 0.01723$ eV and $\sigma = 4.25$ Å, from [84]
  - Carbon (united atom): $\epsilon = 0.005117$ eV and $\sigma = 3.905$ Å, from [84]
  - Gold (using approach from [87]): $\epsilon = 0.09086$ eV and $\sigma = 2.65087$ Å
  - Carbon (of carboxylic acid): $\epsilon = 3.03549 \times 10^{-3}$ eV and $\sigma = 3.5636$ Å, from [85]
  - Oxygen (of carbonyl group): $\epsilon = 5.20369 \times 10^{-3}$ eV and $\sigma = 3.029$ Å, from [85]
  - Oxygen (of hydroxyl): $\epsilon = 6.58957 \times 10^{-3}$ eV and $\sigma = 3.1538$ Å, from [85]
  - Hydrogen (of hydroxyl): $\epsilon = 1.99475 \times 10^{-3}$ eV and $\sigma = 0.4$ Å, from [85]
  - Carbon (of methyl group): $\epsilon = 3.382398 \times 10^{-3}$ eV and $\sigma = 3.63487$ Å, from [85]
  - Hydrogen (of methyl group): $\epsilon = 1.040738 \times 10^{-3}$ eV and $\sigma = 2.3876$ Å, from [85]

Appendix C

Order parameter results for defects created in a perfect lattice

In this appendix, snapshots of the defects created in a perfect FCC cubic structure constituted by 2048 atoms of gold are presented. After each defect was created, the system was relaxed, by running it for 10 ps in NVT conditions, without periodic boundary conditions, at 10 K. Following this, the crystal order was evaluated using the local order parameter and the relative order parameter. As a final remark, for the analysis with the relative order parameter, the images shown do not contain the outer layer of atoms in order to facilitate the visualisation of the interior of the particle.

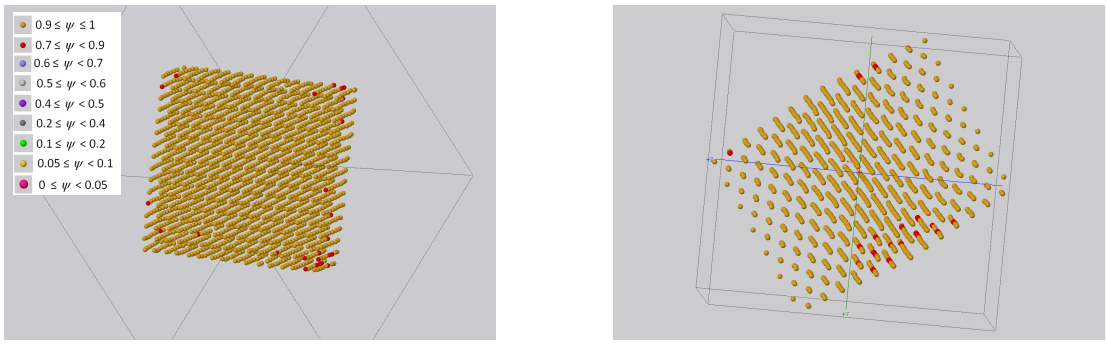

(a) (b)

Figure C.1: Order parameter colour scheme for a cubic system constituted by 2048 gold atoms, in a perfect crystal structure, where 5 vacancies were created. (a) and (b) result from the analysis of the system with the local and relative order parameter program, respectively.

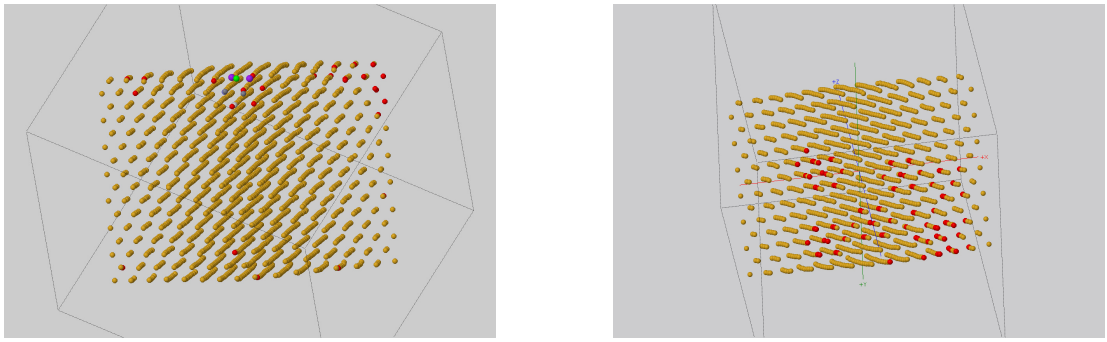

(a) (b)

Figure C.2: Order parameter colour scheme for a cubic system constituted by 2048 gold atoms, in a perfect crystal structure, where 10 vacancies were created. (a) and (b) represent the system analysed with the local and relative order parameter program, respectively.

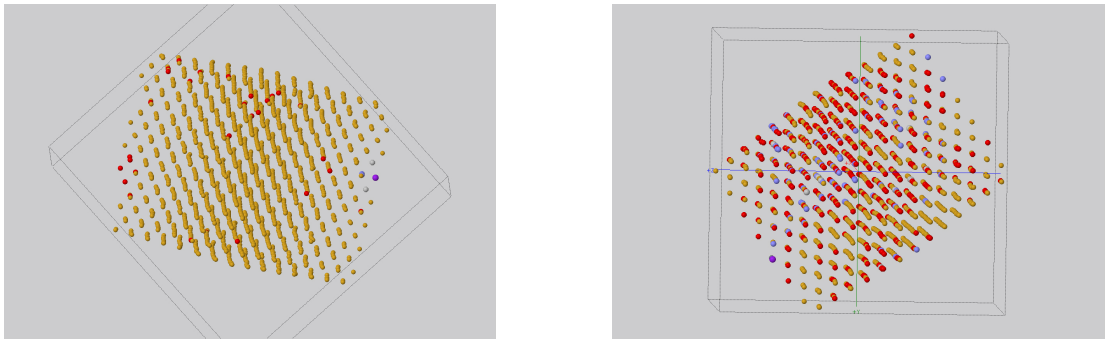

(a) (b)

Figure C.3: Order parameter colour scheme for a cubic system constituted by 2048 gold atoms, in a perfect crystal structure, where 100 vacancies were created. The system was analysed with (a) the local order parameter and (b) the relative order parameter program.

Appendix D

Results related to the annealing of the nanoparticles

In this appendix, snapshots and graphical results for the nanoparticles created are presented. The simulation conditions are also briefly described in the image captions.

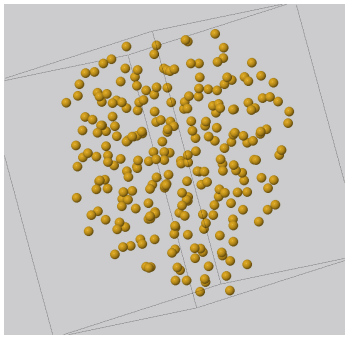

(a)

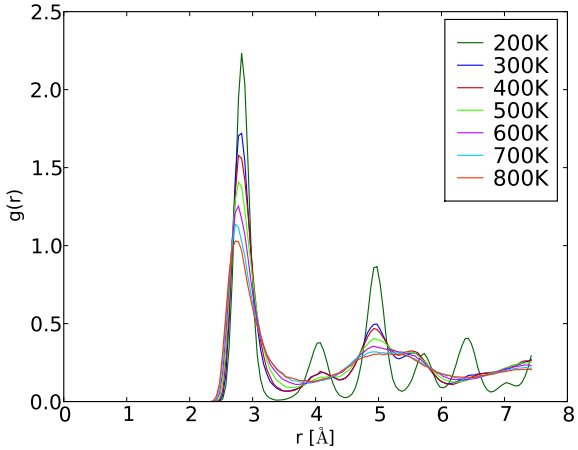

(b)

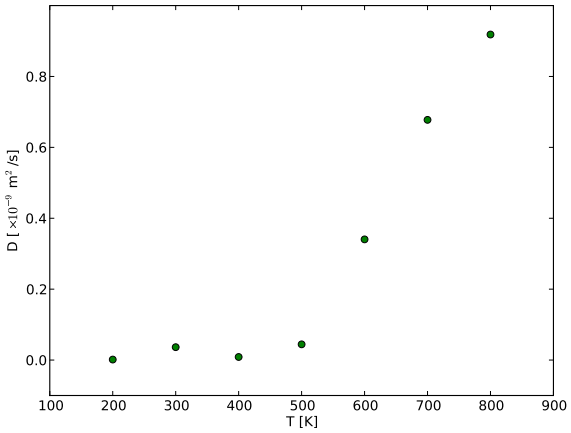

(c)

Figure D.1: Part 1/2 - Results for the heating process of the particle with approximately 2 nm diameter (256 atoms). The temperature increased from 200 K to 800 K, with a heating rate of 100K/100ps. All these simulations were run using NVT conditions and without no periodic boundary conditions. The results presented are (a) the atomic configuration at 800 K, after the heating process (at this point, the particle was completely melted), (b) the radial distribution functions and (c) diffusion coefficients at different temperatures.

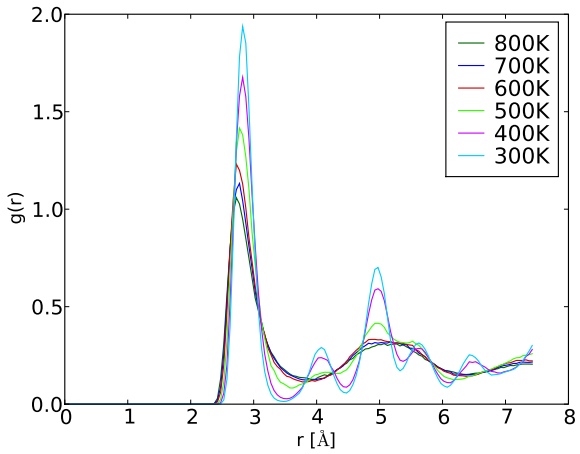

(a)

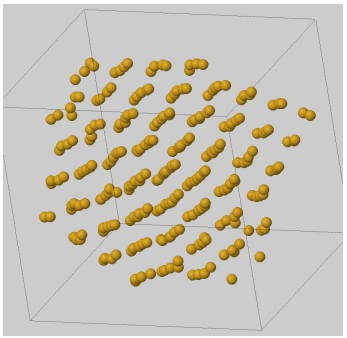

(b)

Figure D.2: Part 2/2 - Results for the cooling process of the particle with approximately 2 nm diameter (256 atoms). The temperature decreased from 800 K to 300 K, with a cooling rate of 10K/100ps. All these simulations were run under NVT conditions and without periodic boundary conditions. The results presented are (a) the radial distribution functions at different temperatures and (b) the atomic configuration at 300 K, after the annealing process.

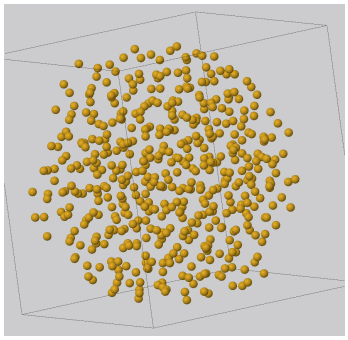

(a)

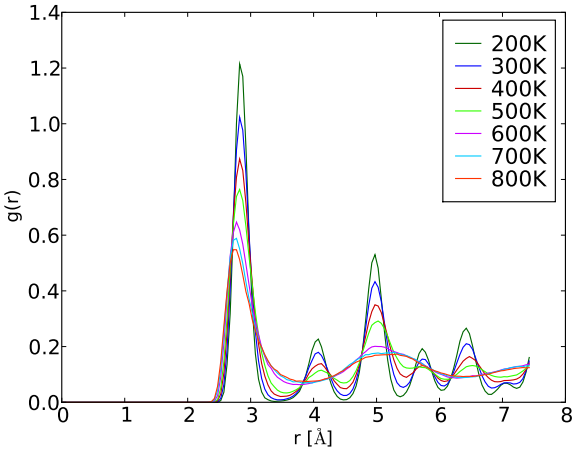

(b)

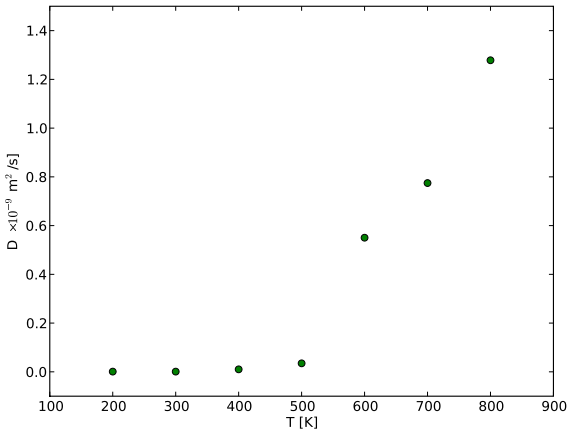

(c)

Figure D.3: Part 1/2 - Results for the heating process of the particle with approximately 2.5 nm diameter (500 atoms). The temperature increased from 200 K to 800 K, with a heating rate of 100K/100ps. All these simulations were run using NVT conditions and without periodic boundary conditions. The results presented are (a) the atomic configuration at 800 K, after the heating process (at this point, the particle was completely melted), (b) the radial distribution functions and (c) diffusion coefficients at different temperatures.

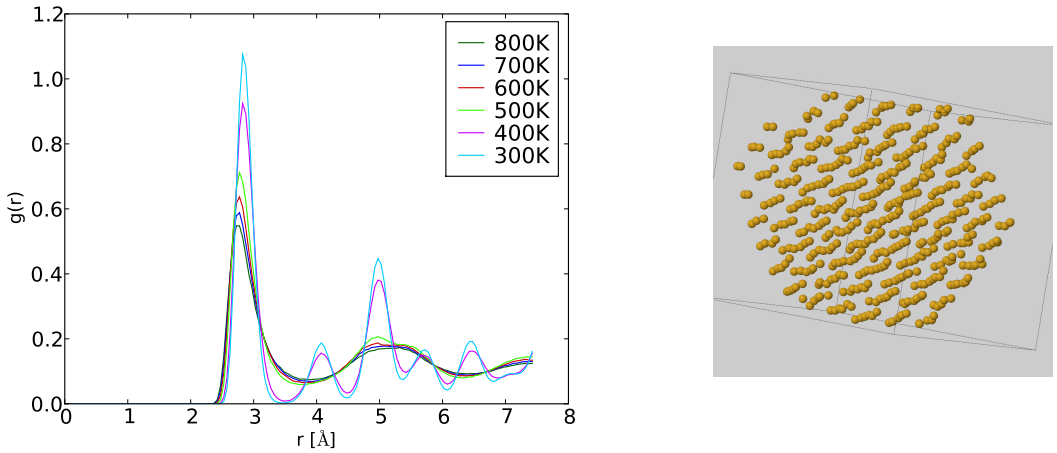

(a) (b)

Figure D.4: Part 2/2 - Results for the cooling process of the particle with approximately 2.5 nm diameter (500 atoms). The temperature decreased from 800 K to 300 K, with a cooling rate of 10K/100ps. All these simulations were run under NVT conditions and without periodic boundary conditions. (a) Radial distribution functions while the temperature of the nanoparticle is decreased. (b) Atomic configuration at 300 K, after the annealing process.

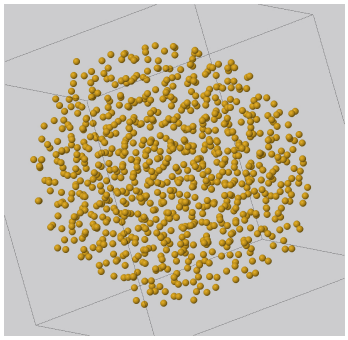

(a)

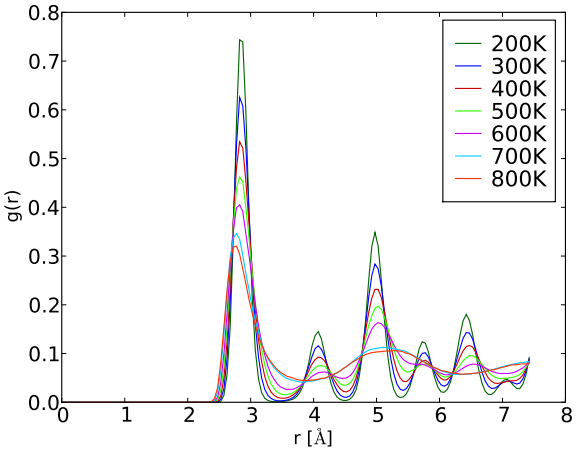

(b)

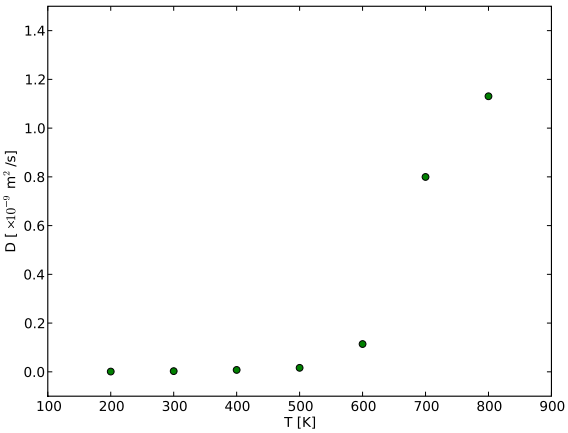

(c)

Figure D.5: Part 1/2 - Results for the heating process of the particle with approximately 3 nm diameter (864 atoms). The temperature increased from 200 K to 800 K, with a heating rate of 100K/100ps. All these simulations were run using NVT conditions and without periodic boundary conditions. The results presented are (a) the atomic configuration at 800 K, after the heating process (at this point, the particle is completely melted), (b) the radial distribution functions and (c) diffusion coefficients at different temperatures.

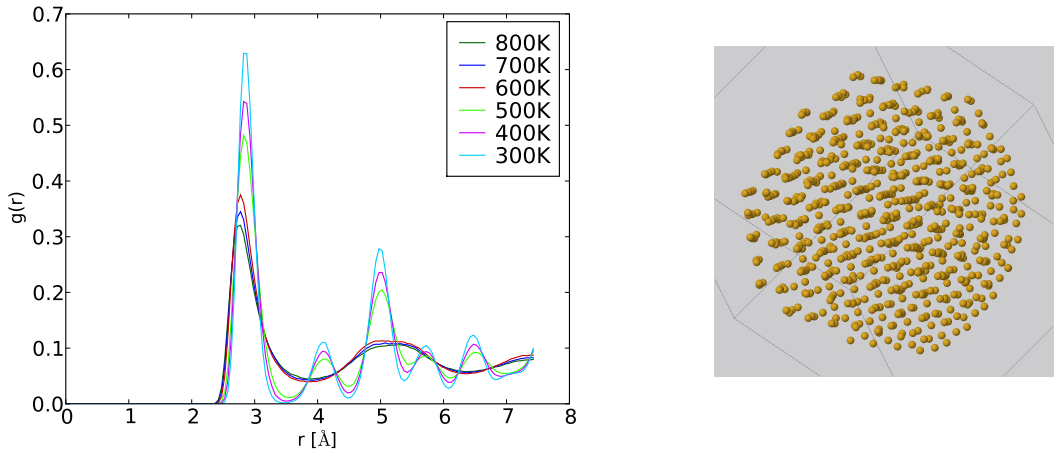

(a) (b)

Figure D.6: Part 2/2 - Results for the cooling process of the particle with approximately 3 nm diameter (864 atoms). The temperature decreased from 800 K to 300 K, with a cooling rate of 10K/100ps. All these simulations were run under NVT conditions and without periodic boundary conditions. The results presented are (a) the radial distribution functions for different temperatures and (b) the atomic configuration at 300 K, after the annealing process.

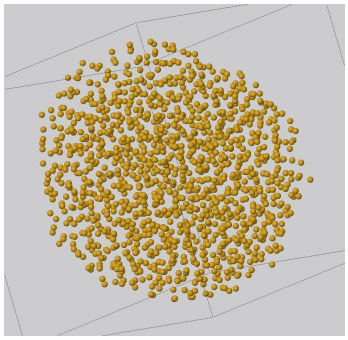

(a)

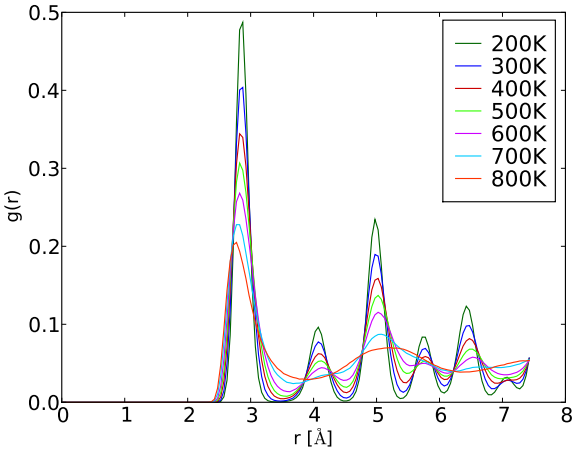

(b)

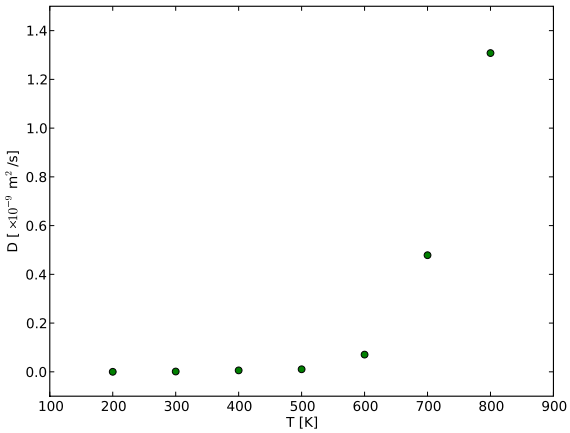

(c)

Figure D.7: Part 1/2 - Results for the heating process of the particle with approximately 3.5 nm diameter (1372 atoms). The temperature increased from 200 K to 800 K, with a heating rate of 100K/100ps. All these simulations were run using NVT conditions and without periodic boundary conditions. The results presented are (a) the atomic configuration at 800 K, after the heating process (at this point, the particle was completely melted), (b) the radial distribution functions and (c) diffusion coefficients for different temperatures.

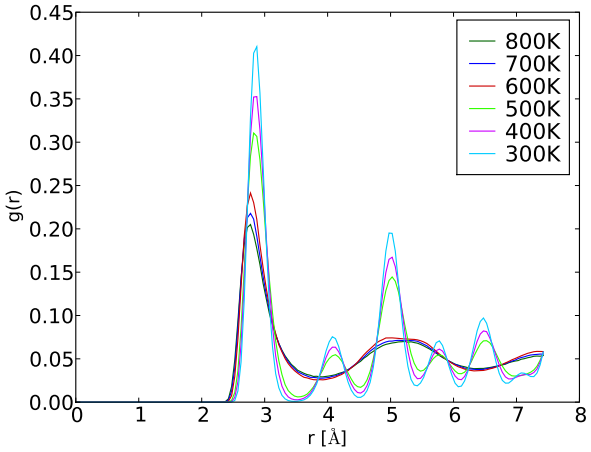

(a)

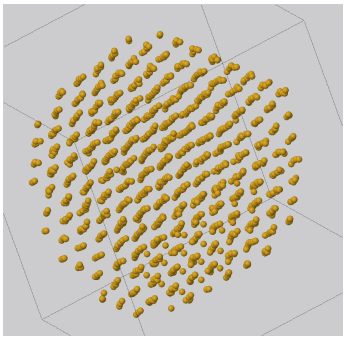

(b)

Figure D.8: Part 2/2 - Results for the cooling process of the particle with approximately 3.5 nm diameter (1372 atoms). The temperature decreased from 800 K to 300 K, with a cooling rate of 10K/100ps. All these simulations were run under NVT conditions and without periodic boundary conditions. The results presented are (a) the radial distribution functions for different temperatures and (b) the atomic configuration at 300 K, after the annealing process.

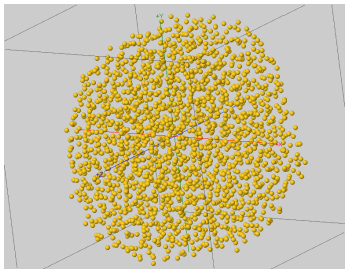

(a)

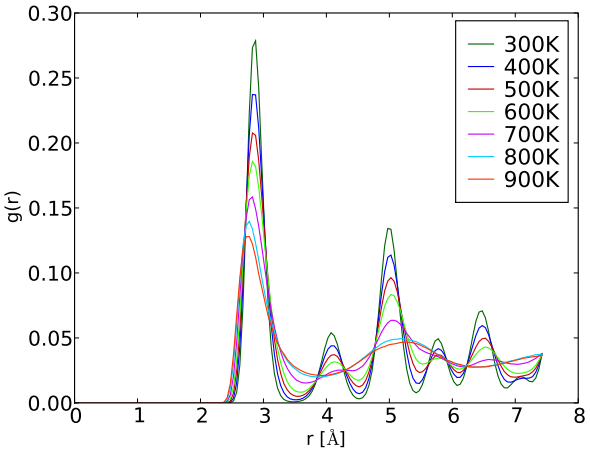

(b)

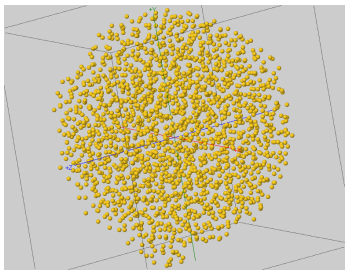

(c)

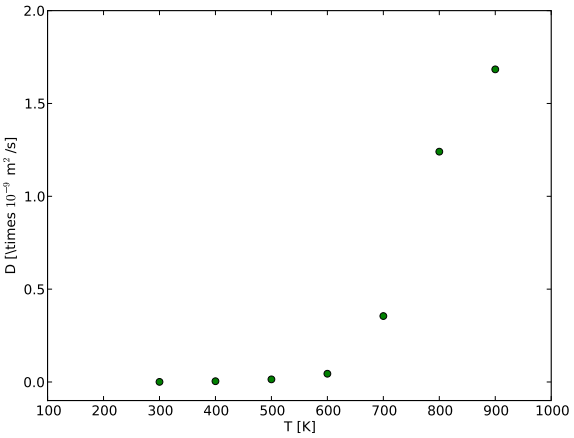

(d)

Figure D.9: Part 1/5 - Results for the heating process of the particle with approximately 4 nm diameter (2048 atoms). The heating process started at 300 K until 900 K was reached, with 100K/100ps heating rate, under NVT conditions and without periodic boundary conditions. The results presented are the atomic configurations (a) at 800 K and (c) at 900 K, after the heating process. At this point, the particle was completely melted. Also, (b) the radial distribution functions and (d) diffusion coefficients at different temperatures are shown.

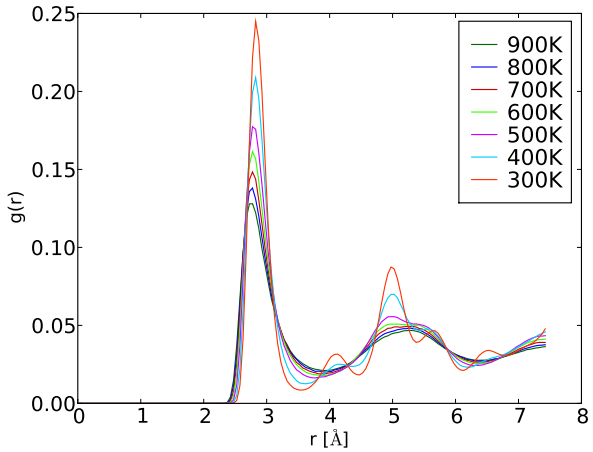

(a)

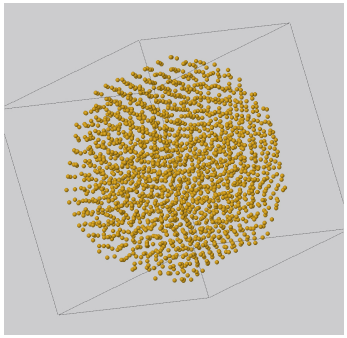

(b)

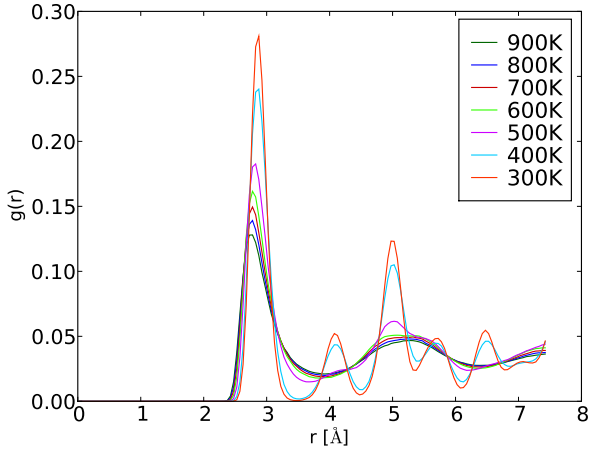

(c)

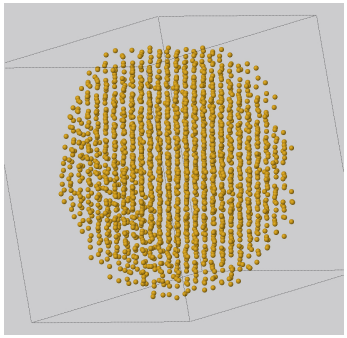

(d)

Figure D.10: Part 2/5 - Results for different cooling rates of the particle with approximately 4 nm diameter (2048 atoms). Each cooling process started at 900 K and was halted at 200 K. All these simulations were run with NVT conditions and without periodic boundary conditions. The results presented are of the radial distribution functions at different temperatures when the cooling rates were (a) 100K/100ps or 1 K/ps and (c) 50K/100ps or 0.5 K/ps. Also, the atomic configurations at 300 K when the cooling rates were (b) 100K/100ps or 1 K/ps and (d) 50K/100ps or 0.5 K/ps are shown.

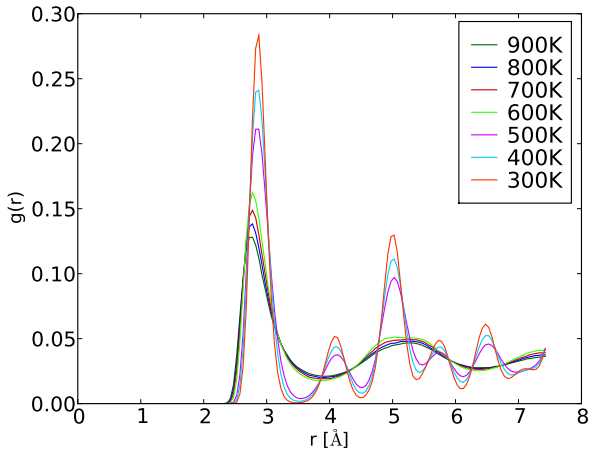

(a)

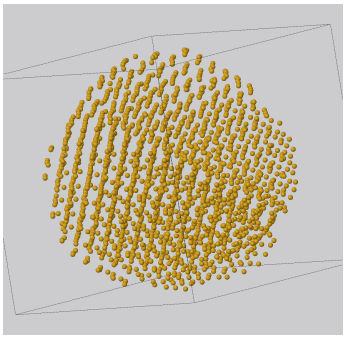

(b)

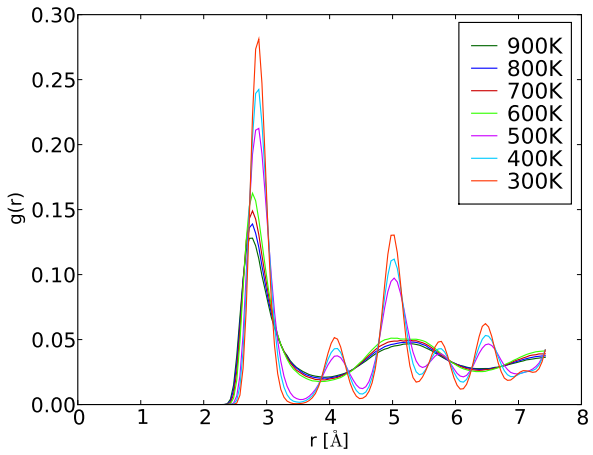

(c)

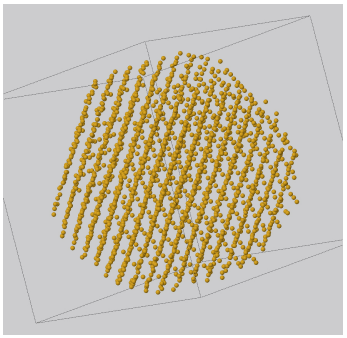

(d)

Figure D.11: Part 3/5 - Results for different cooling rates used for the particle with approximately 4 nm diameter (2048 atoms). The simulations conditions were described in previous figure. The results presented are of the radial distribution functions at different temperatures when the cooling rates were (a) 20K/100ps or 0.2 K/ps and (c) 10K/100ps or 0.1 K/ps. Also, the atomic configurations at 300 K when the cooling rates were (b) 20K/100ps or 0.2 K/ps and (d) 10K/100ps or 0.1 K/ps are shown.

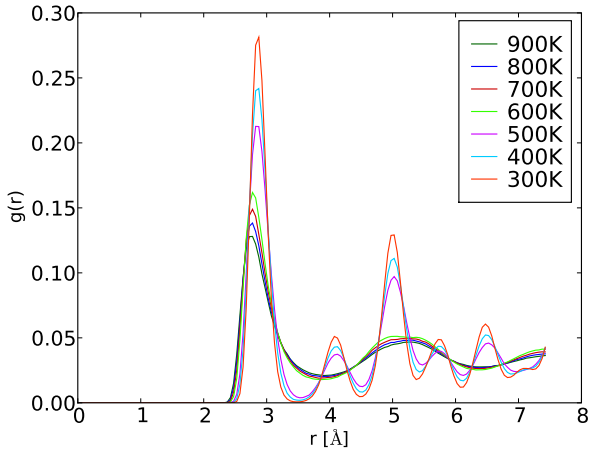

(a)

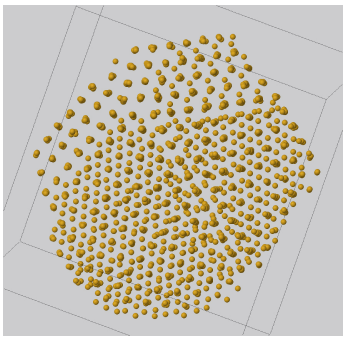

(b)

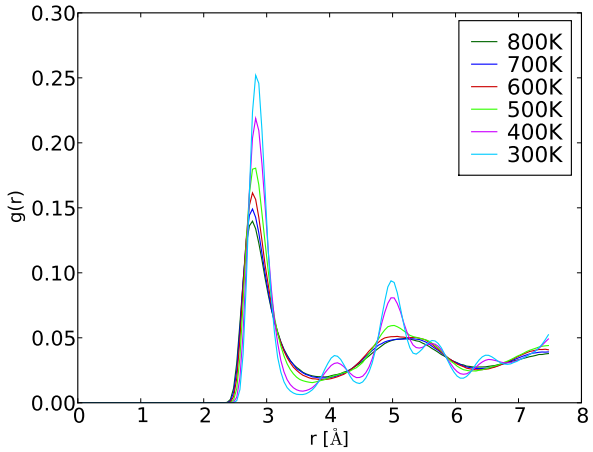

(c)

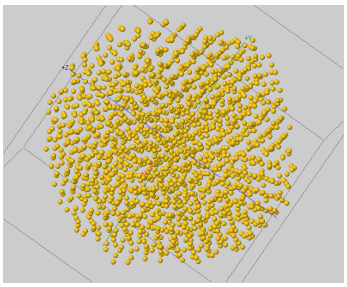

(d)

Figure D.12: Part 4/5 - Results for different cooling rates used for the particle with approximately 4 nm diameter (2048 atoms). For (a) and (b) the cooling process started at 900 K and was halted at 200 K, while for (c) and (d) the cooling process started at 800 K and stopped at 300 K. All the simulations were run with NVT conditions and without periodic boundary conditions. The results presented are of the radial distribution functions at different temperatures when the cooling rates were (a) 5K/100ps or 0.05 K/ps and (c) 100K/100ps or 1 K/ps. Also, the atomic configurations at 300 K when the cooling rates were (b) 5K/100ps or 0.05 K/ps and (d) 100K/100ps or 1 K/ps are shown.

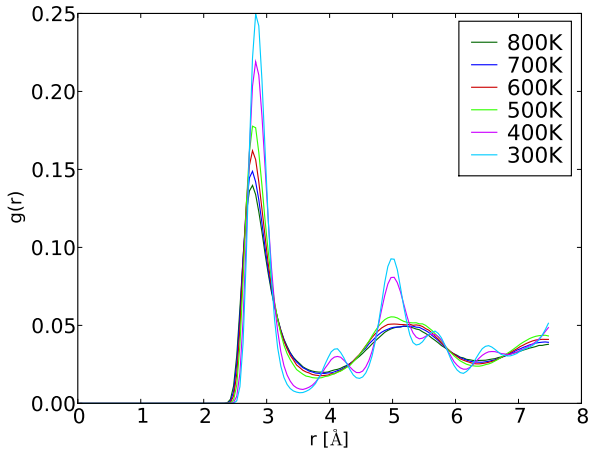

(a)

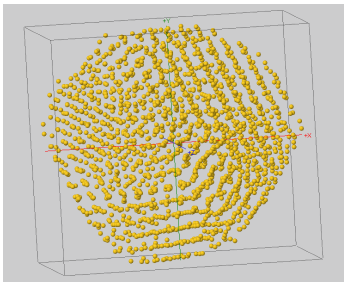

(b)

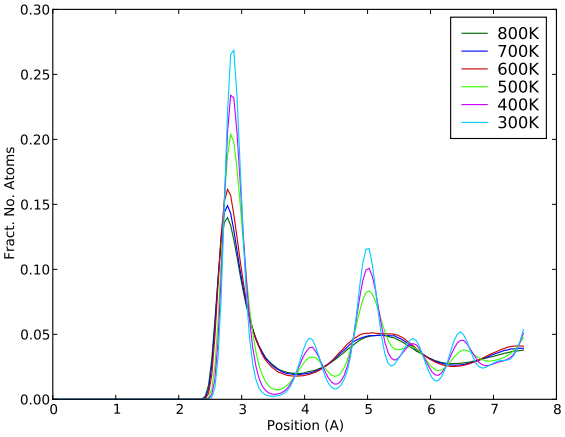

(c)

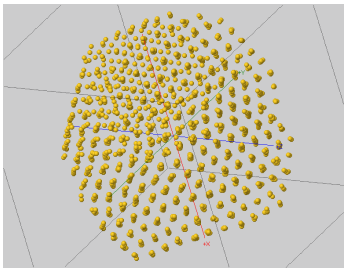

(d)

Figure D.13: Part 5/5 - esults for several cooling rates of the particle with approximately 4 nm diameter (2048 atoms). Cooling started at 800 K and was halted at 300 K. All simulations ran in NVT conditions and without periodic boundary conditions. The results presented are of the radial distribution functions at different temperatures when the cooling rates were (a) 50K/100ps or 0.5 K/ps and (c) 20K/100ps or 0.2 K/ps. Also, the atomic configurations at 300 K when the cooling rates were (b) 50K/100ps or 0.5 K/ps and (d) 20K/100ps or 0.2 K/ps are shown.

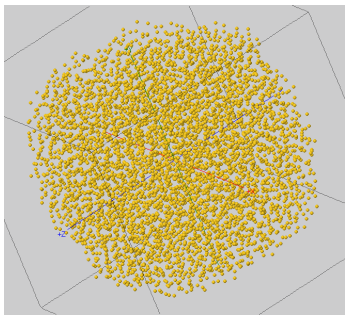

(a)

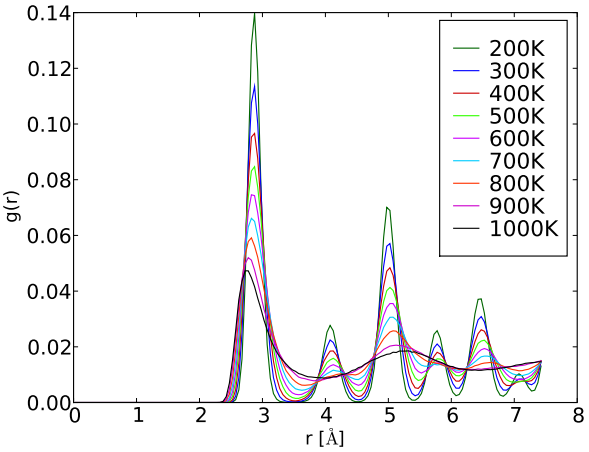

(b)

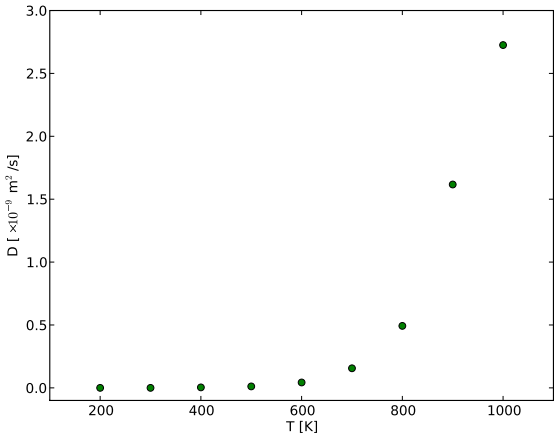

(c)

Figure D.14: Part 1/2 - Results for the heating process of the particle with approximately 5.5 nm diameter (5324 atoms). The heating process started at 200 K and finished at 1000 K, with a heating rate of 100K/10ps, under NVT conditions, without periodic boundary conditions. The results presented are (a) the atomic configuration at 1000 K, (b) the radial distribution functions and (c) diffusion coefficients at different temperatures.

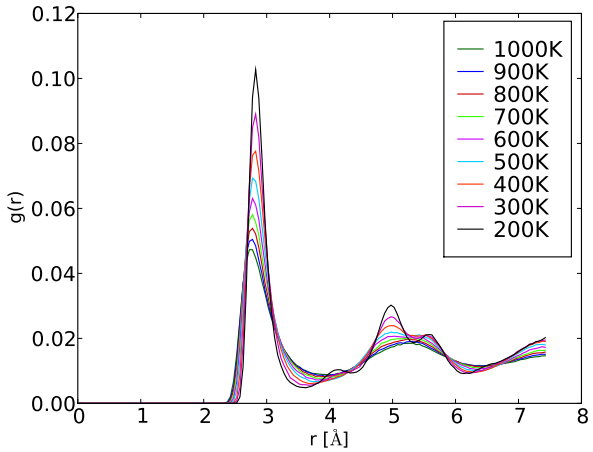

(a)

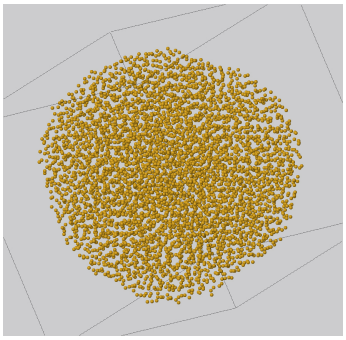

(b)

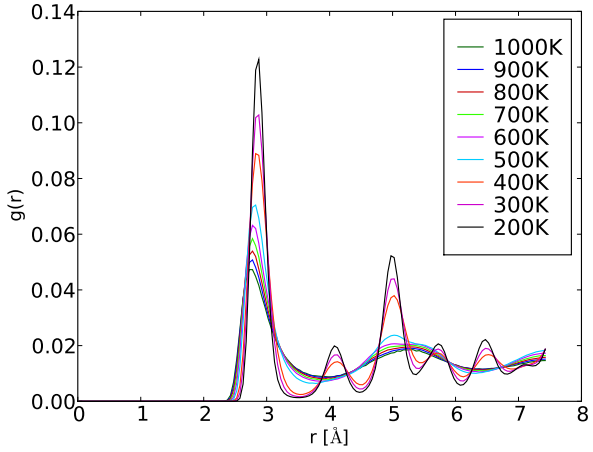

(c)

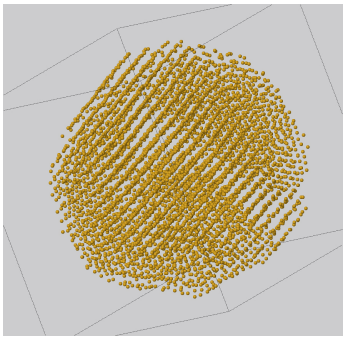

(d)

Figure D.15: Part 2/2 - Results for different cooling rates for the particle with approximately 5.5 nm diameter (5324 atoms). The cooling processes, which ran in NVT conditions and without periodic boundary conditions, started at 1000 K and were halted at 200 K. The results presented are of the radial distribution functions at different temperatures when the cooling rates were (a) 20K/10ps or 2 K/ps and (c) 20K/50ps or 0.4 K/ps. Also, the atomic configurations at 300 K when the cooling rates were (b) 20K/10ps or 2 K/ps and (d) 20K/50ps or 0.4 K/ps are shown.

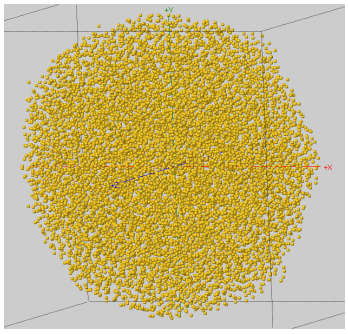

(a)

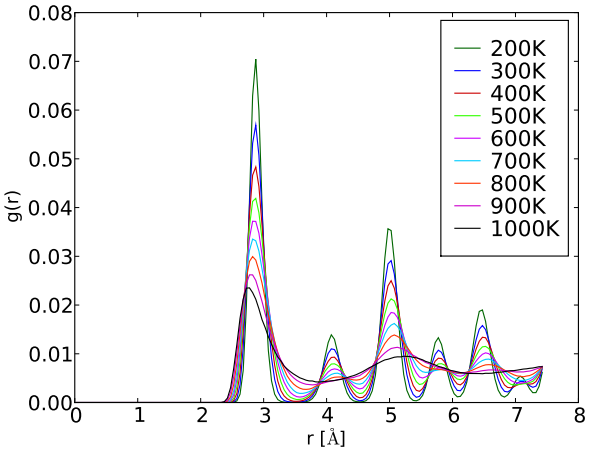

(b)

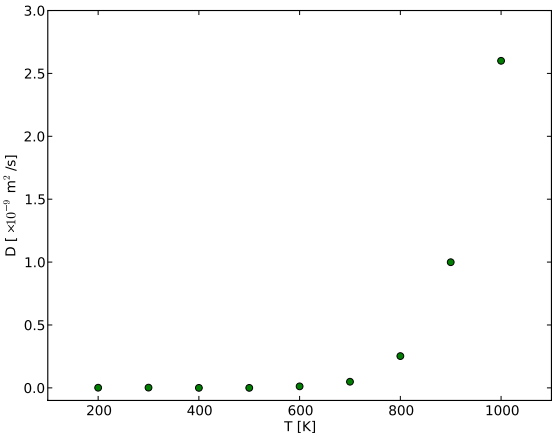

(c)

Figure D.16: Part 1/2 - Results for the heating process of the particle with approximately 7 nm diameter (10976 atoms). The temperature increased from 200 K to 1000 K, with a heating rate of 100K/10ps. All these simulations were run with NVT conditions and without periodic boundary conditions. The results presented are (a) the atomic configuration at 1000 K, (b) the radial distribution functions and (c) diffusion coefficients at different temperatures.

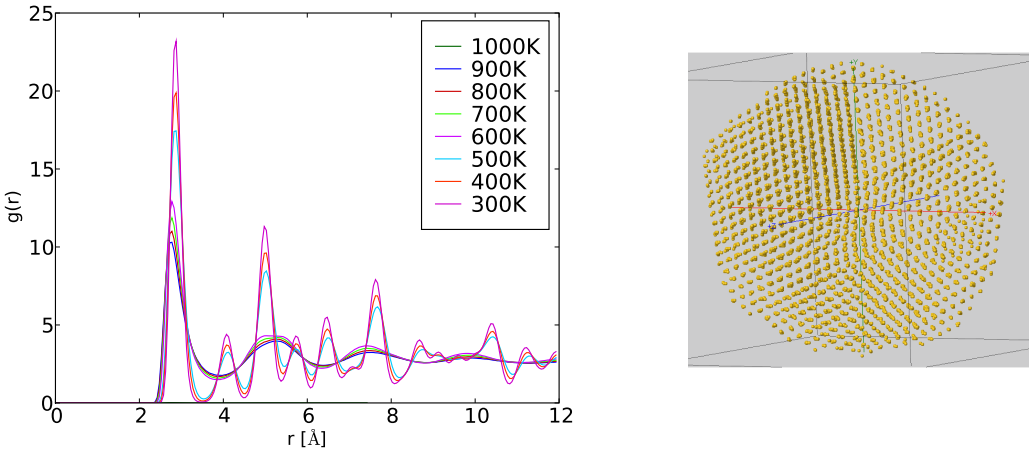

(a) (b)

Figure D.17: Part 2/2 - Results for the cooling process of the particle with approximately 7 nm diameter (10976 atoms). The temperature decreased from 1000 K to 300 K, with a cooling rate of 10K/100ps. All these simulations were run under NVT conditions and without periodic boundary conditions. The results presented are (a) the radial distribution functions at different temperatures and (b) the atomic configuration at 300 K.

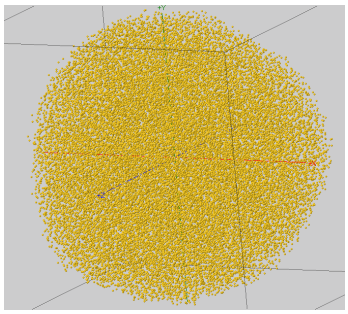

(a)

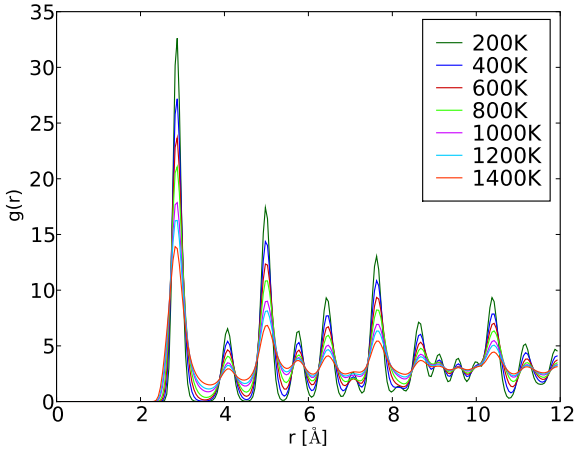

(b)

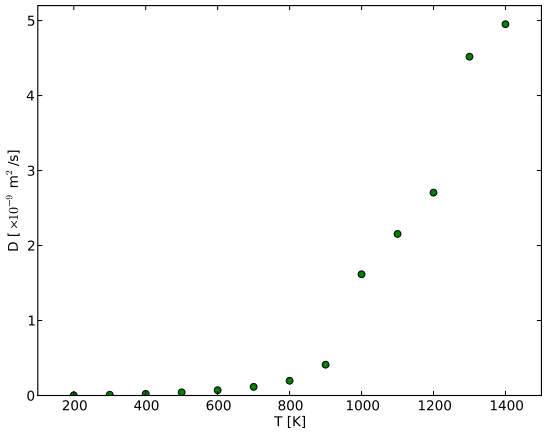

(c)

Figure D.18: Part 1/3 - Results for the heating process of the particle with approximately 10 nm diameter (32000 atoms). The temperature increased from 200 K to 1400 K, with a heating rate of 100K/20ps. All these simulations were run with NVT conditions and without periodic boundary conditions. The results presented are (a) the atomic configuration at 1400 K, the (b) radial distribution functions and (c) diffusion coefficients at different temperatures.

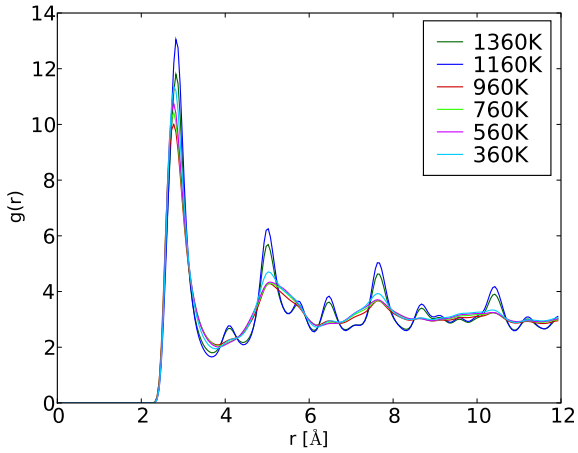

(a)

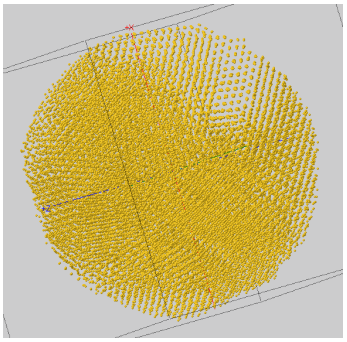

(b)

Figure D.19: Part 2/3 - Results for the cooling process of the particle with approximately 10 nm diameter (32000 atoms). The temperature decreased from 1400 K to 300 K, with a cooling rate of 20K/100ps. All these simulations were run under NVT conditions and without periodic boundary conditions. The results presented are the (a) radial distribution functions at different temperatures and the (b) atomic configuration at 300 K.

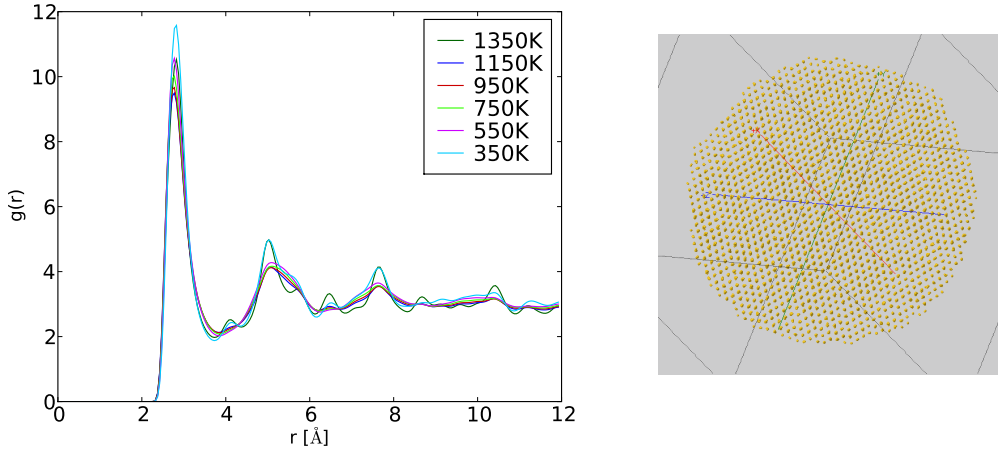

(a) (b)

Figure D.20: Part 3/3 - Results for the cooling process of the particle with approximately 10 nm diameter (32000 atoms). The temperature decreased from 1400 K to 300 K, with a cooling rate of 10K/100ps. All these simulations were run under NVT conditions and with periodic boundary conditions. The results presented are the (a) radial distribution functions at different temperatures and the (b) atomic configuration at 300 K.

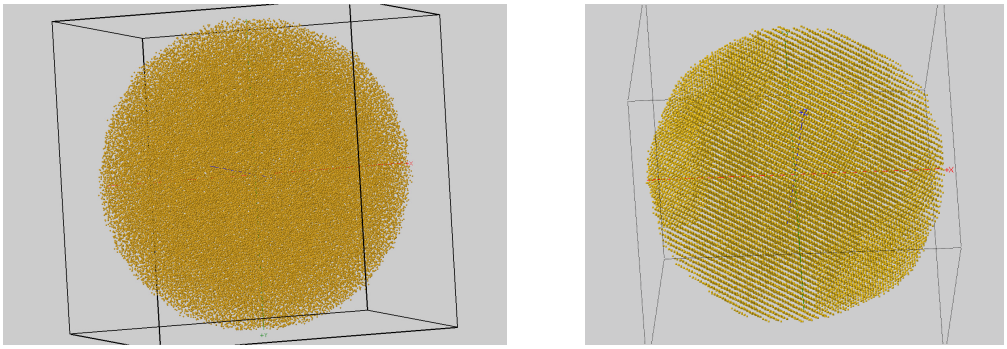

(a) (b)

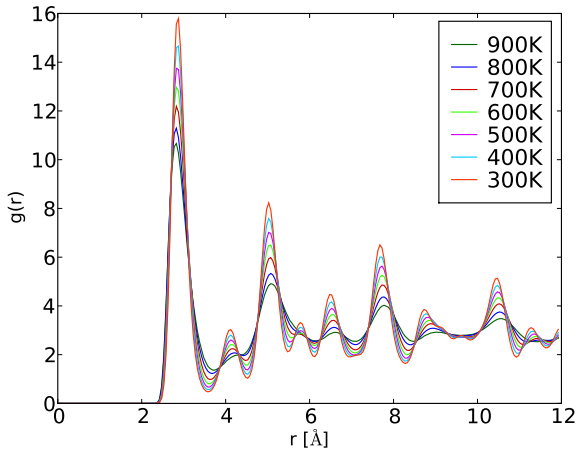

(c)

Figure D.21: Results for the production of the particle with approximately 14 nm diameter (84895 atoms). After cutting a sphere from a perfect FCC cube, the spherical particle was directly coupled with a heating bath at 900K. From this temperature, it was applied a cooling rate of 10K/10ps until 300K was reached. All these simulations were run under NVT conditions and without periodic boundary conditions. The results presented are the atomic configuration at (a) 900 K and (b) 300 K and (c) the radial distribution functions for different temperatures.

Appendix E

Results related to the abnormality of thirteen atomic neighbours

In this appendix, snapshots of clusters containing atoms surrounded by thirteen neighbours are shown. The effect of low temperatures on the particles that present some atoms with more than twelve neighbours is also displayed. When appropriate, the simulation conditions are briefly described.

For most of the nanoparticles, energy minimisation at 10 K is enough to limit the maximum number of neighbours to twelve. The only exception is the nanoparticle with diameter of approximately 7 nm, where even after a period of time at 10 K, the structure still presents atoms surrounded by more than twelve neighbours. The reason why this happens may be related with the annealing conditions used. For instance, the cooling process did not start at a temperature high enough and/or the cooling rate used was too fast to allow atomic reorganisation.

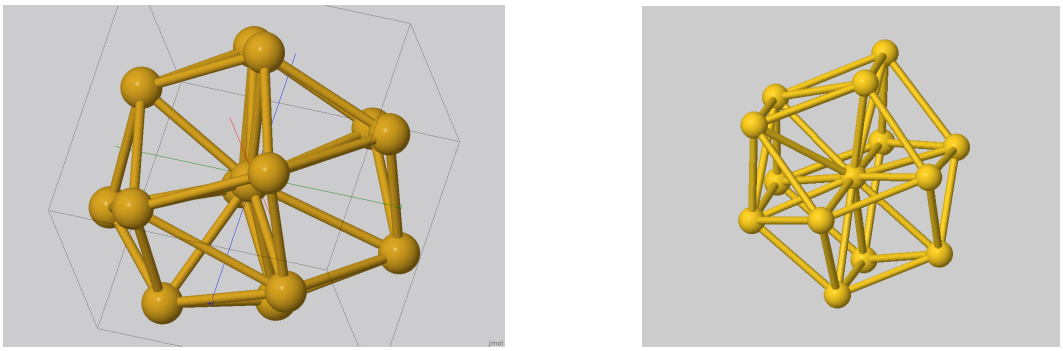

(a) (b)

Figure E.1: Clusters with thirteen neighbours present (a) in particle with approximately 2 nm in diameter and (b) in particle of approximately 7 nm in diameter, at 300 K. Note that the thirteenth neighbour disappears at 10 K. Images obtained with Jmol.

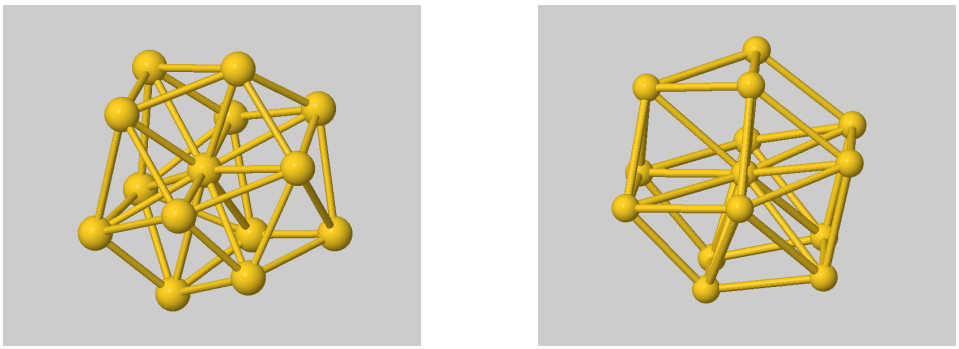

(a) (b)

Figure E.2: Cluster with thirteen neighbours present in particle of approximately 7 nm in diameter (a) at 300 K, that still exists at (b) 10 K. Images obtained with Jmol.

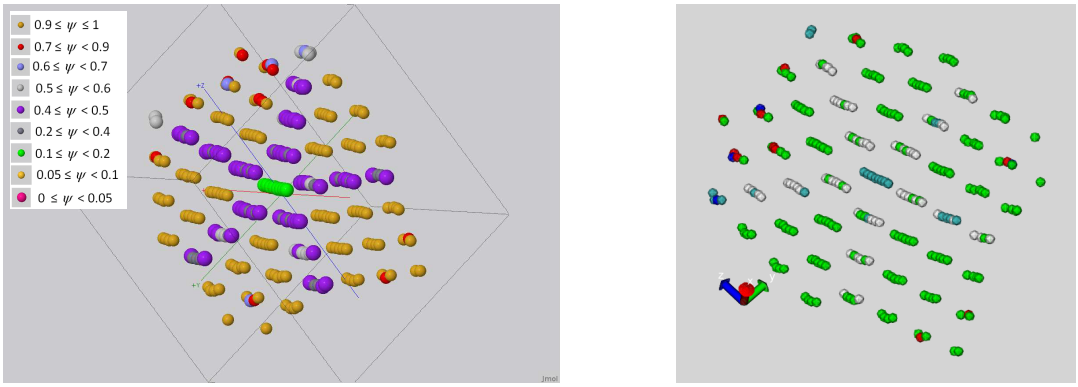

(a) (b)

Figure E.3: (a) Local order parameter colour scheme and (b) atoms with more than 12 neighbours (indicated by a larger volume), for the atomic configuration, at 10 K, after the particle with approximately 2 nm in diameter (256 atoms) underwent the annealing process with cooling rate of 10K/100ps or 0.1 K/ps. This result, obtained after the particle was annealed to 300 K, translates the minimised energy state achieved after the system was cooled down, for 5 ps, to 10 K in NVT conditions. A box big enough to model an isolated particle was used. In (b), it is verified that at a low temperature there are no atoms with more than twelve neighbours.

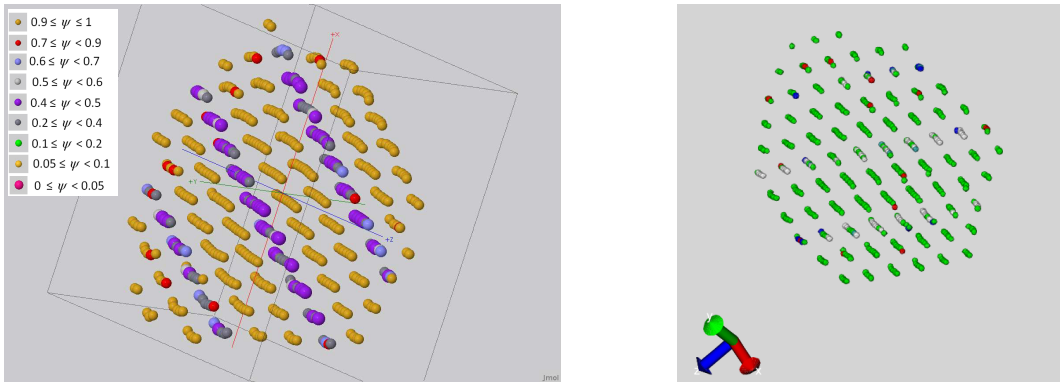

(a) (b)

Figure E.4: (a) Local order parameter colour scheme and (b) atoms with more than 12 neighbours (indicated by a larger volume), for the atomic configuration, at 10 K, after the particle with approximately 2.5 nm in diameter (500 atoms) underwent the annealing process with cooling rate of 10K/100ps or 0.1 K/ps. This result, obtained after the particle was annealed to 300 K, translates the minimised energy state achieved after the system was cooled down, for 5 ps, to 10 K in NVT conditions. A box big enough to model an isolated particle was used. In (b), it is verified that, at low temperatures, there are no atoms with more than twelve neighbours.

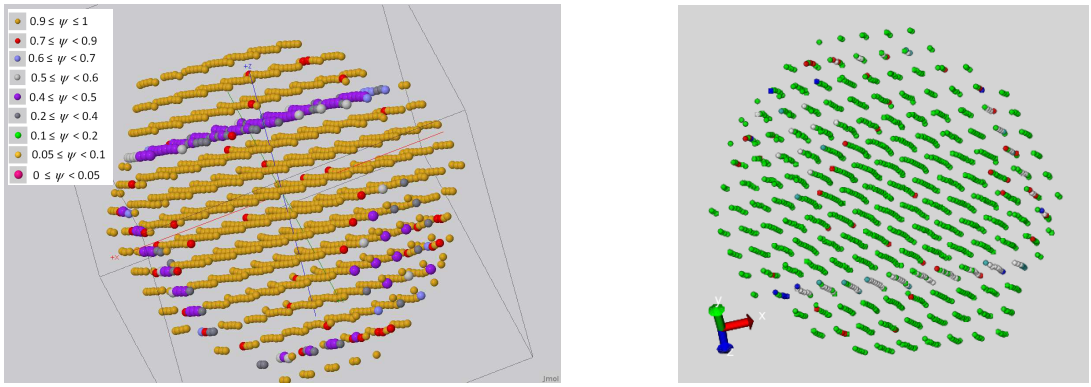

(a) (b)

Figure E.5: (a) Local order parameter colour scheme and (b) atoms with more than 12 neighbours (indicated by a larger volume), for the atomic configuration, at 10 K, after the particle with approximately 3.5 nm in diameter (1372 atoms) underwent the annealing process with a cooling rate of 10K/100ps or 0.1 K/ps. This result, obtained after the particle was annealed to 300 K, translates the minimised energy state achieved after the system was cooled down, for 5 ps, to 10 K in NVT conditions. A box big enough to model an isolated particle was used. In (b), at low temperatures, there are no atoms with more than twelve neighbours.

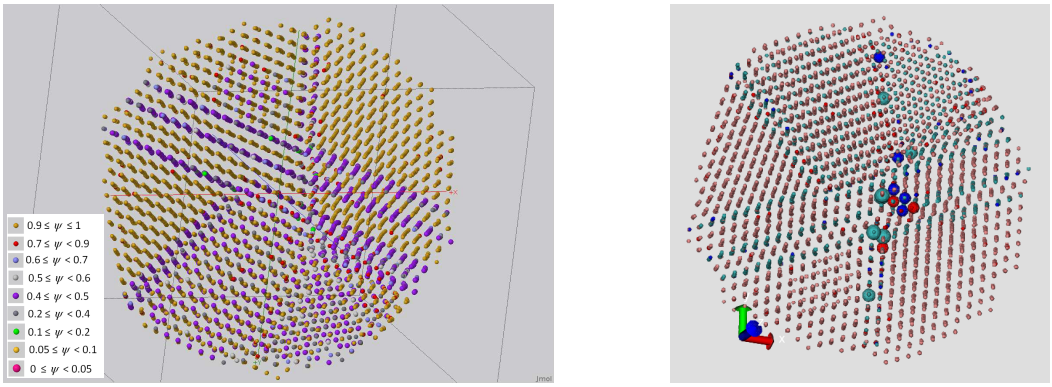

(a) (b)

Figure E.6: (a) Local order parameter colour scheme and (b) atoms with more than 12 neighbours (indicated by a larger volume), for the particle with approximately 7 nm in diameter (10976 atoms), after the energy state was minimised, for 10 ps, to 10 K in NVT conditions. Before the energy minimisation, the particle underwent the annealing process, with a cooling rate of 10K/100ps or 0.1 K/ps until 300 K. In (b), it is verified that, at low temperatures, the number of atoms with more than twelve neighbours considerably decreases from 29 to 18 atoms.

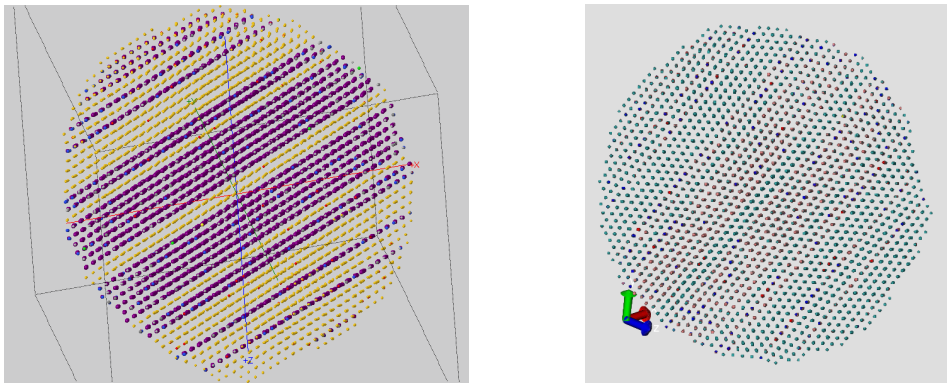

(a) (b)

Figure E.7: (a) Local order parameter colour scheme and (b) atoms with more than 12 neighbours (indicated by a larger volume), for the atomic configuration, at 10 K, after the particle with approximately 10 nm diameter (32000 atoms) underwent the annealing process, with the cooling rate of 10K/100ps or 0.1 K/ps. This result, obtained after the particle was annealed to 300 K, translates the minimised energy state achieved after the system was cooled down, for 10 ps, to 10 K in NVT conditions. A box big enough to model an isolated particle was used. In (b), it is verified that, at low temperatures, there are no atoms with more than twelve neighbours.

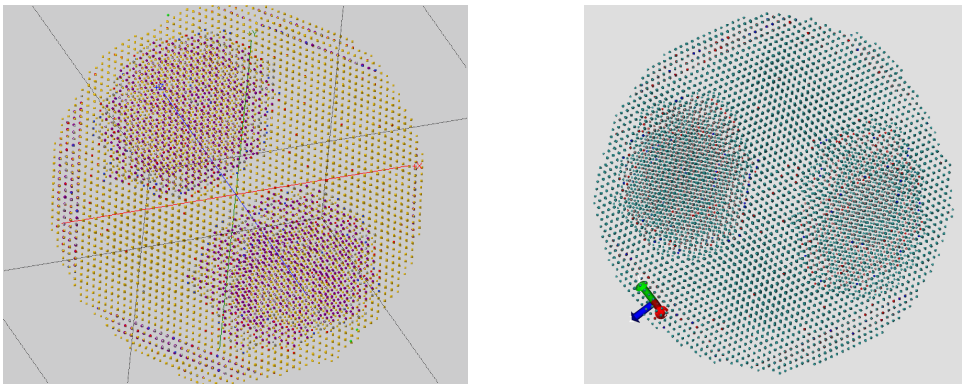

(a) (b)

Figure E.8: (a) Local order parameter colour scheme and (b) atoms with more than 12 neighbours (indicated by a larger volume), for the atomic configuration, at 10 K, after the particle with approximately 14 nm diameter (84895 atoms) underwent the annealing process, with the cooling rate of 10K/10ps or 1 K/ps . This result, obtained after the particle was cooled to 300 K, is the minimised energy state achieved after the system was cooled down, for 10 ps, to 10 K in NVT conditions. A box big enough to model an isolated particle was used. In (b), at low temperatures, there are no atoms with more than twelve neighbours.